October 2022

ANOMALOUS TRANSPORT, QUASIPERIODICITY, AND MEASUREMENT INDUCED PHASE TRANSITIONS

Utkarsh Agrawal
University of Massachusetts Amherst

ANOMALOUS TRANSPORT, QUASIPERIODICITY, AND MEASUREMENT INDUCED PHASE TRANSITIONS

A Dissertation Presented

by

UTKARSH AGRAWAL

Submitted to the Graduate School of the
University of Massachusetts Amherst in partial fulfillment
of the requirements for the degree of

DOCTOR OF PHILOSOPHY

September 2022

Department of Physics

ANOMALOUS TRANSPORT, QUASIPERIODICITY, AND MEASUREMENT INDUCED PHASE TRANSITIONS

A Dissertation Presented

by

UTKARSH AGRAWAL

Approved as to style and content by:

Romain Vasseur, Chair

Nikolay Prokofiev, Member

Tigran Sedrakyan, Member

Sarang Gopalakrishnan, Member

Anthony Dinsmore, Department Chair
Department of Physics

ACKNOWLEDGMENTS

I would like to firstly thank my advisor, Prof. Romain Vasseur for his constant guidance over the years. He was patient and tolerant of my ignorance of the field, which was alien to me when I started my PhD. His support and advice also helped me a lot in my professional development. I also grateful to my collaborators Prof. Sarang Gopalakrishnan, and Prof. Andrew Potter for providing different perspectives for thinking about a problem. None of the work in this thesis would have been possible without them.

I want to thank all my friends in the office, Chris, Vahini, Ke, Javier, Hans for various discussions, not just limited to physics, and past and present group members, Brayden, Aaron, and Fergus, for stimulating discussions during, and outside, the group meetings. I had also like to thank my friends Nishant, Manish, Aditya, Sam, Siao-Fong, Matt, and other batch mates for various group activities, especially when I was new around here. And most importantly, I want to express my gratitude to Virat for being a tolerant roommate for 5 years. Equally, my heart-felt thanks toward all persons who helped me, known or unknown to me, but who I do not know personally, or cannot remember right now.

I also want to thank all the members of my meditation group for our weekly "retreats," atleast before the pandemic. Finally, I cannot understate the importance of my parents and family in providing a sense of security and a home to fall back to.

ABSTRACT

ANOMALOUS TRANSPORT, QUASIPERIODICITY, AND MEASUREMENT INDUCED PHASE TRANSITIONS

SEPTEMBER 2022

UTKARSH AGRAWAL

B. Tech., INDIAN INSTITUTE OF TECHNOLOGY, BOMBAY

Ph.D., UNIVERSITY OF MASSACHUSETTS AMHERST

Directed by: Professor Romain Vasseur

With the advent of the noisy-intermediate scale quantum (NISQ) era quantum computers are increasingly becoming a reality of the near future. Though universal computation still seems daunting, a great part of the excitement is about using quantum simulators to solve fundamental problems in fields ranging from quantum gravity to quantum many-body systems. This so-called second quantum revolution rests on two pillars. First, the ability to have precise control over experimental degrees of freedom is crucial for the realization of NISQ devices. Significant progress in the control and manipulation of qubits, atoms, and ions, as well as their interactions, has not only allowed for emulation of diverse range of physical systems but has also led to realization of quantum systems in non-conventional settings such as systems out-of-equilibrium, driven by oscillating fields, and with quasiperiodic (QP) modulation. These systems often show novel properties which not only provide an

interesting testbed for NISQ devices but also an opportunity to exploit them for further development of quantum computing devices. Second, the study of dynamics of quantum information in quantum systems is essential for understanding and designing better quantum computers. In addition to their practical application as resource for quantum computation, quantum information has also become an essential element for our understanding of various physical problems, such as thermalization of isolated quantum many-body systems. This interplay between quantum information and computation, and quantum many-body systems is only expected to increase with time.

In this thesis, we explore these topics in two parts, corresponding respectively to the two pillars mentioned above. In the first part, we study effects of quasiperiodicity on many-body quantum systems in low dimensions. QP systems are aperiodic but deterministic, so their behavior differs from that of clean systems and disordered ones as well. Moreover, these systems can be conveniently realized in an experimental setting where it is easier to isolate them from external decoherence. We start with the easy-plane regime of the XXZ spin chain and show that the well-known fractal behavior of the spin Drude weight implies the divergence of the low-frequency conductivity for generic values of anisotropy. We tie this to the quasi-periodic structure in the Bethe ansatz solution resulting in different species of quasiparticles getting activated along the time evolution in a quasi-periodic pattern. We then study quantum critical systems under generic quasi-periodic modulations using real-space renormalization group (RSRG) procedure. In 1d, we show that the system flows to a new fixed point with the couplings following a discrete aperiodic sequence which allows us to analytically calculate the critical properties. We dub these new classes of quasi-periodic fixed points infinite-quasiperiodicity fixed points in line with the infinite-randomness fixed point observed in random quantum systems. We use this approach to analyze the quasiperiodic Heisenberg, Ising, and Potts spin chains. The RSRG is not ana-

lytically tractable in 2d, but numerically implementing it for the 2d quasi-periodic q-state quantum Potts model, we find that it is well controlled and becomes exact in the asymptotic limit. The critical behavior is shown to be largely independent of q and is controlled by an infinite-quasiperiodicity fixed point. We also provide a heuristic argument for the correlation length exponent and the scaling of the energy gap.

Moving on to the second part, we study monitored quantum circuits which have recently emerged as a powerful platform for exploring the dynamics of quantum information and errors in quantum systems. Unitary evolution generates entanglement between distant particles of the system. The dynamics of entanglement has been successfully studied by replacing the Hamiltonian evolution with random quantum circuits. Recently, the robustness of unitary evolution's ability to protect the entanglement against external projective measurements has received much attention. Entanglement is also a resource for quantum information, so its stability is directly related to the stability of a quantum computer against external noises. It has been observed that, in absence of any symmetry, there is a measurement induced phase transition (MIPT) in the behavior of bipartite entanglement that goes from volume law to area law as we tune the rate of measurements. Here we focus on monitored quantum circuits with U(1) symmetry which leads to the presence of a conserved charge density. These diffusive hydrodynamic modes scramble very differently than non-symmetric modes and we find that in addition to the entanglement transition, there is another transition *inside* the volume phase which we call a "charge sharpening" transition. The sharpening transition is a transition in the ability/inability of the measurements to detect the global charge of the system. We study this sharpening transition in a variety of settings, including an effective field theory that predicts the transition to be in a modified Kosterlitz-Thouless universality class. We provide various numerical evidence to back our predictions.

TABLE OF CONTENTS

LIST OF TABLES

Table **Page**

LIST OF FIGURES

Figure **Page**

Part I

Quantum criticality, anomalous transport and dynamics in low dimensional quasiperiodic systems

CHAPTER 1

INTRODUCTION

Recent advancements in the fields of twisted bi-layer graphene [1, 2, 3], cold atoms [4, 5, 6, 7, 8, 9, 10, 11, 12, 13, 14, 15, 16], and photonic lattices [17, 18, 19, 20] have made it easier than ever to engineer synthetic systems with quasi-periodic (QP) inhomogeneity, sparking a renewed interest in understanding the effects of QP modulations on quantum systems. Unlike random systems, QP systems are fully deterministic but have long range spatial correlations and, hence, standard techniques developed over the years for random systems, for example those based on the replica trick, do not carry forward to QP systems.

A system can be subjected to QP modulation by placing it under the superimposition of two (or more) periodic modulations with incommensurate frequencies, that is, the ratio of frequencies of modulations is an irrational number, γ. A natural example is of a periodic lattice (which acts as one of the two periodic modulations required) exposed to an incommensurate potential, resulting in a QP pattern. Recently, the effects of driving a quantum system with two or more incommensurate periodic drives have also received much interest [21, 22, 23, 24, 25, 26, 27, 28, 29, 30, 31] with new, and exotic non-equilibrium phases and steady states being discovered.

QP systems thus have a natural hierarchy of length or energy scales associated with writing the relevant irrational number, γ, as the limit of a sequence of best approximating rational numbers [1]. The best approximating sequence of rational

[1] A rational number, p/q, is a best approximation of γ if it is closest to γ among all rational a/b with $b < q$.

numbers, p_n/q_n, is obtained by cutting off the continuous fraction expansion of γ, $[a_0; a_1, a_2, ...]$, at various levels, giving $p_n/q_n \equiv [a_0; a_1, ..., a_n]$. The sequence $\{q_n\}$ are then seen as length scales at which the system is almost periodic: note that the numbers p_n, q_n satisfy $|q_n\gamma - p_n| < 1/q_n$ and applying Taylor expansion to a QP function $f(x)$, we get $f(x + q_n) - f(x) \lesssim 1/q_n$; an example of such a function is $f(x) = \cos 2\pi x + \cos 2\pi\gamma x$. This hierarchy of scales plays a key role in understanding the properties of QP systems. The spectrum of a QP Hamiltonian is well known to be a Cantor set with each splitting controlled by the coefficients of the continuous fraction [32, 33, 34, 35, 36, 37, 38, 39, 40, 41]. Moreover, the topology of the spectrum is robust to the changes in the underlying model, depending only on the incommensurate frequency. In fact, the topological nature of gaps in the bulk spectrum is similar to Landau levels and have been shown to have localized edge modes showing integer quantum hall effects of dimension higher than of the QP system [17, 42]. In general QP systems, derived using the so-called cut-and-project method [43], inherit properties from systems in higher dimensions [44].

There are also some systems that apparently lack any QP pattern in the geometry but have an emergent "QP structure" in their solutions. A famous example is the energy levels of $2d$ electrons in a magnetic field, which are known to show fractal structure (Hofstadter butterfly) for irrational values of magnetic flux [45, 46]. Another example is the Bethe Ansatz solutions for the easy-plane XXZ chain, with anisotropy parameter $-1 < \Delta < 1$; the nature of solutions differ greatly depending on whether $\lambda \equiv \cos^{-1}\Delta$ is irrational or rational [47], with the Drude weight, $\mathcal{D}_\lambda$, showing discontinuous fractal behavior [48, 49, 50, 51, 52, 53, 54], as shown in Figure 2.5. For $\lambda = p/q$, there are q types of quasiparticles and for irrational values of λ, there will be a hierarchy of time scales on which the system can be approximated by some rational λ_n, and consequently, new quasiparticles get "activated" as the system time evolves in time.

Unlike random systems, not much is known about the effects of QP modulations on quantum criticality. In the presence of random disorder, quantum critical systems in d dimension are driven to new fixed points marked by randomness, if the correlation length, ν, of the clean system violates the Harris bound $\nu > 2/d$ [55, 56]. For variety of quantum systems the resultant new random fixed points have infinite randomness and for which exact methods based on real space renormalization group (RSRG) exist [57, 58, 59, 60]. On the other hand, QP perturbations are relevant at the clean fixed point if the correlation length exponent satify a weaker condition, [2] $\nu < 1/d$ [61]. However, most of the studies involving QP modulations were either restricted to discrete aperiodic sequences or non-interacting systems [62, 63, 64, 65, 66, 67, 68, 69, 70, 71, 72, 73]. Recently this has been extended to continuous QP modulations for transverse Ising field model [74, 75, 76].

Non-interacting systems in the presence of inhomogeneity show delocalization to localization transitions. For QP systems, these transitions are known to occur even in $1d$ [77], as opposed to random systems where they exist only in $d \geq 3$. Recently, its generalization to interacting systems, also known as many-body localization transition (MBLT), has received widespread interest. Significant advancement has been made in understanding the MBLT in random systems, with the latest theories for the transition suggesting a Kosterlitz–Thousless (KT) like transition [78, 79, 80, 81]. However, the understanding of the corresponding transition for QP system is still in its infancy [82, 83, 84]. Also, the many-body localized (MBL) phase in 2d random systems has been argued to be unstable due to the presence of rare anomalous thermal inclusions capable of thermalizing the whole system [85, 86, 87]. Such rare regions are absent in QP modulations and consequently the MBL phase is expected to survive in 2d QP systems.

[2] This is true when the wandering constant, ω, is equal to zero, which is the case for continous QP modulations considered in this proposal.

In addition to the theoretical differences between random and QP systems, the latter can be conveniently realized in an *isolated* experimental setup. Solid materials are the primary sources for random systems but are difficult to isolate as the phonon modes present in the solid act as a heat bath by coupling to the electrons. On the other hand, due to advancements in cold atoms, and photonic lattices, it is relatively easy to create synthetic lattices with desired properties. For this reason, many recent experiments involving MBL [6, 7, 9, 13, 88, 89, 90, 91, 92, 93, 94, 95], have used QP modulations as a proxy for random inhomogeniety (and hence, QP is sometimes *misleadingly* dubbed as quasirandomness). Absence of Griffiths effects [96, 97] due to rare regions, small sample to sample fluctuations, and the relative ease of realizing them in experiments makes QP systems a better choice for use in engineering applications.

The rest of this section is organized as follows. In Chapter 2, we present two independent examples of anomalous transport in integrable systems. We first look into a fine-tuned non-interacting integrable model in the presence of random, but *correlated*, disorder. We study the model using generalized hydrodynamics, which was recently developed for studying the dynamics of integrable models [98, 99] and show slow anomalous relaxation. We also study quasilocalization transition and multifractal structure of eigenstates and tie them to the anomalous transport of quasiparticles. Our second example will be of anomalous low frequency conductance in the XXZ spin chain due to new quasiparticles getting "activated" in a hierarchical fashion on time scales coming from rational approximants of the irrational parameter in the Hamiltonian.

In Chapter 3 we study various quantum critical systems in 1d, and 2d under *continuous* QP modulations and describe their critical properties. We show that, under real space renormalization group (RSRG), the initially continuous QP modulation flows to discrete aperiodic sequences. We argue for "super-universality" for critical

properties in the sense that they are same for a large class of QP fixed points and for different microscopic models.

CHAPTER 2

ANOMALOUS TRANSPORT IN INTEGRABLE SYSTEMS

Addressing questions about non-equilibrium transport, thermalization and far-from-equilibrium dynamics pose notable challenges for theory as they are not susceptible to the general principles and methods that govern the physics of low-energy, equilibrium systems. With the notable exception of many-body localized systems [100, 101, 102], generic many-body systems are expected to be "chaotic", and to thermalize under their own dynamics [103]. Another class of systems that escape thermalization in the traditional sense are quantum integrable systems, including experimentally relevant examples like the Heisenberg antiferromagnet and the Lieb-Liniger Bose gas in one dimension [104, 105, 106]. Such systems have stable quasiparticle excitations even at high temperature, and they possess an extensive number of conserved quantities which strongly constrain their dynamics, and prevent them from thermalizing like generic chaotic systems [107, 108, 109, 110, 111, 52, 112, 113, 114, 115, 116]. However, contrary to many-body localized systems, integrable systems do thermalize in a generalized sense, as they eventually reach a maximum entropy steady state described by a generalized Gibbs ensemble (GGE) [117, 118, 119, 105]. Such steady-states can exhibit non-zero currents, and are commonly referred to as non-equilibrium steady states (NESS) in the literature [120, 101], even though they are natural equilibrium states for integrable systems.

In this chapter we study anomalous transport in two independent integrable systems. As the first example, we consider an integrable spin chain with quenched

correlated randomness. The correlation in randomness is defined precisely to preserve the integrable nature of the model. We focus on the non-interacting limit of the model for simplicity and concreteness. Unlike generic non-interacting systems, these special class of models escape Anderson localization and display stable ballistically propagating quasiparticles. We use the recently developed framework of generalized hydrodynamics (GHD) [99, 98], which we review in brief in Section. 2.1. We find that the quasiparticles have diffusive corrections to their ballistic trajectories which are expected to be absent for non-interacting systems [121]. Using GHD we also show that long range random distributions have quasiparticles with infinitesimally small velocity, reminiscent of localization. These particles are responsible for anomalously slow local relaxation, and a quasi-localization transition for low energy states driven by the parameter controlling the tail of the random distribution.

For our second example we consider the spin 1/2 easy-plane XXZ antiferromagnetic chain given by $H = J\sum_i (S_i^x S_{i+1}^x + S_i^y S_{i+1}^y + \Delta S_i^z S_{i+1}^z)$. The Drude weight, $\mathcal{D}_\lambda$, of the model is known to show fractal discontinuous behavior with respect to $\lambda \equiv \cos^{-1}\Delta$ [48, 49, 50, 51, 52, 53, 54], with $\mathcal{D}_\lambda$ showing discontinuous jumps for irrational λ, see Figure 2.5. We argue for the fractal behavior of $\mathcal{D}_\lambda$ to be closely related to the hierarchical nature of quasiparticles for irrational λ. The convergents of λ [1] give the timescales on which the system can be described by a rational approximant of λ (within some small error). The low frequency a.c conductivity (which depends on the late time behavior) follows the diverging sequence of d.c conductivities of models with rational approximants of λ, leading to the anomalous divergence of the conductivity (instead of a finite value expected for a generic diffusive systems.) This is very similar to QP modulated systems where the convergents provide the length scales on which the system is almost periodic and is well described by the Bloch theorem; QP

[1] Recall that convergents of an irrational number $\lambda \equiv [a_0; a_1, a_2, \dots]$ is given by q_n, where $p_n/q_n \equiv [a_0; a_1, \dots, a_n]$.

properties are restored on taking the limit of convergents going to infinity [122, 123]. However, unlike the QP modulated system, the QP nature of XXZ model is not due to the geometry of the system but rather is intrinsic to the Bethe ansatz solution of the model.

2.1 Generalized Hydrodynamics – a brief review

A major step in understanding the non-equilibrium dynamics of quantum integrable systems was the formulation of what is now known as "generalized hydrodynamics" (GHD) [99, 98], which are Euler hydrodynamics equations (0th order hydrodynamics) obtained in the large space-time limit where the system is locally in equilibrium. While the prospect of solving infinitely-many hydrodynamic equations (one for each conserved quantity in the system) originally appeared daunting, GHD can be conveniently formulated in the basis of quasiparticle excitations: in that language, they can be naturally interpreted as describing a semi-classical gas of solitons (quasiparticles) [124, 125, 126, 127].

One imagines chopping off the system into hydrodynamic cells that are big enough to assume equilibrium within each cell, but very small compared to the total system size. This separation of scales allows one to assume local equilibrium, where Lagrange multipliers like temperature or chemical potential are allowed to depend on position and time.

There is one hydrodynamic equation per conserved quantity in the system – any other information about the system is "scrambled" by the quantum dynamics into non-local entanglement that is not measurable by local observables. For each conserved quantity $Q_n = \sum_x q_n(x)$, we can write a continuity equation

$$\partial_t q_n(x,t) + \partial_x j_n(x,t) = 0, \tag{2.1}$$

where we restricted ourselves to one spatial dimension. Assuming local equilibrium then leads to a relation $j_n = F_n[\{q_m\}]$ between the currents j_n and the conserved charges q_m at a given position x: this relation is an equilibrium property and gives rise to *Euler* hydrodynamic equations that govern ballistic transport properties. More generally, one can perform a gradient expansion of the (expectation value of the) currents in terms of the charges, where contributions to the currents coming from gradient terms $D_{nm}\partial_x q_m$ correspond to diffusive contributions to hydrodynamics (see *e.g.* [128]). The diffusion constants D_{nm} are not entirely given by equilibrium properties, and have to be determined by other means such as the Kubo formula, or by using kinetic theory calculations. Once the transport coefficients characterizing the relation between currents and charges are known, hydrodynamics provides a simple set of classical, partial differential equations that govern the non-equilibrium dynamics of the system.

The hydrodynamic framework summarized above is completely general, and it was successfully applied to integrable systems [99, 98]: the resulting framework is now known as *generalized hydrodynamics* (GHD), as it describes systems in local generalized Gibbs ensemble equilibrium. There, local equilibrium is characterized by the densities of particles, $\rho_{j,\lambda}(x,t)$, and holes, $\rho^h_{j,\lambda}(x,t)$, with the charges $q_n(x) = \sum_j \int q_{n,j,\lambda}\rho_{j,\lambda}(x)d\lambda$ and currents $j_n(x) = \sum_j \int v^{\text{eff}}_{j,\lambda}(x) q_{n,j,\lambda}\rho_{j,\lambda}(x)d\lambda$ (ignoring gradient (diffusive) corrections). v^{eff}_j is interpreted as a group velocity which is a functional of the quasiparticle density in general. The continuity equations for the conserved charges then imply a continuity equation for the quasiparticle density [99, 98]

$$\partial_t \rho_{j,\lambda} + \partial_x (v^{\text{eff}}_{j,\lambda}\rho_{j,\lambda}) = 0, \tag{2.2}$$

The GHD framework was recently generalized to include diffusive effects in interacting integrable models [129, 130, 131, 132] – corresponding to "1st order" or Navier-Stokes hydrodynamics, with important consequences for the nature of spin

transport in XXZ spin chains [131, 132]. There are two key ingredients needed to have diffusion: density dependent velocities, and thermal fluctuations. This immediately implies that in non-interacting integrable models where the group velocity is obtained from band theory and is independent of density, there should be no diffusion [121]. For non-interacting systems, it is thus natural to expect that the lowest order correction to ballistic GHD comes from higher order derivative terms, which lead to $t^{1/3}$ spreading governed by the Airy kernel (see Ref. [133] and references therein).

2.2 Random integrable spin chains

In this section, we introduce a family of random integrable spin chains, following closely Ref. [134], and study their transport properties using GHD. Let us consider a random XXZ spin-$\frac{1}{2}$ chain $H = \sum_i J_i \left[\boldsymbol{\sigma}_i.\boldsymbol{\sigma}_{i+1}\right]_{\Delta_i}$, where $\left[\boldsymbol{\sigma}_j.\boldsymbol{\sigma}_k\right]_{\Delta_i}$ is a shorthand notation for $\sigma_j^x\sigma_k^x + \sigma_j^y\sigma_k^y + \Delta_i(\sigma_j^z\sigma_k^z - 1)$. In the clean (homogeneous) case, this model is integrable, but the introduction of disorder immediately breaks integrability, and leads to a model that is either chaotic or many-body localized [135, 136]. However, it is possible to preserve integrability [137, 138, 134] by introducing next-to-nearest neighbor interactions, and by carefully choosing the inhomogeneous couplings:

$$\begin{aligned} H = \sum_{j=1}^{L/2} & J_{2j}^{(1)} \left(\left[\boldsymbol{\sigma}_{2j-1}.\boldsymbol{\sigma}_{2j}\right]_{\Delta_{2j}} + \left[\boldsymbol{\sigma}_{2j}.\boldsymbol{\sigma}_{2j+1}\right]_{\Delta_{2j}} \right) \\ & + K_{2j} \left(\left[\boldsymbol{\sigma}_{2j}.\left(\boldsymbol{\sigma}_{2j-1} \times \boldsymbol{\sigma}_{2j+1}\right)\right]_{\Delta_{2j}^{-1}} + \Delta_{2j}^{-1} \right) \\ & + J_{2j}^{(2)} \left(\boldsymbol{\sigma}_{2j-1}.\boldsymbol{\sigma}_{2j+1} - 1\right). \end{aligned} \tag{2.3}$$

The first line of the hamiltonian corresponds to an XXZ interaction, while the last line is an isotropic Heinsenberg interaction. The middle line is more unusual, as it involves three spins. The parameters in the hamiltonian are given by

$$J_{2j}^{(1)} = \frac{\sin^2\eta\ \cosh\xi_{2\mathrm{j}}}{\sin^2\eta + \sinh^2\xi_{2\mathrm{j}}}, \quad J_{2j}^{(2)} = \frac{\cos\ \eta\ \sinh^2\xi_{2\mathrm{j}}}{\sin^2\eta + \sinh^2\xi_{2\mathrm{j}}},$$
$$K_{2j} = \frac{\sin\ \eta\ \cos\ \eta\ \sinh\xi_{2\mathrm{j}}}{\sin^2\eta + \sinh^2\xi_{2\mathrm{j}}}, \quad \Delta_{2j} = \frac{\cos\ \eta}{\cosh\ \xi_{2\mathrm{j}}}, \tag{2.4}$$

with ξ_{2j} a random coupling, while η is an overall global parameter that parametrizes the interaction strength. For $\xi_{2j} = 0$, one recovers the usual XXZ spin chain. A remarkable feature of this model is that it remains integrable for any choice of the inhomogeneous couplings ξ_{2j}. Away from the zero-energy limit, the properties of this model are insensitive to details of the disorder distribution. Therefore, except as specified below we will take the ξ_{2j} couplings to be random variables drawn from the gaussian distribution

$$P(\xi) = \frac{1}{\sqrt{2\pi W^2}} e^{-\xi^2/2W^2}. \tag{2.5}$$

Later, we will also consider the exponential distribution,

$$P(\xi) = \frac{\phi}{2} e^{-\phi|\xi|}. \tag{2.6}$$

We will be especially interested in the special point $\eta = \pi/2$. For this value of η, the XXX part of the Hamiltonian is set to zero, leaving behind a random XX model with three spin interactions,

$$H = \sum_{j=1}^{L/2} \left[\frac{1}{\cosh\ \xi_{2\mathrm{j}}} \sum_{\alpha=x,y} \left[\sigma_{2j-1}^{\alpha}\sigma_{2j}^{\alpha} + \sigma_{2j}^{\alpha}\sigma_{2j+1}^{\alpha}\right] \right. \tag{2.7}$$
$$\left. + \tanh(\xi_{2\mathrm{j}}) \left[\sigma_{2\mathrm{j}-1}^{\mathrm{y}}\sigma_{2\mathrm{j}}^{\mathrm{z}}\sigma_{2\mathrm{j}+1}^{\mathrm{x}} - \sigma_{2\mathrm{j}-1}^{\mathrm{x}}\sigma_{2\mathrm{j}}^{\mathrm{z}}\sigma_{2\mathrm{j}+1}^{\mathrm{y}}\right] \right].$$

The above hamiltonian can be diagonalized via Jordan-Wigner transformation reducing it to a free fermion model

$$H = -\sum_{j=1}^{L} \frac{2}{\cosh(\xi_{\rm j})} \left(c_j^\dagger c_{j+1} + \text{h.c.} \right) + \sum_{j=1}^{L/2} 2i \tanh(\xi_{2\rm j}) \left(\rm c_{2j-1}^\dagger c_{2j+1} - h.c. \right), \tag{2.8}$$

where the ξ_j's are random parameters used in (2.3), extended to odd sites via relation, $\xi_{2j-1} = \xi_{2j}$. We use periodic boundary conditions for the fermions for an even number of sites. While non-interacting and disordered, this model was shown to escape Anderson localization in Ref. [134], and to exhibit ballistic transport of conserved quantities. It is then natural to ask if transport properties of this model can be captured using generalized hydrodynamic equations, properly adapted to deal with the quenched disorder. If so, it is natural to expect disorder to lead to new hydrodynamic effects, such as diffusion. In the following, we will mostly focus on the special point $\eta = \pi/2$ (eqs. (2.8) (2.7)), though we expect our approach to generalize to any value of η. This will be convenient as the free fermion representation of this model allows one to simulate numerically the non-equilibrium dynamics of this system easily, and more importantly, the absence of interactions will allow us to isolate the effect of disorder on diffusion.

In the non-interacting limit of $\eta = \pi/2$, there are two kind of quasiparticles, or strings, $j = 1, 2$, and their group velocity is simply given by [99, 98]

$$v_{j,\lambda}^{\rm eff} = \frac{e_j'(\lambda)}{p_j'(\lambda)} = q_j \frac{e_j'(\lambda)}{2\pi \rho_{j,\lambda}^T}, \tag{2.9}$$

where e_j is the quasiparticle energy given by

$$e_j(\lambda) = 4J A_j(\lambda), \tag{2.10}$$

p_j the quasiparticle momentum, and the total density of states $\rho_{j,\lambda}^T = \rho_{j,\lambda} + \rho_{j,\lambda}^h$ is given [139, 134] by the Bethe equation (which is particularly simple since the model

is non-interacting)

$$\rho^T_{j,\lambda} = q_j \frac{1}{N} \left(\sum_{k=1}^{N/2} A_j \left(\lambda + \frac{4}{\pi} \xi_{2k} \right) + \frac{N}{2} A_j(\lambda) \right), \tag{2.11}$$

for a system of size N, with the function $A_j(\lambda)$ defined as

$$A_j(\lambda) = \frac{\pi}{4} \frac{q_j}{\cosh(\pi\lambda/2)}. \tag{2.12}$$

In these equations, $q_1 = 1, q_2 = -1$. In the interacting case, all these quantities would be "dressed" and would become functional of the quasiparticle densities ρ_j.

As expected since the model is non-interacting, the group velocity does not depend on the density ρ of the other quasiparticles. However, it does depend on the inhomogeneous variables ξ_i. It is thus clear that some kind of averaging over these random variables needs to be done in order to formulate a hydrodynamic theory of this random quantum spin chain.

2.2.1 Averaging and coarse-graining

In order to average the random variables ξ_i, we go back to the physical picture of hydrodynamics and divide the system into mesoscopic hydrodynamic cells large enough to be in the thermodynamic limit. Let the system length be L and it be divided in $N \gg 1$ sub-cells of size $\Delta x = L/N \gg a$ with a the lattice spacing. For a given disorder realization, the velocity in each hydrodynamic cell is given by (2.9). These velocities depend on our choice of sub-cell division, but as we will see this dependence drops out of the final result.

Given these velocities we can easily construct the trajectory of a given quasiparticle from its initial position $x = 0$. Let us find the time required for a quasiparticle

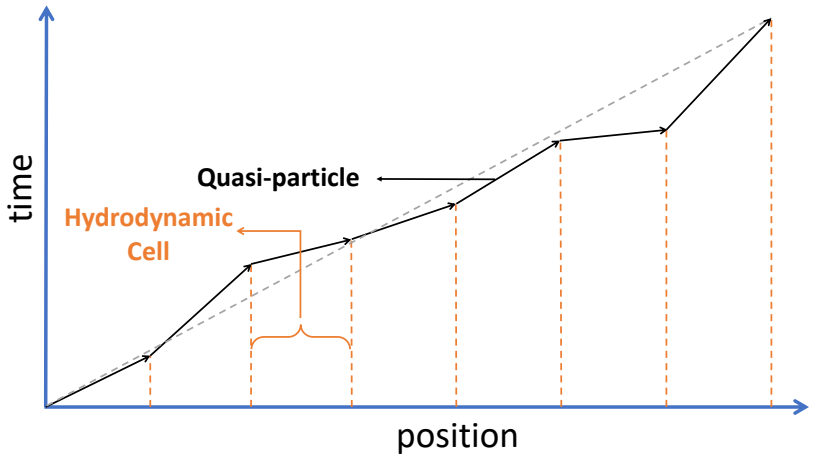

Figure 2.1. A cartoon depicting the diffusion spreading of a quasiparticle, which can be thought of as random collisions with impurities in each hydrodynamic cell it encounters along it's trajectory.

of type j with rapidity λ, initially at $x = 0$ to reach $x = M\Delta x$. It is given by [2],

$$t_x = \Delta x \sum_{i=1}^{M} \frac{1}{v_i}, \tag{2.13}$$

with v_i the velocity the i^{th} cell. We then have using (2.9)

$$t_x = \Delta x \frac{2\pi}{e'} \sum_{i=1}^{M} \rho_i^T. \tag{2.14}$$

Since ρ^T is a sum of random variables, we can use the central limit theorem to deduce that both ρ^T and t_x are Gaussian distributed (provided the hydrodynamic cells are large enough, and $M \gg 1$). This also shows that the result is largely independent of the distribution chosen for the random parameter ξ, as long as the central limit theorem is applicable, as is the case for the distributions considered in this paper.

[2]We will momentarily omit the string number and rapidity/momentum subscripts to make the equations more readable.

Thus we have following result: the time taken for a quasiparticle to move over a distance x is Gaussian distributed, with the average time being given by

$$\overline{t_x} = x\frac{2\pi\overline{\rho^T}}{e'}, \tag{2.15}$$

where $\overline{\rho^T}$ is the disorder average of ρ^T. This quantity is clearly independent from our choice of hydrodynamic cells – it only depends on x, not M, or Δx. The standard deviation reads

$$\sigma[t_x] = \sqrt{\frac{\Delta x}{2N_{\text{sub}}}}\sqrt{x}\frac{2\pi\sigma\left[A(\lambda+\frac{2}{\eta}\xi)\right]}{e'},$$

where N_{sub} is the number of lattice sites inside a cell, and $\sigma[A(\lambda+\frac{2}{\eta}\xi)]$ is the standard deviation of the function defined in equation (2.12). Note that $\sqrt{\frac{\Delta x}{2N_{sub}}} = \sqrt{\frac{a}{2}}$ with a the lattice spacing, implying that the standard deviation of t_x is also independent of our choice of hydrodynamic cells. Thus we conclude that the distribution of t_x does not depend on the partition of hydrodynamic cells, and is well defined.

We define the average velocity $v^\star$ via the relation $v^\star\overline{t_x} = x$. This yields

$$v^\star = \frac{e'}{2\pi\overline{\rho^T}} = \overline{(v^{\text{eff}})^{-1}}^{-1}. \tag{2.16}$$

Note that this is *not* the average of v^{eff} over disorder.

The probability distribution of the time it took for quasiparticle to move over a distance x thus reads

$$P_x(t) = \frac{1}{\sqrt{2\pi\Gamma x}}e^{-(t-x/v^\star)^2/2\Gamma x}, \tag{2.17}$$

$$\Gamma(\lambda) \equiv \left(\frac{2\pi\sigma[A(\lambda+\frac{2}{\eta}\xi)]}{e'}\right)^2\frac{a}{2}. \tag{2.18}$$

This process is called *temporal diffusion* [140, 141], as it looks like an usual diffusion process where the roles of space and time are exchanged. However, in the hydrodynamic limit, the spreading of the distribution is confined to region $(x/v^\star - t)^2 = \mathcal{O}(\Gamma x)$

or $x = v^\star t \left(1 + \mathcal{O}(\sqrt{\frac{\Gamma v^\star}{t}})\right)$. Thus in the limit $\frac{\Gamma v^\star}{t} \ll 1$ we can replace x by $v^\star t$ and get

$$P(x,t) \approx \frac{1}{\sqrt{2\pi\Gamma(v^\star)^3 t}} e^{-(x-v^\star t)^2/2\Gamma(v^\star)^3 t}, \tag{2.19}$$

which corresponds to a biased random walk. A similar temporal diffusion equation recently appeared in the context of energy transport in a random conformal field theory [141]. In all the numerical results below, we have checked that the difference between the temporal and ordinary diffusion descriptions are negligible in the hydrodynamic limit.

For generic initial condition of the quasiparticles, $\rho^0(x, t = 0)$, the evolution should thus reads

$$\rho(x,t) = \int \frac{1}{\sqrt{4\pi D t}} e^{-(x-x_0-v^\star t)^2/4Dt} \rho^0(x^0) dx^0, \tag{2.20}$$

with $D = \Gamma(v^\star)^3/2$ since the quasiparticles are non-interacting. Reintroducing the string and rapidity labels, we find that the quasiparticle density satisfies the following hydrodynamic equation

$$\boxed{\partial_t \rho_{j,\lambda}(x,t) + v^\star_{j,\lambda} \partial_x \rho_{j,\lambda}(x,t) = D_{j,\lambda} \partial_x^2 \rho_{j,\lambda}(x,t),} \tag{2.21}$$

where $D_{j,\lambda} \equiv \frac{\Gamma_{j,\lambda}(v^\star_{j,\lambda})^3}{2}$ is a diffusion constant due to the disorder. We emphasize that the transport coefficients $v^\star$ and D in this equation *do not* depend on the details of our coarse graining procedure – in particular, they do not depend on the size of the hydrodynamic cells Δx as long as $L \gg \Delta x \gg a$.

2.2.2 Energy and spin transport

We now use the hydrodynamic equation derived above to study non-equilibrium energy and spin transport in the random spin chain (2.7). This will also allow us to benchmark and test the validity of the hydrodynamic approach, and investigate the

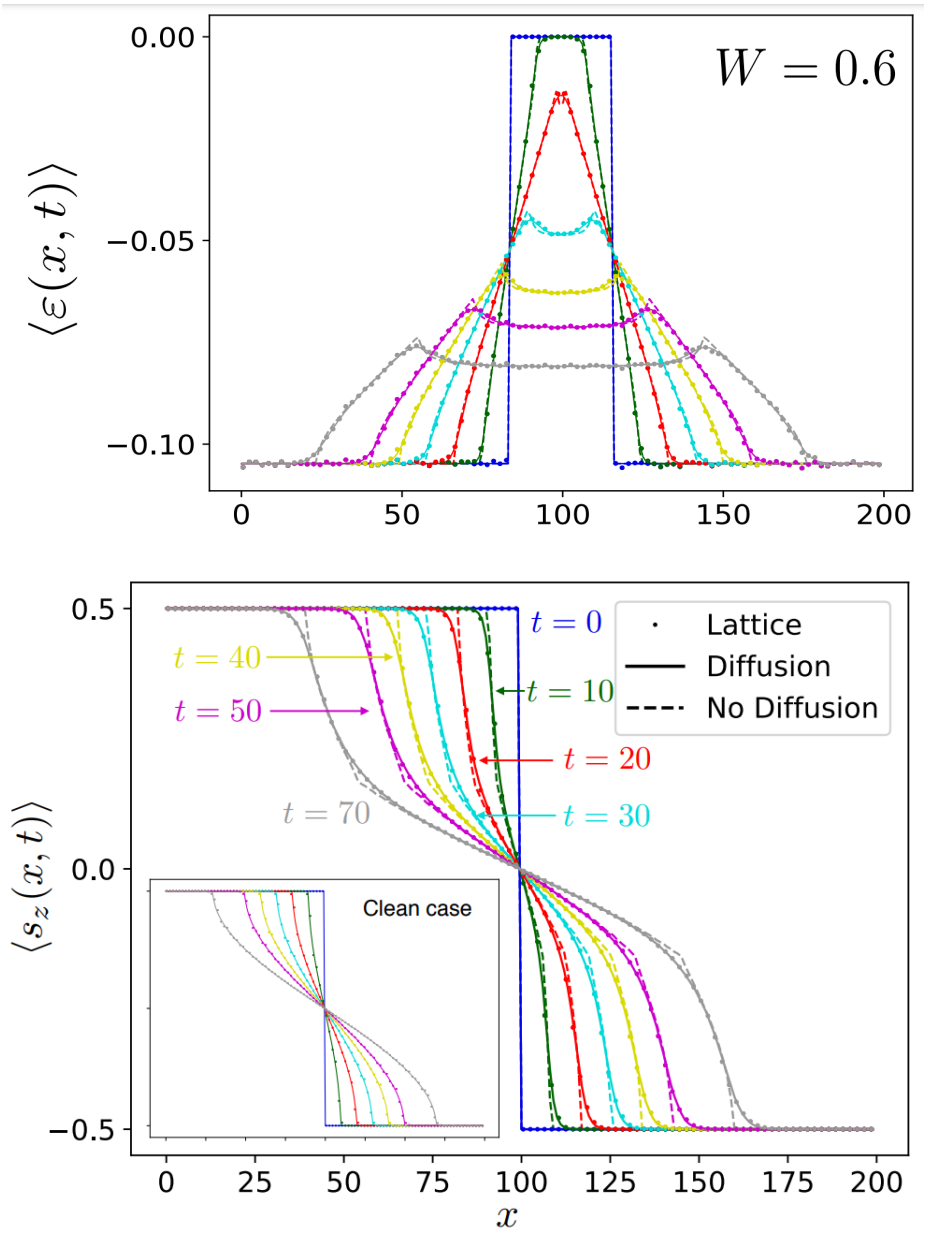

Figure 2.2. Energy and spin transport.Upper panel: the evolution of the energy density as a function of time for $W = 0.6$ in eq. (2.5), for an initial state at temperature $T = 1$ with a small region of the system locally at infinite temperature. We compare exact numerical results, and the hydrodynamic prediction from the solution of eq. (2.21), with and without the diffusive term. The numerical data was averaged over $\sim 3 \times 10^3$. **Lower panel:** comparison of the hydrodynamic prediction (2.21) with numerical results a for spin domain wall initial state. The disorder strength is $W = 0.6$, and numerical results are averaged over $\sim 2 \times 10^3$ disorder realizations. The hydrodynamic equation including diffusive terms (solid line) is describing the numerical results much more accurately than the purely ballistic prediction (dashed line). This establishes the presence of diffusive terms in the hydrodynamic description of this non-interacting system, even for an initial state that does not incorporate thermal fluctuations.

importance of the diffusive terms due to disorder. The energy and spin densities can be expressed in terms of the quasiparticle densities as

$$\epsilon(x,t) = \sum_j \int \rho_{j,\lambda}(x,t) e_j(\lambda)\ d\lambda, \tag{2.22}$$

$$s_z(x,t) = \frac{1}{2} - \sum_j n_j \int \rho_{j,\lambda}(x,t)\ d\lambda, \tag{2.23}$$

where n_j is given in our case by: $n_1 = n_2 = 1$. Figure 2.2 show the numerical data against the prediction from eq. (2.21). The agreement between the numerics and hydrodynamics is excellent, and we find that diffusive corrections are needed to accurately describe the numerical data, especially at stronger disorder.

2.2.3 Quasi-localization and anomalous transport

So far, our discussion has focused on macroscopic energy and spin transport, which is dominated by fast quasiparticles. In addition to these typical, fast, quasiparticles, however, these models also have slow quasiparticles at energy $|E| \approx 0$. These are important, e.g., for low-temperature transport, as well as for the behavior of local autocorrelation functions at late times. We discuss the nature of these quasiparticles here. We first explore the properties of wavefunctions, both numerically and analytically, and find that these undergo a quasi-localization transition for the exponential disorder distribution (2.6). We then apply the thermodynamic Bethe ansatz results to study the asymptotic behavior of the velocity and density of states as $|E| \to 0$.

To consider the behavior of quasiparticles in the $|E| \to 0$ limit note that from eq. (2.10), these quasiparticles correspond to large $|\lambda|$: in fact, $e_j(\lambda) \sim e^{-\pi|\lambda|/2}$. In what follows we suppress the index j and denote the energy as E. The limiting behavior of the velocity and the density of states is sensitive to the tails of the disorder distribution. For the sample-averaged density of states, Eq. (2.11) yields

$$\rho_{1,\lambda}^{T} = \left\langle \frac{\pi}{8\cosh(\pi\lambda/2 + 2\xi)} \right\rangle_{\text{dis}} + \frac{\pi}{8\cosh(\pi\lambda/2)}, \tag{2.24}$$

where $\langle \dots \rangle_{\text{dis}}$ denotes the average over disorder. If the disorder is bounded or falls off faster than exponentially, one can safely approximate $\cosh(x) \approx e^x/2$ for large enough λ. The quasiparticle velocity (given by Eq. (2.9)) therefore remains nonzero in the $\lambda \to \infty$ limit, so transport is asymptotically ballistic (but with a slower velocity). Likewise, the density of states also remains finite.

However, for distributions $P(\xi)$ with exponential or slower tails, computing the expectation value (2.24) is more subtle. We focus on the exponential case $P(\xi) = \frac{1}{2\phi}\exp(-\phi|\xi|)$. In this case, the expectation value (2.24) reads

$$\frac{\phi\pi}{4}\int_{-\infty}^{\infty} d\xi \frac{e^{-\phi|\xi|}}{\cosh(\pi\lambda/2 + 2\xi)}. \tag{2.25}$$

To get compact expressions for the asymptotics, we approximate $\cosh(\pi\lambda/2 + 2\xi) \approx \frac{1}{2}e^{|\pi\lambda/2+2\xi|}$. There are two cases. When $\phi > 2$, the integral is dominated by small $|\xi|$ and we get

$$\left\langle \frac{\pi}{8\cosh(\pi\lambda/2 + 2\xi)} \right\rangle_{\text{dis}} \approx \frac{\phi\pi e^{-\pi\lambda/2}}{2(\phi-2)}(1 - e^{-(\phi-2)\pi\lambda/2}) + \dots \tag{2.26}$$

where $\dots$ indicates terms that do not become singular in the limit $\phi \to 2$. Thus the zero-energy density of states and velocity remain finite when $\phi > 2$, but respectively diverge and vanish as $\phi \to 2^+$. Note that there are nonanalytic corrections to the density of states, even in this regime: specifically, $|\rho(E) - \rho(0)| \sim E^{\phi-2}$.

In the opposite limit $\phi < 2$, Eq. (2.24) is dominated by $|\xi| \approx \pi\lambda/4$. In this case we have instead

$$\left\langle \frac{1}{\cosh(\pi\lambda/2 + 2\xi)} \right\rangle_{\text{dis}} \sim e^{-\phi\pi\lambda/4}. \tag{2.27}$$

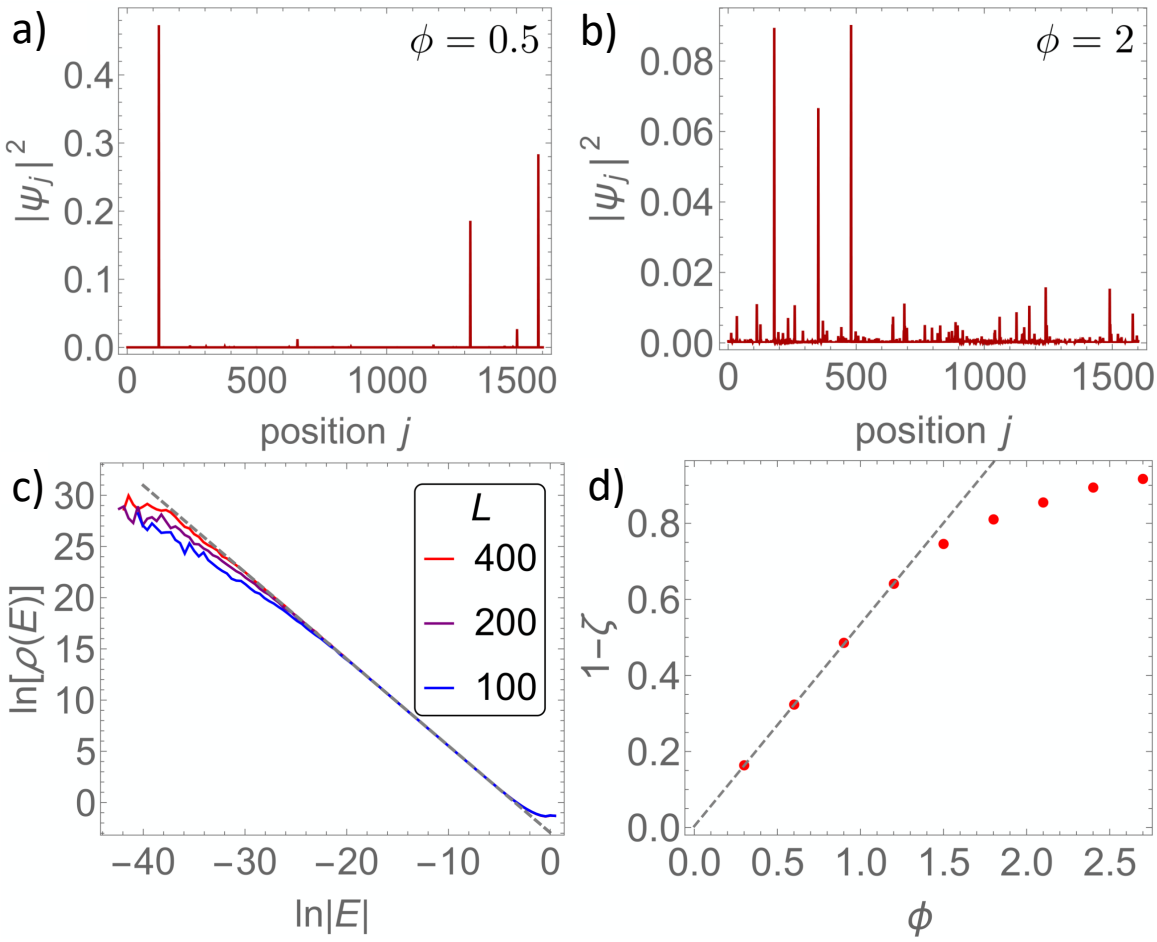

Figure 2.3. Density of states and quasi-localization. (a), (b) Spatial structure of single low-energy eigenstates for $\phi = 0.5$ (quasi-localized) and $\phi = 2$ (multifractal), for system size $L = 2000$. (c) Log-log plot of density of states for various system sizes, in the case where ξ_k are distributed exponentially with the parameter $\phi = 0.3$. The density of states diverges as $|E|^{-\zeta}$ at low energies. (d) Exponent $1 - \zeta$ vs. ϕ. For small ϕ we find a good linear fit to $\zeta = 1 - 0.53\phi$, which is in reasonable agreement with the Bethe ansatz prediction $\zeta = 1 - \phi/2$ (see main text).

The velocity then vanishes as $v(\lambda) \sim \exp[-(\pi\lambda/2)(1 - \phi/2)]$, or equivalently $v(E) \sim |E|^{1-\phi/2}$. Correspondingly the density of states $\rho(E)$ diverges as

$$\rho(E) \sim |E|^{-1+\phi/2}. \tag{2.28}$$

This behavior of the density of states is borne out numerically (Figure 2.3)

In short, when $\phi > 2$ the velocity approaches a finite value as $|E| \to 0$, so quantities such as the local autocorrelation function behave in an asymptotically ballistic fashion. On the other hand when $\phi < 2$ the velocity vanishes as $|E| \to 0$, and the local autocorrelation function will in general be anomalous. It is interesting to note that despite the very local character of the rare low-energy states, they appear naturally as slow quasiparticles in the hydrodynamics framework.

Slow local relaxation. We now turn briefly to the part of the local operator that remains near its initial position at late times. Since we are considering a noninteracting model, we can equivalently consider the return probability of an initially local wavepacket.

This quantity is proportional to the (mean) local autocorrelation function $C_0(t) = \overline{\langle S_i^z(t) S_i^z(0)\rangle}$. We focus on i even and infinite temperature. In generalized hydrodynamics this can be expressed as

$$C_0(t) \sim \sum_{j=1,2} \int d\lambda \langle \rho(\lambda) m_j(\lambda)^2 \Theta(a - |v(\lambda)t|)\rangle_{\text{dis.}}, \tag{2.29}$$

where at infinite temperature for a free-fermion model, $\rho^T \sim \rho$, $a = 1$ is the lattice spacing, and $m_j(\lambda) = n_j = 1$ is the spin of the quasiparticles. Focusing on low-energy quasiparticles, this integral can be written out as

$$C_0(t) \sim \int d\lambda \, d\xi \, e^{-\phi|\xi|} \rho^T(\lambda, \xi) \Theta(1 - |v(\lambda, \xi)t|). \tag{2.30}$$

We now resolve the step function and approximate $\rho_t(\lambda, \xi) \simeq e^{-\pi\lambda/2 + 2\xi} \Theta(\lambda - 4\xi/\pi)$, as done above, to rewrite this expression in terms of the double integral

$$C_0(t) \sim \int_{\frac{1}{2}\log t}^{\infty} d\xi \int_{4\xi/\pi}^{\infty} d\lambda e^{-\pi\lambda/2} e^{(2-\phi)\xi} \sim t^{-\phi/2}. \tag{2.31}$$

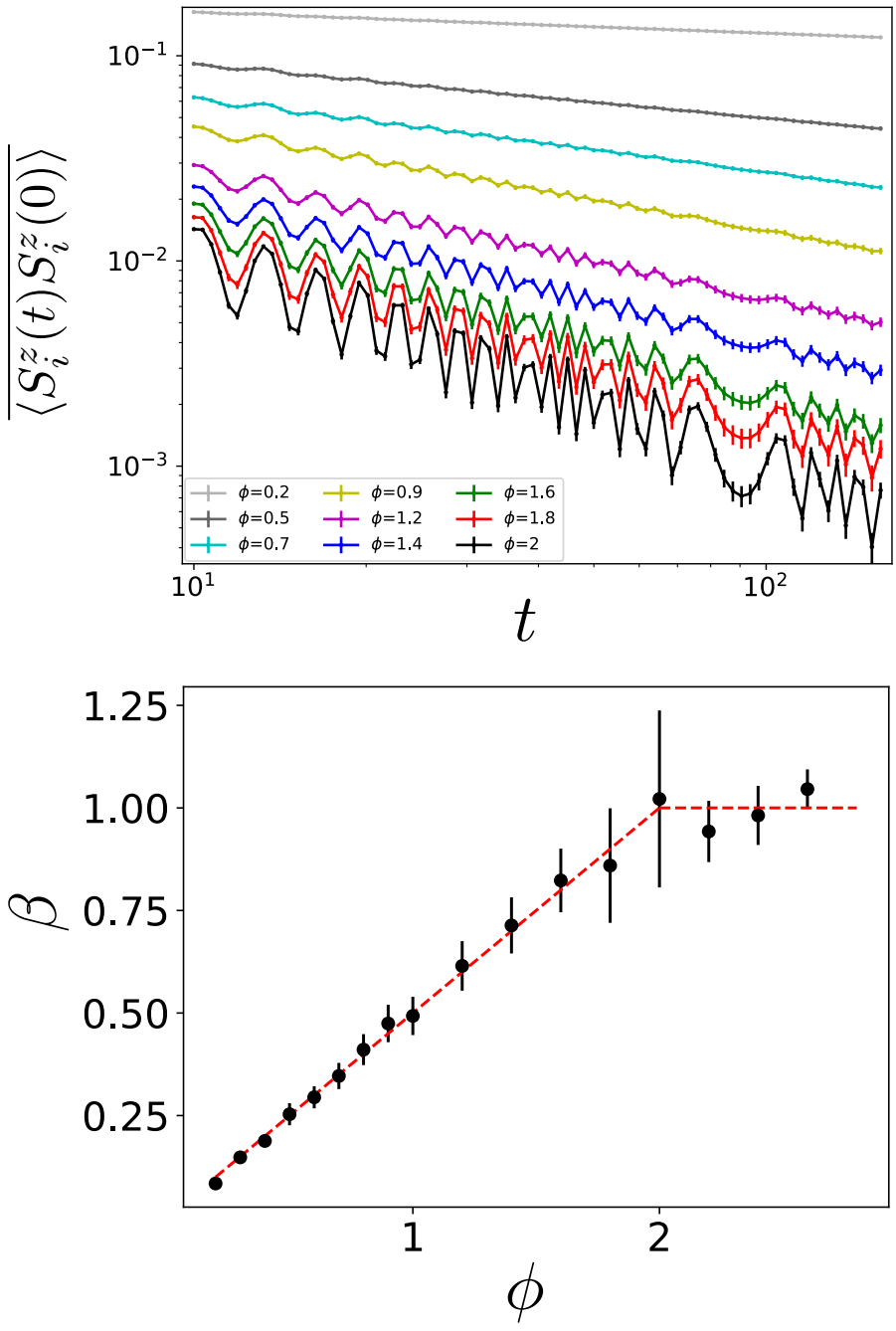

Figure 2.4. Anomalous local relaxation. *Top panel*: Algebraic decay of the average local structure factor $C_0(t)$ as a function of time, for various disorder strengths ϕ. This power-law decay for small values of ϕ can be observed up to very long times. *Bottom panel*: Decay exponent of the average local correlation function $C_0(t)$, as a function of disorder strength ϕ. We find that $C_0(t) \sim t^{-\beta}$, where $\beta \approx \phi/2$ throughout the quasi-localized phase $\phi < 2$. The generalized hydrodynamics prediction $\beta = \phi/2$ is indicated by a dashed red line. When $\phi > 2$ one has conventional ballistic behavior $C_0(t) \sim 1/t$.

Higher energy quasiparticles give rise to a ballistic decay $1/t$ that is subleading when $\phi < 2$. Thus, throughout the quasi-localized phase the autocorrelation function decays slower than one would expect for a model with ballistic transport. Numerical simulations of the autocorrelation function gives results in very good agreement with this exponent (Fig. 2.4). We emphasize that in the argument above, it was crucial to disorder-average the full autocorrelation function—separately averaging the velocity and the density of states would yield an incorrect exponent $\phi/(2-\phi)$ in clear disagreement with our numerical results. The local velocity is inversely proportional to the local density of states, and capturing these correlations is essential to deriving the correct anomalous exponent.

2.3 Anomalous conductivity in the easy-plane XXZ chain

This section addresses the a.c. conductivity of the XXZ spin-$\frac{1}{2}$ chain which is paradigmatic model for magnetism and is known to approximate many magnetic materials and experiments. The model is governed by the Hamiltonian

$$H = J\sum\nolimits_i (S_i^x S_{i+1}^x + S_i^y S_{i+1}^y + \Delta S_i^z S_{i+1}^z). \tag{2.32}$$

Here, $S_i^\alpha = \sigma_i^\alpha/2$ are spin-$\frac{1}{2}$ operators with σ_i^α the Pauli matrices on site i, the parameter Δ is the anisotropy, and J is an overall coupling scale that we will set to unity. We consider the "easy-plane" regime $-1 < \Delta < 1$, so we can parameterize $\Delta \equiv \cos(\pi\lambda)$. The Bethe ansatz solution for the above Hamiltonian is known to depend on the continous fraction expansion of λ [47]: for rational λ there is a finite number of quasiparticles while for irrational values, the system has infinite number of quasiparticle species. This, as we will show below, plays a crucial role for spin transport, leading to a a.c conductivity diverging as $\sigma(\omega) \sim 1/\sqrt{\omega}$.

For concreteness we assume the system is at infinite temperature, far from luttinger liquid regime, and in the thermodynamic limit (though the physics is presum-

ably qualitatively similar at any $T > 0$ [50]). Spin transport in this model is ballistic, so the spin conductivity takes the form $\sigma(\omega) = \mathcal{D}_\lambda \delta(\omega) + \sigma_\lambda^{\text{reg.}}(\omega)$. Much is known, through exact bounds as well as GHD [48, 49, 50, 51, 52, 53, 54], about the behavior of $\mathcal{D}_\lambda$ (which is called the Drude weight); however, the finite-frequency part has only been studied numerically [142, 143, 144, 145, 146]. The apparent behavior of $\mathcal{D}_\lambda$ is remarkable: it appears to be discontinuous and fractal as a function of λ (see Fig. 2.5). When $\lambda = p/q$ is rational, several distinct methods [48, 49, 50, 51, 52, 53, 54] lead to the conclusion that

$$\mathcal{D}_\lambda = \frac{1}{12}(1-\Delta^2) f\left(\frac{\pi}{q}\right), \quad f(x) = \frac{3}{2}\left[\frac{1-\frac{\sin(2x)}{2x}}{\sin^2 x}\right]. \tag{2.33}$$

Eq. (2.33) is a rigorous lower bound on $\mathcal{D}$, which GHD [147, 53, 126, 51] predicts is saturated. Remarkably, Eq. (2.33) allows the Drude weight to jump by $\mathcal{O}(1)$ as Δ changes infinitesimally: $\lim_{x\to 0} f(x) = 1$ for any irrational number λ, but is higher by an $\mathcal{O}(1)$ amount at an arbitrarily close small-denominator rational. This has been a mystery for long times for how can any physical quantity be fractal. These jumps in the zero-frequency spectral weight strongly suggest that the finite-frequency behavior must also be nontrivial, so that the physical properties measured at finite times show continuous behavior.

The high-temperature limit of $\sigma(\omega)$ is given by the Kubo formula

$$\sigma_\lambda(\omega) = \beta \int_0^\infty dt \sum_x C_{jj}(x,t) e^{i\omega t} = \pi \mathcal{D}_\lambda \delta(\omega) + \sigma_\lambda^{\text{reg}}(\omega), \tag{2.34}$$

in terms of the autocorrelator $C_{jj}(x,t)$ of the current $j(x) \equiv -i(S_x^+ S_{x+1}^- - \text{h.c.})$:

$$C_{jj}(x,t;\lambda) \equiv Z^{-1} \text{Tr}\left[e^{iH_\lambda t} j(x) e^{-iH_\lambda t} j(0) e^{-\beta H_\lambda}\right]. \tag{2.35}$$

Here, Z is the partition function and β is the inverse temperature. In what follows we will suppress the subscript (since we discuss only one correlation function) and

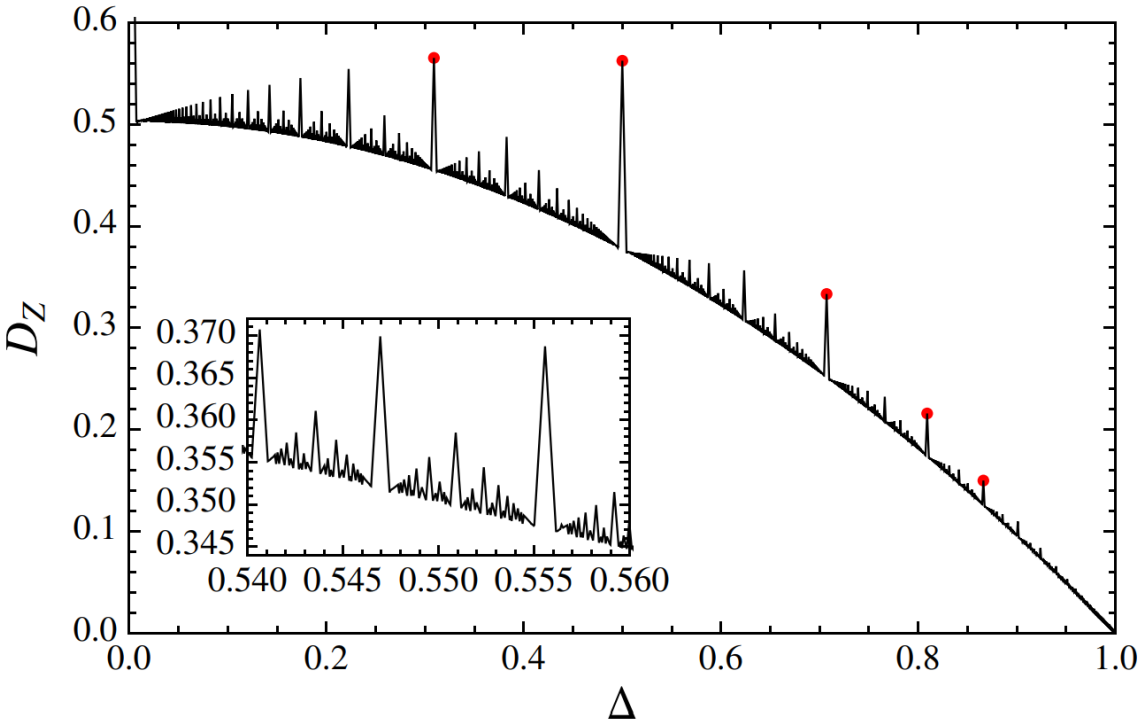

Figure 2.5. Plot of drude weight showing its fractal nature. Plot reproduced from [108].

define $C_\lambda(t) \equiv \sum_x C_{jj}(x,t;\lambda)$. We will take the $\beta \to 0$ limit; in this limit, all response functions including $\sigma(\omega)$ vanish, but the autocorrelation function (2.35) is well-behaved, and therefore so is the quantity $\sigma(\omega)/\beta$ (2.34): in the following, we will absorb this factor of $1/\beta$ in the definition of $\sigma(\omega)$. The Drude weight is defined as $\mathcal{D}_\lambda \equiv \lim_{t\to\infty} C_\lambda(t)$, and the d.c. conductivity is defined as $\sigma_\lambda^{\text{d.c.}} \equiv \lim_{\omega\to 0} \sigma_\lambda^{\text{reg}}(\omega)$.

2.3.1 Constraints on auto-correlation and a.c conductivity

The autocorrelator $C_\lambda(t)$, at any finite t, must be a continuous function of Δ and thus of λ: by the Lieb-Robinson theorem [148], one can truncate the infinite system on these timescales to a finite system of size $\propto t$, and all properties of finite systems evolve continuously with Δ. For some small ε, Eq. (2.33) implies that one can find nearby values $\lambda, \lambda+\varepsilon$ such that $\mathcal{D}_\lambda$ and $\mathcal{D}_{\lambda+\varepsilon}$ differ by a large amount. Even so,

locality implies that $|C_\lambda(t) - C_{\lambda+\varepsilon}(t)|$ remains small until some late time t^*. One can easily show that $t^* \gtrsim 1/\varepsilon$ which is basically the time scale at which 1st order perturbation theory breaks down. [3] Equivalently, in the frequency domain,

$$\int_0^\Omega d\omega |\sigma_\lambda(\omega) - \sigma_{\lambda+\epsilon}(\omega)| \lesssim C\frac{\varepsilon}{\Omega}, \tag{2.36}$$

where $\sigma_\lambda(\omega)$ is the *full* conductivity (2.34) at anisotropy λ, $\Omega > \varepsilon$ is generic, and C is a constant of order unity. Changing λ by ε can only shift spectral weight over frequencies $\sim \varepsilon$. Thus there is a characteristic frequency $\omega^*(\varepsilon) \lesssim \varepsilon$ such that for $\omega \gtrsim \omega^*(\varepsilon)$ the conductivity is essentially ε-independent. The drastic rearrangement of spectral weight that gives rise to the fractal structure of $\mathcal{D}_\lambda$ (2.33) must happen below this frequency.

We now discuss how this constraint relates the a.c. conductivity of an irrational λ to the d.c. conductivity of rational approximants. We approximate the irrational value, denoted λ_∞, by a sequence of rationals $\{\lambda_q = p/q\}$ with increasing denominators q. We assume that $C_\lambda(t)$ decays monotonically at sufficiently late times for all λ; within GHD this assumption certainly holds. By the reasoning above, until some late time t_q^*, $C_{\lambda_\infty}(t) \approx C_{\lambda_q}(t) > \mathcal{D}_{\lambda_q}$. Assuming monotonicity, therefore, $C_{\lambda_\infty}(t) - \mathcal{D}_{\lambda_\infty} > \delta\mathcal{D}_q \sim 1/q^2$, for all such large q, with $\delta\mathcal{D}_q \equiv \mathcal{D}_{\lambda_q} - \mathcal{D}_{\lambda_\infty}$.

We make the general ansatz $C_{\lambda_\infty}(t) - \mathcal{D}_{\lambda_\infty} \sim 1/t^{1-\alpha}$ [i.e., $\sigma_{\lambda_\infty}(\omega) \sim \omega^{-\alpha}$]. This ansatz fixes the crossover timescale t_q^* for large q, as follows. For $t \lesssim t_q^*$, $C_{\lambda_q}(t) \approx C_{\lambda_\infty}(t)$, whereas for $t \gtrsim t_q^*$, $C_{\lambda_q}(t) \approx \mathcal{D}_{\lambda_q}$. Equating the two forms at $t \sim t_q^*$ we find that $(t_q^*)^{1-\alpha} \sim \delta\mathcal{D}_q^{-1} \sim q^2$, so

$$t_q^* \sim q^{2/(1-\alpha)}. \tag{2.37}$$

---

[3] Note that this time scale is a lower bound. We can have longer time scale, like in the case considered here for which the actual cut-off time, as we argue below, is $t^* \gtrsim 1/\varepsilon^2$.

Finally, we relate this to the d.c. conductivity $\sigma^{\rm d.c.}_{\lambda_q}$ at λ_q. This is the integral of $C_{\lambda_q}(t) - \mathcal{D}_{\lambda_q}$, which follows the power-law $1/t^{1-\alpha}$ and is cut off at time t^*_q. Combining this result with Eq. (2.37) we find that

$$\sigma^{\rm d.c.}_{\lambda_q} \sim q^{2\alpha/(1-\alpha)}, \quad \sigma_{\lambda_\infty}(\omega) \sim \omega^{-\alpha}, \tag{2.38}$$

where $\alpha \geq 0$. Indeed this reasoning can be used to show that $\sigma(\omega)$ diverges, even without invoking GHD. By Dirichlet's approximation theorem, $|\lambda_q - \lambda_\infty| \lesssim 1/q^2$. Therefore, $t^*_q \gtrsim q^2$, so $C_{\lambda_\infty}(t) - \mathcal{D}_{\lambda_\infty} \gtrsim 1/t$. Fourier transforming gives $\sigma(\omega) \gtrsim |\log \omega|$ at low frequencies, establishing a divergence. (This divergence had previously been predicted using GHD [149].)

2.3.2 d.c conductivity using GHD

The argument above shows that $\sigma(\omega)$ must diverge at low frequencies for irrational λ. However, Eq. (2.38) does not determine the exponent α. To do this we adopt the framework of generalized hydrodynamics (GHD) [98, 99], which was recently extended to incorporate diffusion [150, 151, 152].

For the d.c. conductivity $\sigma^{\rm d.c.}_{\lambda_q}$, we have the relation [150, 151]

$$\begin{aligned}\sigma^{\rm d.c.}_{\lambda_q} &= \frac{1}{4}\sum_{kl}\int d\theta_1 d\theta_2 \rho_k(\theta_1)\rho_l(\theta_2) f_k f_l |v_k(\theta_1) - v_l(\theta_2)| \\ &\quad \times \left[\mathcal{K}^{\rm dr}_{kl}(\theta_1-\theta_2)\left(\frac{m^{\rm dr}_k}{\rho^{\rm tot}_k(\theta_1)\sigma_k} - \frac{m^{\rm dr}_l}{\rho^{\rm tot}_l(\theta_2)\sigma_l}\right)\right]^2,\end{aligned} \tag{2.39}$$

in terms of data from the Thermodynamic Bethe Ansatz (TBA) [139].

In this expression, k, l label quasiparticle species and θ_i label rapidities; and the other symbols denote properties (within TBA) of quasiparticles with labels k, θ: $\rho_k(\theta)$ is the density of quasiparticles; $f_k = 1 - \rho_k(\theta)/\rho^{\rm tot}_k(\theta)$ is related to their filling factor (independent from θ at infinite temperature); $\rho^{\rm tot}_k(\theta)$ is the total density of states;

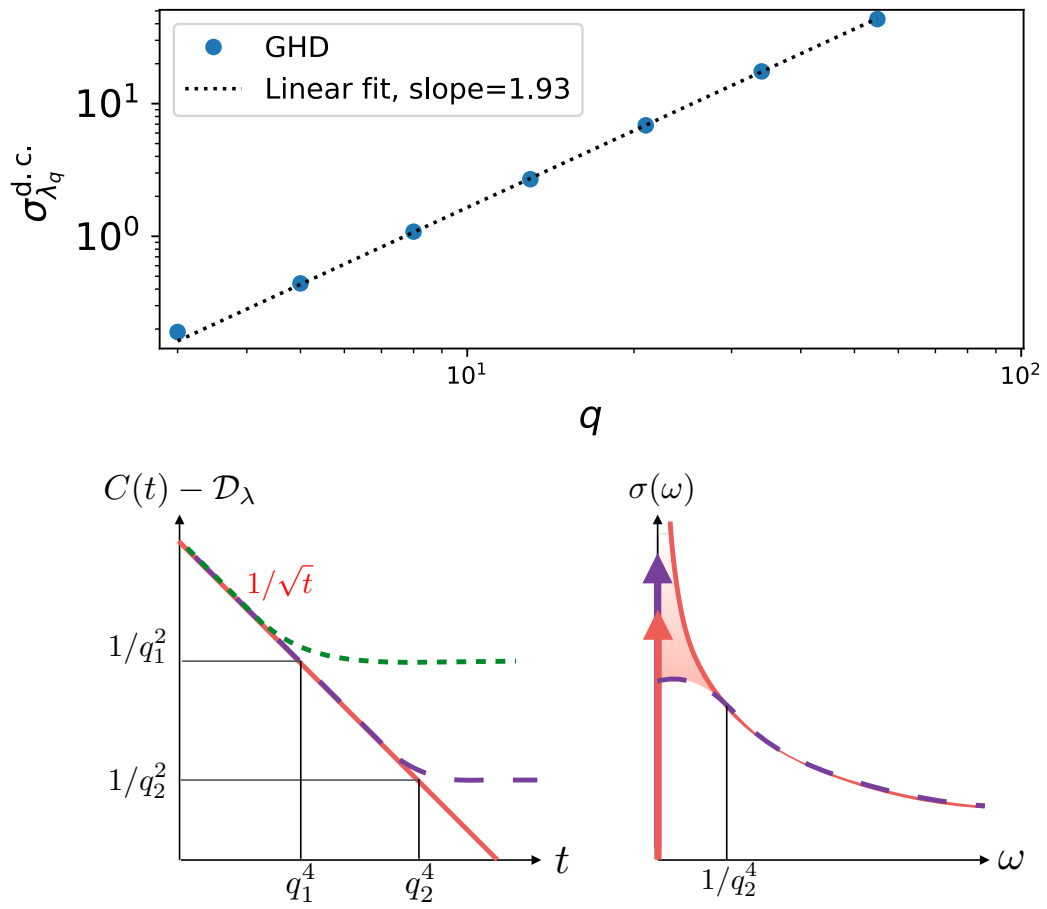

Figure 2.6. d.c conductivity and auto-correlation. Upper panel: d.c. conductivity for rational Fibonacci approximants $\lambda_q = F_{n-1}/F_{n+1}$ *vs* $q = F_{n+1}$ to the generic irrational anisotropy $\lambda_\infty \equiv 1/\varphi^2$ where φ is the Golden Ratio. We find $\sigma^{\mathrm{d.c.}}_{\lambda_q} \sim q^\beta$ with $\beta \approx 1.93$, corresponding to $\alpha \simeq 0.49$ in eq. (2.38). Lower panel: relationship between the d.c. conductivity for approximants, the crossover timescale, and the a.c. conductivity for λ_∞. Left: the autocorrelation function $C(t)$ for λ_∞ must follow that of a rational approximant with a given denominator q_i until a crossover timescale $t^*_{q_i} \sim q_i^4$ (derived in the text). This forces $C(t) \sim 1/\sqrt{t}$ for λ_∞. Right: in the frequency domain, the "excess Drude weight" at the rational approximant must precisely match the missing spectral weight in $\sigma(\omega)$ for $\omega < \omega^*_q \sim q^{-4}$.

$v_k(\theta)$ and m_k^{dr} are respectively the dressed velocity—derived from the dressed dispersion relation—and dressed magnetization; and $\sigma_k = \pm 1$ is the so-called *σ-parity* of quasiparticle species k. The dressed kernel $\mathcal{K}^{\mathrm{dr}}$ is the solution to an integral equation

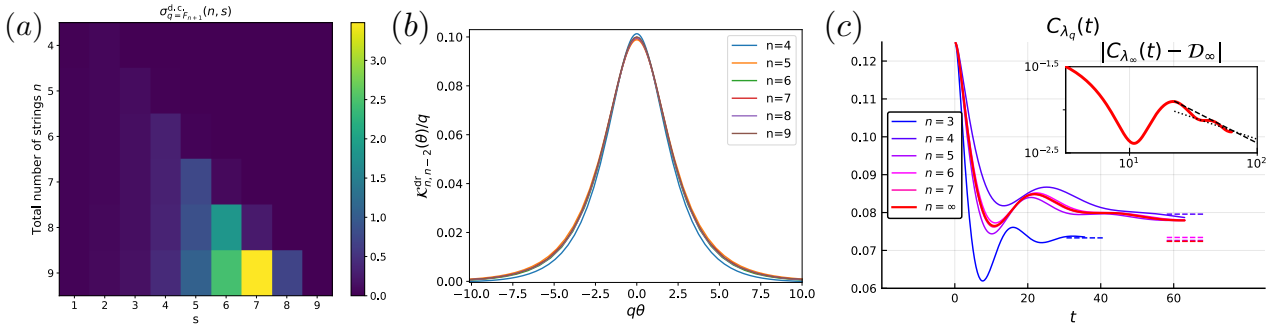

Figure 2.7. (a) Contributions to the d.c. conductivity of the charged quasiparticle from scattering off each species of neutral quasiparticle. For any given n, the dominant source of diffusion is the heaviest neutral quasiparticle $n-2$. (b) Rapidity-dependence of the dressed kernel for scattering between the charged quasiparticle and the largest neutral quasiparticle; we find that $K^{\mathrm{dr}}_{n,n-2}(\theta)$ has a peak of height q_n and width $1/q_n$, as shown by the data collapse. (c) TEBD numerics for the current-current correlator for various n; plots for the larger n stay close to the $n = \infty$ value at the accessible times. Inset: Power-law decay of $C_{\lambda_\infty}(t) - \mathcal{D}_{\lambda_\infty}$: although our time range is limited, our data is consistent with an exponent $1 - \alpha \in (\frac{1}{2}, \frac{3}{4})$ (dashed lines).

that has to be solved numerically. For a brief overview of the TBA formalism we refer to Ref. [139] and supplemental material of [153].

As a generic irrational number, we choose $\lambda_\infty = 1/\varphi^2$ where φ is the Golden Ratio. The TBA for this number has the advantage of being tractable, with a simple quasiparticle hierarchy. The continued fraction expansion is given by $\varphi^2 = 1/(2 + 1/(1 + 1/(\ldots)))$. Truncating this expansion by replacing the last term with 2 gives the series $\lambda_n = F_{n-1}/F_{n+1}$, where F_n is the nth Fibonacci number. The Bethe ansatz solution for λ_n involves n quasiparticle species [139]. At zero field, the first $n - 2$ quasiparticle species carry no dressed magnetization; the last two quasiparticle species each carry a magnetization $\sim F_{n+1} = q$ and are responsible for the spin Drude weight. We refer to quasiparticles with larger values of n as being "larger," which is true at lattice scale; however, GHD treats all quasiparticles as pointlike. Spin transport is dominated by charged quasiparticles; the other, "neutral" quasiparticles affect spin

transport by scattering elastically off the charged quasiparticles and causing them to diffuse.

GHD yields the following conclusions for spin transport. Charged quasiparticles move with a characteristic velocity which saturates to an $\mathcal{O}(1)$ value as $q \to \infty$, and as they move they scatter off neutral quasiparticles. Large neutral quasiparticles are rare $\rho_{n-2} \sim q^{-2}$, but also have an outsized influence, because their scattering phase shifts are large. Fig. 2.7 separates out the contributions to $\sigma^{\text{d.c.}}_{\lambda_q}$ by quasiparticle index/size: evidently the dominant contribution comes from scattering off the largest neutral quasiparticle. Explicitly evaluating Eq. (2.39) with the appropriate TBA data we find that $\sigma_{\text{d.c.}}(\lambda_q) \sim q^2$. This asymptotics can be derived analytically [153], and is consistent with numerical evaluation of Eq. (2.39) (Fig. 2.6). Using Eq. (2.38) this means that

$$\sigma_{\lambda_\infty}(\omega) \sim 1/\sqrt{\omega}, \tag{2.40}$$

and therefore that $t^*_q \sim q^4$.

2.3.3 Soliton gas picture

This long crossover timescale has a physical interpretation in terms of the semi-classical soliton gas framework for GHD [127, 152]. The dressed kernel $\mathcal{K}^{\text{dr}}(\theta)$ is peaked at $\theta = 0$, with a peak height that scales as q and a peak width that scales as $1/q$ (Fig. 2.7.b). The dominant scattering events that a charged particle experiences are those with large neutral quasiparticles which have almost the same rapidity and therefore almost the same velocity (up to $\sim 1/q$). At large q the heaviest neutral quasiparticle has density $1/q^2$; fixing its rapidity to a window of size $1/q$ reduces the density of dominant scatterers to $1/q^3$. Since the two quasiparticles start out spaced at a distance q^3 and have a relative velocity $\sim 1/q$, they collide on a timescale $t^*_q \sim q^4$.

At much shorter timescales, the system is not in local equilibrium and the asymptotic result (2.39) does not apply.

One can derive further physical insight by applying the soliton-gas framework to the motion of the charged quasiparticle at very large q but for $t \ll t_q^*$. In this regime, as time passes, the charged quasiparticle encounters increasingly large neutral quasiparticles, and therefore picks up increasingly large displacements. On timescale t, the largest collision will involve a quasiparticle for which $q(t) \sim t^{1/4}$. This quasiparticle gives a (dressed) displacement [127, 126, 154] of order $\Delta x^{\rm dr} = \mathcal{K}^{\rm dr}/p'(\theta) \sim q^3 \sim t^{3/4}$ where we have used the fact that the dressed momentum scales as $p'(\theta) \sim \rho^{\rm tot}(\theta) \sim q^{-2}$. Therefore, the variance of the position of the charged quasiparticle scales as $t^{3/2}$, consistent with our exponent for the conductivity. Since the charged quasiparticle spreads through kicks of power-law increasing strength, whose probability also falls off as a power law, it is a Lévy flight with dynamical exponent $z = 4/3$ [155]. It would be interesting to compare the spin structure factor to known scaling forms for Lévy flights.

CHAPTER 3

CRITICALITY AND UNIVERSALITY IN QUASI-PERIODIC QUANTUM SYSTEMS

Unlike random systems, the effects of QP modulations on critical quantum systems has not received as much attention. This is partially due to the ubiquitous nature of random disorder in the form of impurities in solid state materials. Standard theoretical techniques, like those based on the replica trick, developed for the study of random systems fails to work for QP systems due to its deterministic long-range correlated nature. However, recent advancements in the fields of twisted bi-layer graphene [1, 2, 3], cold atoms [4, 5, 6, 7, 8, 9, 10, 11, 12, 13, 14, 15, 16], and photonic lattices [17, 18, 19, 20] have made it easier to probe QP quantum systems.

Quantum critical systems under the influence of random perturbations flow to random fixed points which are broadly classified in two categories, 1) those with finite randomness, and 2) those having infinite randomness [1] [157, 158]. Of these, the latter are more tractable and for which asymptotically exact methods based on the real space renormalization group (RSRG) exist [57, 58, 59, 60]. Many quantum critical systems are known to flow to infinite-randomness fixed point under RSRG and it is only natural to ask for an equivalent question of "infinite-quasiperiodicity" fixed points for the corresponding QP modulated systems, and whether they can also be described using RSRG.

The RSRG has previously been used to study QP quantum systems but they were restricted to cases where the values were discrete and taken from aperiodic sequences

[1] That is, whether the standard deviation of the fixed point distribution is finite or infinite.

[67, 66, 65, 64, 68, 69, 70, 62, 63, 72, 73, 71]. It is not immediately obvious that conclusions obtained from such toy models correctly apply to realistic systems under continuous QP modulations, for example, due to bi-chromatic lasers with incommensurate frequencies. These studies were also restricted to 1d with few works available for 2d systems [159]. Exact analytical treatment for QP quantum systems are available but restricted to non-interacting systems like the XY chain, or the transverse field Ising model (TFIM); see [63, 62] for couplings taken from discrete aperiodic sequences and for the case of generic continuous modulation see [74, 75, 76].

In this chapter [2] we use the RSRG to study critical properties of quantum systems in the presense of *continuous* QP modulation. The central idea of the RSRG used is to identify the term in the Hamiltonian with the largest energy scale and consequently restrict the associated local degrees of freedom to their ground state. Perturbation theory is then used to find the new effective Hamiltonian in the restricted subspace of the projected ground state. This process is repeated untill we are left with one or two terms in the renormalized Hamiltonian. The idea of systematically projecting the Hilbert space to the ground state was first proposed in [57], where it was used to study low temperature properties of the random XXX chain. Each step of the RG induces some error due to the use of 2nd order perturbation theory and it is not clear that ignoring these error will not effect the true physics. However, it is one of the main result of this chapter that, as for random systems, for QP systems too the errors get progressively smaller with the RG flow and goes to zero in the asymptotic limit. The RSRG is said to be controlled in this sense and the results obtained are expected to correctly describe the universal physics near the fixed point.

The chapter is organized as follows: we start with 1d systems and consider the Heisenberg model, where we show that the couplings flow to a self-similar Fibonacci

[2] This chapter is based on [84, 156].

sequence under RG [3]. This allows for extracting the critical properties analytically. We then move on to 1d quantum Potts model. Here the fixed point is a "superposition" of various self-similar sequence, that is, the details of the fixed point sequence depend on the phase difference between couplings and magnetic fields. But we show that various critical properties do not depend on details of the sequences and can be calculated assuming the fixed point to be the standard Fibonacci sequence. We also point out the irrelevance of weak QP for the Ising model which was recently verified in [75, 76, 74]. Thus, the discrete aperiodic sequences studied until now can be seen as effective description of the actual fixed points for generic continuous QP modulations. We then move on to 2d systems. The RSRG is not analytically tractable in 2d due to topology of the system's graph changing with the RG flow. However, we implement RSRG numerically and discuss various numerical results and argue for their validity. We provide a heuristic argument for the correlation exponent, ν, similar to the argument used in 1d systems and thus hinting at the "super-universality" of ν, irrespective of the model, frequency of the QP modulation γ, and dimension d.

3.1 Heisenberg Chain in 1d

Although our results are very general and apply to a variety of one-dimensional systems, for concreteness we will illustrate the approach on a paradigmatic example of quantum magnetism: the antiferromagnetic spin-$\frac{1}{2}$ Heisenberg spin chain

$$H = \sum_i J_i \boldsymbol{S}_i \cdot \boldsymbol{S}_{i+1}, \tag{3.1}$$

with $J_i > 0$. In the clean case $J_i = J$, this spin chain is gapless and is described at low energy by a $SU(2)$ symmetric Luttinger liquid with Luttinger parameter $g = \frac{1}{2}$.

[3] For concreteness and simplicity, in this proposal we always take the fequency to be φ.

Disorder in the J_i couplings is a relevant perturbation [160] that leads to a quantum critical random-singlet state [60].

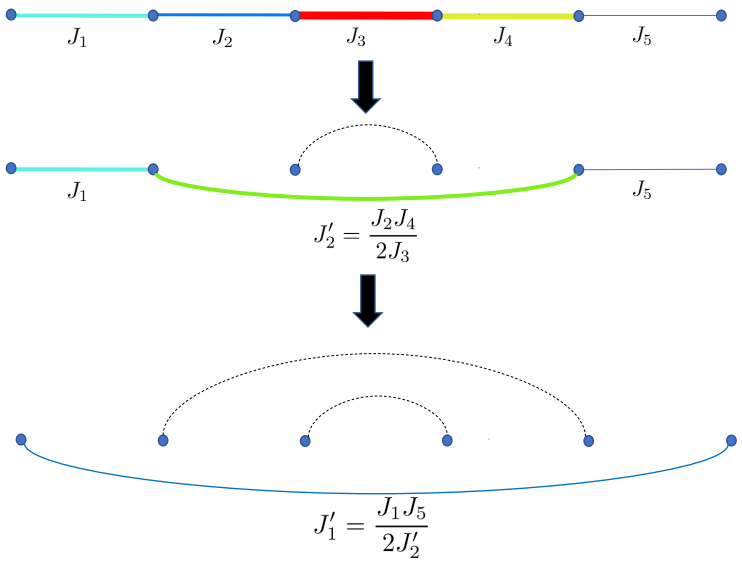

Figure 3.1. RSRG rules for the anti-ferromagnetic Heisenberg chain in 1d. Colored solid line indicates coupling. Dashed lines indicate that the pair has been projected to the singlet state.

In the random case, the low-energy physics can be captured by a strong disorder real space RG with the following iterative procedure [57]: one identifies the strongest remaining coupling J_i, forms a singlet out of the spins $i, i+1$ and generates a new effective coupling $J_{\text{eff}} = \frac{J_{i-1}J_{i+1}}{2J_i}$—at second order in perturbation theory—between spins $i-1$ and $i+2$; see Figure 3.1. This procedure is accurate so long as $J_i \gg J_{i-1}, J_{i+1}$; in the random case, the ratio of neighboring couplings flows to infinity, so the procedure is asymptotically exact [60].

Here, we are interested instead in quasiperiodic modulations of the couplings, with $J_i = f(i)$ with $f(x) = f(x + \varphi^{-1})$ for irrational φ [in the bulk of this thesis we take $\varphi = \frac{1+\sqrt{5}}{2}$]. We take $f > 0$ to be a general smooth function with a smooth logarithm. To understand whether this perturbation is relevant at the Heisenberg critical point we recall that the Heisenberg chain is a critical point separating two inequivalent

dimerized phases, which occur when the even and odd bonds have different strengths. The correlation length exponent for the dimerization transition is $\nu = 2/3 < 1$; thus, weak quasiperiodicity is relevant [161, 162, 65] by the Harris-Luck criterion [163] and the system flows to a quasiperiodicity-dominated fixed point.

It proves convenient to write the RG rules in logarithmic variables, $\ell_i \equiv -\log J_i$, as

$$\ell_i' = \ell_{i-1} - \ell_i + \ell_{i+1} + c, \tag{3.2}$$

where $c = \ln 2$. We will be interested in other values of c when we discuss the Potts model and treat it as a parameter. For simplicity, we define the potential to be,

$$\ell_j = -\ln J_j = a + \cos\left(2\pi\varphi j + \theta\right), \tag{3.3}$$

where a is some constant, and θ is a phase which we average over. Note that the final results *do not* depend on the precise definition of the initial distribution as long as it is sufficiently well-behaved with not much oscillations [84]. We check numerically that we get same results for potentials defined differently. Defining the potential in terms of ℓ_i simply the calculations. As an example, we find the wandering constant w as follows: defining the detuning parameter, denoting the asymmetry between even and odd coupling, as $\delta_{2i} = \ell_{2i} - \ell_{2i+1}$, we can show that $\sum_{i=0}^{N/2} \delta_{2i} = C_1 \sin\left(\pi\varphi(N + 5/4) + \theta/2\right) + C_2$, where $C_{1,2}$ are constants depending only on φ and θ. We immediately see that if N is a rational approximant of φ (e.g Fibonacci numbers for the golden ratio), then $\langle\delta\rangle \sim \text{const.} + \mathcal{O}(1/N)$, implying zero wandering; there will be some oscillations in the average for other N, see [75, 76]. Note that this result is true for all reasonable irrational φ.

3.1.1 Flow to discrete sequence

Note that in the RG procedure we can decimate local minimum ℓ_j (recall that minimum ℓ_j is maximum J_j) in any order we want. It is therefore helpful to introduce

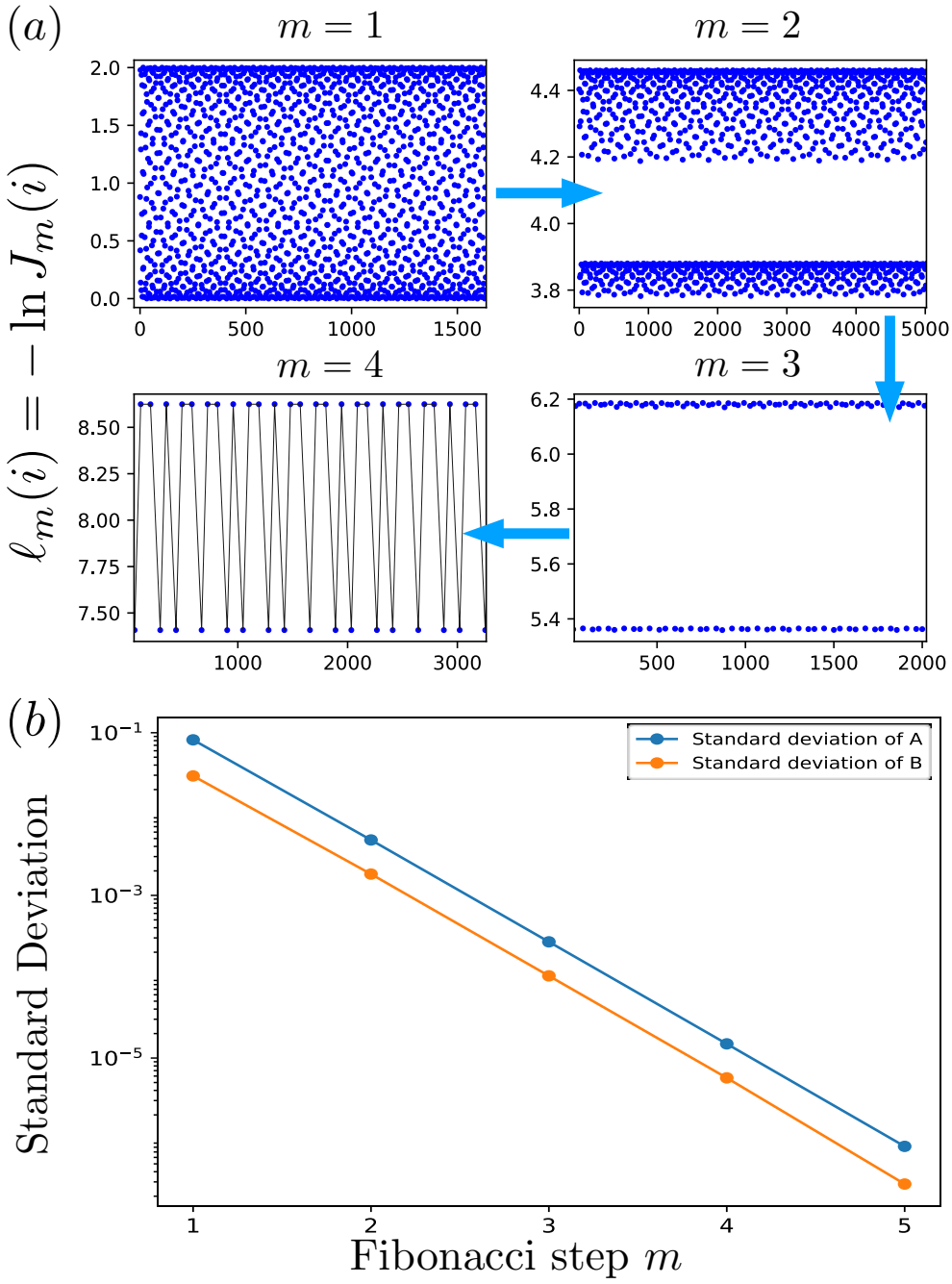

Figure 3.2. Quasiperiodic Heisenberg chain. (a) Evolution of the couplings under renormalization for an Heisenberg chain with initial potential (3.3) with $a = 1$. The fluctuations decay with the number of RG steps, and become completely negligible after a few Fibonacci steps. (b) The fluctuations about the sequence prediction (3.4) starting from a cosine potential decay exponentially with the number of Fibonacci RG steps m.

the notion of a *local minimum*: i.e., a site j such that $\ell_j < \min(\ell_{j-1}, \ell_{j+1})$. Any such coupling will get decimated before its neighbors, so we can decimate them all at once. It is crucial to note that, if we label minima as B and all other sites as A, we will arrive at a two-letter Fibonacci sequence defined by the inflation rule $A \to AB, B \to A$ (this can be checked by inspection, see [84] for a formal proof). This implies that the first couplings to be decimated already follow a Fibonacci sequence. With this crucial observation in mind, we denote the set of minima as B_0 and the set of all other couplings as A_0. We now decimate all the B_0 couplings — we call this a Fibonacci RG step. This gives rise to a new Fibonacci sequence: once again, we can identify the local minima, denote them B_1, decimate them, and so on. This allows us to keep track of the renormalized couplings analytically. Remarkably, after a few steps, we find that all the $A(i)$ and $B(i)$ at a given step become increasingly similar in magnitude [84], Figure. 3.2. Specifically, after m Fibonacci RG steps, we find the effective couplings

$$\begin{aligned} A_m(i) &= a + m(m+1)c + \frac{\cos(F_{3m+2}\pi\varphi)}{\cos\pi\varphi} + \epsilon^A_{i,m}, \\ B_m(i) &= a + m^2 c - \frac{\cos(F_{3m+1}\pi\varphi)}{\cos\pi\varphi} + \epsilon^B_{i,m}, \end{aligned} \tag{3.4}$$

where F_n is the n$^{\text{th}}$ Fibonacci number, and $\epsilon^{A,B}_{i,m}$ are site-dependent fluctuations that go to 0 exponentially as $m \to \infty$; see Figure. 3.2. With each Fibonacci step the fluctuations get smaller, and we obtain a sharper sequence which asymptotically becomes a perfect binary Fibonacci sequence.

From eq. (3.4) we also see that $A_m - B_m$ goes as mc, which means that the perturbation theory, and hence the RG, is getting better with m, becoming exact in the limit $m \to \infty$. Inspired from the random case, we call a fixed point with this property an "infinite quasi-periodic" fixed point. Also note that if $c = 1$, which corresponds to the prefactor to be equal to 1 in the RG rules, then RG becomes

worse with the flow. The transverse field Ising model falls in this category and have interesting consequences that we will explore in Section 3.3.

3.1.2 Quantum Critical properties

The critical properties of the quasiperiodic chain (3.1) then follow straightforwardly from eq. (3.4), in agreement with previous works on discrete aperiodic sequences. The new fixed point has dynamical exponent $z = \infty$: a chain of length $L \sim \varphi^{3m}$ is fully decimated in m Fibonacci steps, so the energy gap ΔE of the chain is set by the last coupling to be decimated, $\log \Delta E = -\log B_m \sim -m^2 c$, so that [64, 73]

$$\Delta E \sim e^{-\frac{c}{(3\ln\varphi)^2}\ln^2 L}, \tag{3.5}$$

where we have used eq. (3.4). Other critical properties readily follow from the Fibonacci nature of the fixed point, which has already been considered in many of the previous studies on aperiodic sequences.

The Correlation length exponent can be calculated in two ways. 1) We can perturb the Fibonacci sequence (which let us assume to be perfectly binary) by introducing an asymmetry between odd and even couplings: $A_0^E = A_0 + \delta/2,\ B_0^E = B_0 + \delta/2,\ A_0^O = A_0 - \delta/2,\ B_0^O = B_0 - \delta/2$, where the superscript O, E corresponds to odd, even couplings respectively. After m Fibonacci steps, the system size would scale by F_{3m} and the new couplings will on average contain F_{3m} number of original couplings, of which half will be odd couplings, and half even. Thus the new couplings would be shifted by $\sim \pm F_{3m}\delta$ for even, and odd couplings respectively. The correlation length is set by the length scale F_{3m_δ} when the asymmetry, $F_{3m_\delta}\delta$, becomes of the order $A_{m_\delta} - B_{m_\delta}$ (since only odd couplings would get decimated after this). From eq. (3.4), we get $\xi\delta \sim m_\delta \sim \log \xi$, or $\xi \sim \delta^{-\nu}$, where,

$$\nu = 1 + \text{log. corrections.} \tag{3.6}$$

These log corrections to ν were also observed in $1d$ transverse field Ising model in [75, 76]. [4]

2) We can perturb the original potential to $\ell_j = W(a + \cos(2\pi\varphi j + \theta)))$, with $W \equiv W^E = 1$ for even couplings, and $W \equiv W^O$ for odd couplings treated as the detuning parameter. This would have the effect of changing the order of decimation in places where the difference of neighboring couplings, $\ell_j - \ell_{j+1}$, are of order $\delta W \equiv |W^O - W^E|$. From the discussion in the Introduction, we know that a QP potential is almost periodic with periods given by the denominator of the frequency's rational approximant. For our case of golden ratio, these are given by Fibonacci numbers, F_a. Noting the fact that $\varphi F_a - F_{a+1} \sim \varphi^{-a}$, the location with the change in the order of decimation repeat on the length scale of $F_n \sim \varphi^n$, with $\varphi^{-n} \sim \delta W$. This length scale sets the correlation length $\xi \sim \varphi^n \sim 1/\delta W$, giving $\nu = 1$. We call locations where the order of decimation changes, as defects; due to almost periodic nature of QP functions, these defects repeat on a length scale determined by the error caused by the detuning.

The 2nd method used above for calculating ν is less dependent on the fixed point details and puts more emphasis on the universal properties of QP function by finding a equivalence between the correlation length and approximate periods obtained from the continuous fraction expansion. Thus, we expect this method to carry forward to different systems where we cannot explicitly study the fixed point (for example, in the Potts model discussed in subsequent sections) and other irrationals having self-similarity (periodicity) in their continuous fraction expansion [164]. Also, experimen-

[4] This method is quite general and can also be used, for example, to get ν for the random transverse field Ising model [58, 59] as follows: after the size of the system is scaled by the factor L_b, asymmetry δ between field and coupling would increase by $L_b\delta$ (this is a general property of the RG rules in $1d$ and is independent of the details of the critical point). When the asymmetry becomes of the order of the standard deviation of the field distribution, the subsequent decimations will mostly be fields. From the solution of the critical point, the standard deviation scales as $\sqrt{L_b}$, giving $\xi\delta \sim \sqrt{\xi}$ for the correlation length, or $\xi \sim \delta^{-\nu}$ with $\nu = 2$.

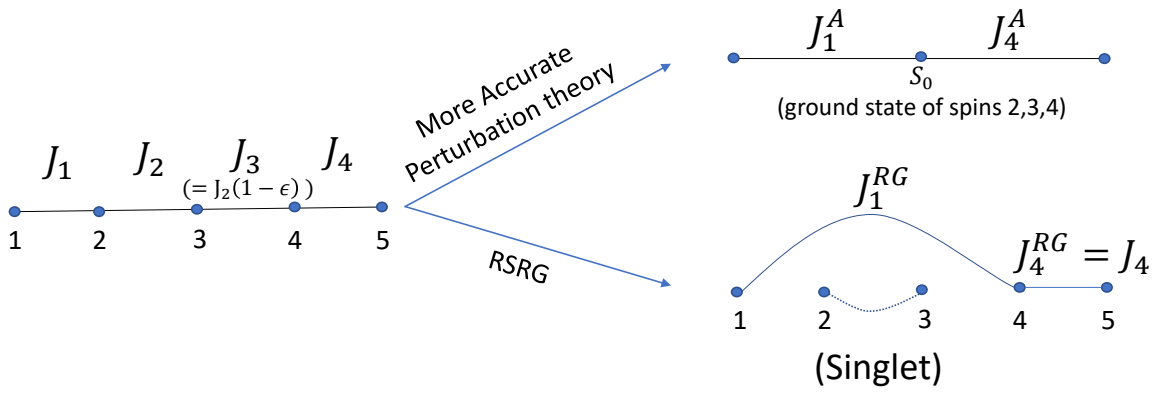

Figure 3.3. We can do a more accurate perturbation procedure in case two neigbhor couplings have similar strength. Comparing values from the RSRG to values from this accurate procedure shows that not much is changed qualitatively for strongh enough modulations.

tally it is more relevant to disturb the initial potential, while it may not be possible to control the asymmetry near the actual fixed point. In fact, by artificially inserting singularities in initial potential we can change the value of ν. For example, consider $\ell_n = f(\cos(2\pi\varphi n+\theta))$ with $f(x) = 2+\text{sgn}\left(\cos(2\pi\frac{\{\varphi\}}{2}) - \text{x}\right)\sqrt{|\cos(2\pi\frac{\{\varphi\}}{2}) - \text{x}|}$ being singular at $x = \cos(2\pi\{\varphi\}/2)$ ($\{\cdot\}$ denotes fractional part). $f(x)$ is a nice continuous bounded (but singular) function and hence flows to discrete Fibonacci sequence under RG. From the first method, wherein we perturb the fixed point sequence, we get $\nu = 1$. However, performing the analysis of the 2nd method, we find $\nu = 2$. These predictions are found to be correct via numerical methods [84].

Bad decimations: There might be a concern raised over the presence of defects, which are exactly the locations where our RG rules are expected to give large errors. This also cast doubts over the validity of the calculation for $\nu = 1$ based on defects. However, we can show that the RG rules are qualitatively correct near the defects. Consider a subsystem of 5 spins as shown in Figure 3.3, with $J_3 = J_2(1-\epsilon)$, where ϵ is a small positive number, and J_1, J_4 are small enough. Naively using RSRG we would decimate J_2 to get $J_1^{RG} = \frac{J_1 J_3}{2J_2} = J_1(1-\epsilon)/2$, while J_4 remain unchanged. We

can also do a more accurate perturbation theory by projecting spins 2,3,4 to their ground state (which is a doublet of spin 1/2) described by an effective spin S_0. Using 1st order perturbation theory (see Appendix B of [72]) we get (to leading order in ϵ) $J_1^A = J_1(2/3-\epsilon/2)$, and $J_4^A = J_4(2/3+\epsilon/2)$. Our naive RG values can be written as, $J_1^{RG} = \frac{3}{4}J_1^A(1-\epsilon/4)$, $J_4^{RG} = \frac{3}{2}J_4^A(1-3\epsilon/4)$, which clearly show quantitative deviation from values obtained through more accurate procedure. But for sufficiently strong QP modulations, this differences does not change the subsequent order of decimations in the RG and give correct qualitative answers.

3.2 1d Quantum Potts model

To illustrate the generality of our approach we now turn to the q-state quantum Potts model, governed by the Hamiltonian

$$H = -\sum\nolimits_i J_i \delta_{n_i,n_{i+1}} - \sum_i \frac{h_i}{q} \sum_{n_i,n_i'} |n_i\rangle\langle n_i'|, \tag{3.7}$$

where n_i is a variable on site i that takes one of q possible values. The first term wants to align the system to a ferromagnet ordered phase, while the 2nd term, like the transverse field in the Ising model, causes disorder by flipping a spin to all possible colors.

To treat this model in the RG scheme, one formally rewrites it as a chain with twice the number of links, and assigns the variables J_i to even links and h_i to odd links. The decimation step [165] then takes the same form as Eq. (3.2) with $c = \log(q/2)$. More precisely, decimating a strong field h_i leads to a new effective bond $J_{\rm eff} = 2J_{i-1}J_i/(qh_i)$ connecting neighboring spins, while decimating a strong bond J_i creates an effective spin acted on by am effective field $h_{\rm eff} = 2h_ih_{i+1}/(qJ_i)$. When $q > 2$, $c > 0$, so once again the RG flows to discrete sequences.

The main distinction between the Potts and Heisenberg models lies in the choice of initial couplings: in the Heisenberg model it was natural to draw all bonds from the same QP sequence, whereas here it is natural to take the h_i and J_i from distinct QP sequences with frequency φ but different phases: $J_i = W_J(a + \cos(2\pi\varphi(i + \frac{1}{2}) + \theta_J))$ and $h_i = W_h(a + \cos(2\pi\varphi i + \theta_h))$ with $a > 1$. This introduces a separate variable to the problem, viz. the relative phase $\theta \equiv \theta_J - \theta_h$ between the sequences for h_i and J_i. [5]

Numerically running the RG in this case leads to the following picture. When θ is close to the special values, we once again observe a flow to self-similar Fibonacci-like sequences. In that case, the results for the XXX spin chain carry over to Potts immediately – in particular, $\nu = 1$. Other critical exponents can readily be computed analytically; for example, we find that correlation function of the order parameter $\sigma_i^{(a)} = \delta_{n_i,a} - q^{-1}$ with a a given Potts color, scales as (see [84])

$$\langle \sigma_0^{(a)} \sigma_r^{(a)} \rangle \sim r^{-2\Delta_\sigma}, \text{with } \Delta_\sigma = \frac{\ln(1 + 2\varphi^{-1}/3)}{3 \ln \varphi}. \tag{3.8}$$

The proof of above relation is quite general and not specific to Fibonacci sequences.

However, for large θ we see abrupt transitions to *different* sequences. Thus, there appear to be *multiple* fixed-point sequences, with transitions between them occurring at special values of θ. These fixed points have different length-energy scaling: in all cases, $\Delta E \sim e^{-a \ln^2 L}$, but a depends on θ. The dependence of the fixed point on the phase difference in the context of 1d Ising model was also observed in [75, 76].

[5] For the final data for the Potts model, we average over both phases. The justification for averaging over phases is that in infinite system different sub-systems have different phases. Thus more accurately, in the case of the Potts model we should have averaged over the phases keeping the phase difference constant; different phase difference corresponds to different physical systems. However, we find critical properties to be universal for generic values of the phase difference; also see [76, 75].

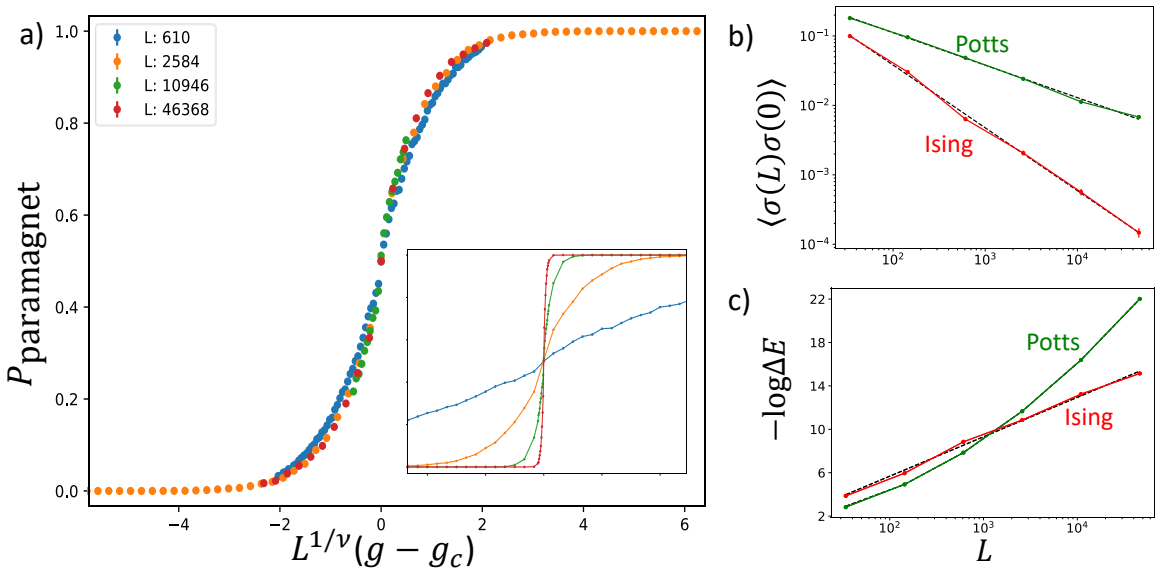

Figure 3.4. Quasiperiodic Potts ($q = 3$) and Ising ($q = 2$) chains. For the Ising chain, we choose a potential with both positive and negative couplings, while for the Potts chain, all couplings are taken to be antiferromagnetic. (a) Scaling collapse of the probability of the RG to end in a paramagnetic phase for the Potts model (paramganetic phase can be defined as the absence of edge parafermion modes [166]), with $\nu = 1$. Here $g = W_h/W_J$ is an asymmetry parameter between h_i and J_i with $W_{J,h}$ the amplitude of the quasiperiodic potentials, and $g_c = 1$. (Inset) Raw, uncollapsed data. (b) Spin-spin correlation function $\langle\sigma(L)\sigma(0)\rangle$ averaged over the uncorrelated phases θ_J, θ_h, scaling as $L^{-0.47}$ for Potts (in good agreement with (3.8) derived for discrete Fibonacci sequences), and $L^{-0.9}$ for Ising. Error bars represent standard error. (c) Energy-length scaling: $\Delta E \sim L^{-0.22 \ln L}$ for Potts, while the Ising transition has a finite dynamical exponent $z \approx 1.6$.

However, all of the fixed points agree on the exponent $\nu = 1$, as well as on the spin-spin correlation function eq. (3.8) (Fig. 3.4). [6]

3.3 Ising model

We briefly remark on the $q = 2$ Potts model, i.e., the Ising model. In this case, $c = 0$ in the decimation rule (3.2). Thus the RG does not take arbitrary functions to

[6] This suggest a different kind of universality, independent of the details at the fixed point. For example, we expect fixed points described by the rules $A \to ABABA$, $B \to ABA$ and $A_1 \to A_1BA_2BA_1$, $A_2 \to A_2BA_1BA_2$, $B \to A_1BA_2$ to have same critical properties.

sequences. Instead, nonsingular sequences of ℓ are generically squashed under the RG and become effectively constant after a few steps. Remarkably, this corresponds to the observation that weak quasiperiodic modulations are (marginally) irrelevant at the clean Ising critical point. It is indeed known from free fermion numerics [75, 76] that the Ising transition in the presence of any such nonsingular quasiperiodic potentials is governed by the *clean* Ising conformal field theory, in agreement with the predictions of the RG. To see a nontrivial transition in this case, one must take singular distributions of ℓ; one can do this, e.g., by taking $J_i = W_J(a+\cos(2\pi\varphi(i+\frac{1}{2}+\theta_J))$ and $h_i = W_h(a+\cos(2\pi\varphi i+\theta_h))$, with $0 < a < 1$ so $\ell_{2i} = -\ln|J_i|$, $\ell_{2i+1} = -\ln|h_i|$ is singular. For $a > 1$, quasiperiodic potentials flow to uniform ones under renormalization, indicating a transition in the clean Ising universality class. For $a < 1$ the critical dynamics is strongly modified because the chain has a finite density of nearly broken links, corresponding to a flow to a quasiperiodic fixed point. This quantitatively reproduces the phase diagram obtained in Refs. [75, 76]. For $a < 1$, the RG does not lead to perfect sequences, and does not flow to "infinite quasiperiodicity" as the examples described above. This means that the perturbation theory steps do not become asymptotically exact under the RG. This is a physical feature of the transition, as it is known from numerics that it has a finite dynamical exponent [75, 76]. (This is similar to the random case where the strong disorder RG is exact only for infinite-randomness critical points which have infinite dynamical exponents.)

Although our RG procedure is not fully controlled for this model, running the RG numerically yields a fixed point that is qualitatively similar to the numerically seen one [75, 76, 32] (Fig. 3.4): in particular, it has a correlation length exponent $\nu = 1$, and a finite dynamical critical exponent $z \approx 1.6$, which is close to the numerical value $z \approx 2$. The remaining discrepancies are to be expected given that the procedure is not controlled; however, the RG correctly captures the qualitative features of the

transition and is the only analytic method able to capture the universality class of this transition.

3.4 2d Quantum Potts model

So far we dealt with $1d$ systems which can solved analytically either by the virtue of the system being non-interacting or by RSRG methods discussed so far in this chapter. Non-interacting systems in $1d$ can be studied effectively via numerical diagonalization or various other analytical techniques developed over the years. RSRG in $1d$ can also be tracked analytically primarily because the topology of the system remains invariant under RG. However, QP systems in higher dimension remain poorly understood [4, 167, 168, 159].

The problem becomes even more difficult for systems described by "infinite-quasiperiodicity" fixed points where the strength of QP modulations keep increasing unbounded along the RG flow and the dynamical critical exponent, z, is infinite, that is, the characteristic timescale t_ξ associated with a length-scale ξ grows faster than any power law of ξ. The $z = \infty$ dynamical scaling leads to a rapidly vanishing gap, which makes it hard to access the critical regime using Quantum Monte Carlo techniques [169, 170, 171, 172]. Tensor network based approaches (see *e.g.* [173]) are also less suited to study 2d QP quantum criticality, due to large entanglement.

In this section, we propose a general RSRG approach to study 2+1d quantum spin models with QP couplings. As in the implementations of RSRG for disordered systems in two dimensions, the RG changes the underlying geometry of the system creating intricate and complex long range interactions [157, 174, 175]. Nevertheless the RG procedure can be efficiently implemented numerically. We focus on the 2d quantum Potts model, with q "colors" ($q = 2$ corresponding to the Ising model). For clean systems, the phase transition separating paramagnetic and symmetry-broken phases is in the classical 3D Potts model universality class, which is a first-order for

$q \geq 3$ [176, 177, 178]. Strong enough QP modulations should smoothe these first-order transitions [179], driving them to a new strong quasiperiodicity fixed point that we describe using RSRG. Our results suggest that the critical properties do not depend on $q > 2$, with the Ising case $q = 2$ being special.

3.4.1 Model

The q-state quantum Potts model is defined via the Hamiltonian

$$H = -\sum_{\langle i,j \rangle} J_{ij}\delta_{n_i,n_j} - \sum_i \frac{h_i}{q} \sum_{n_i,n_i'} |n_i\rangle\langle n_i'|, \tag{3.9}$$

defined on the square lattice with $\langle i, j\rangle$ denoting nearest neighbor pairs, where n_i is a variable on site i that takes one of q possible values. The first term with $J_{ij} > 0$ is a classical ferromagnetic interaction favoring aligned spins, while the second term is a quantum transverse field leading to a paramagnetic phase at large h_i's. For $q = 2$ colors, this coincides with the familiar transverse field Ising model. The model is initially defined on a square lattice; however, we believe our results to be independent of the initial lattice geometry, as RSRG drastically changes the connectivity of the system.

Here, we consider $J_{ij} = f_1(\boldsymbol{k}_1.\boldsymbol{r}) + f_2(\boldsymbol{k}_2.\boldsymbol{r})$, where $\boldsymbol{r} = (i_x, i_y) + \frac{1}{2}(j_x - i_x, j_y - i_y)$, $\boldsymbol{k}_1$, and $\boldsymbol{k}_2$ are two orthogonal unit vectors, and $f_a(x) = f_a(x+\varphi^{-1})$ for some irrational φ, which we take to be the golden ratio, $\varphi = \frac{1+\sqrt{5}}{2}$. Similarly, the fields are taken from an initial potential of the form, $h_i = g_1(i_x) + g_2(i_y)$ with $g_a(x) = g_a(x + \varphi^{-1})$. For concreteness, we focus on the following QP modulations throughout this section,

$$\begin{aligned} \ell_{ij}^{\mathrm{J}} =& 2 + \cos(2\pi\varphi\boldsymbol{k}_1.\boldsymbol{r} + \phi_1) + \cos(2\pi\varphi\boldsymbol{k}_2.\boldsymbol{r} + \phi_2) \\ \ell_i^{\mathrm{h}} =& g(2 + \cos(2\pi\varphi i_x + \phi_3) + \cos(2\pi\varphi i_y + \phi_4)), \end{aligned} \tag{3.10}$$

where g is a parameter driving the transition, $\ell_{ij}^{\mathrm{J}} = -\ln J_{ij}$ and $\ell_i^{\mathrm{h}} = -\ln h_i$ are defined so as to decrease the transient behavior in the RG (see below), and ϕ_i are some constant global phases which we average over. Unless otherwise stated, we take $\boldsymbol{k}_1 = (\sin\theta, \cos\theta)$, with the angle $\theta = \sqrt{2}\pi$. The results do not depend on the details of these distributions.

3.4.2 RG procedure

We now describe the RSRG procedure we use to capture the critical properties of Eq. (3.9), which is mostly similar to that in $1d$ but few extra caveats due to $2d$ geometry. One step of the RG procedure consists of identifying the strongest coupling in the Hamiltonian (which sets the cutoff, Ω) and eliminating it, as follows [157, 180, 174, 181]. If the strongest coupling is a bond J_{ij}, one merges the two spins connected by the bond into a new effective spin (or "cluster") with magnetic moment $\mu_i' = \mu_i + \mu_j$ ($\mu_i = 1$ for initial physical spins). The effective transverse field acting on the cluster is given by second-order perturbation theory, $h_i' \approx \frac{h_i h_j}{\kappa J_{ij}}$ with $\kappa = q/2$; also, any other spin (or cluster) in the system that was connected to either i or j now picks up a bond to the new cluster, with coupling given by $J_{ik}' = \max(J_{ik}, J_{jk})$. If instead the strongest spin is an effective field h_i, one eliminates the site i. Any other pair of sites j, k that were connected to i by bonds now pick up a new effective bond, which we estimate using 2nd order perturbation theory: $J_{jk}' \approx J_{jk} + \frac{J_{ij}J_{ik}}{\kappa h_i} \approx \max(J_{jk}, \frac{J_{ij}J_{ik}}{\kappa h_i})$. This procedure correctly captures the low energy physics as long as $\Omega \gg J_{ij}, h_j$ (broadly distributed couplings) so that perturbation theory is controlled; we will see that the parameter controlling the error in perturbation theory flows to zero upon coarse-graining, leading to asymptotically exact predictions for universal properties.

We numerically run the RG procedure described above starting from a $L \times L$ square lattice. We first focus on the $q = 3$ Potts model – the critical behavior is largely independent of $q \geq 3$. As the system moves along the RG flow, its geometry changes

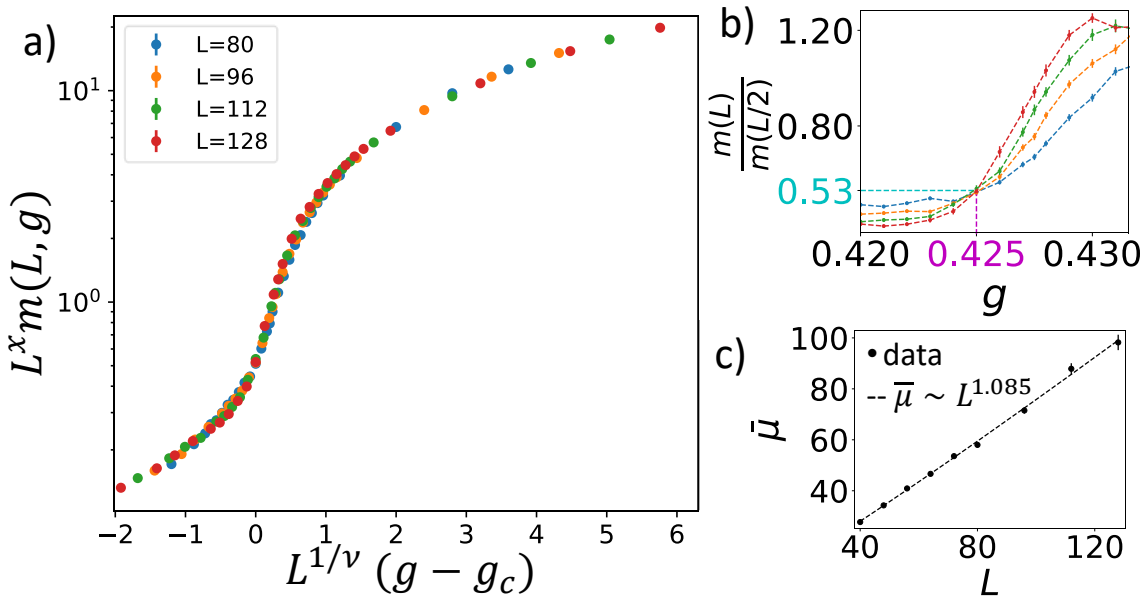

Figure 3.5. Magnetization scaling. **a)** Scaling collapse of the magnetization $m(L, g)$ for $q = 3$ with the correlation length exponent $\nu = 1$, critical coupling $g_c = 0.425$, and magnetization scaling dimension $x = 0.92$. **b)** Plot of the ratio $r(L) = \frac{m(L)}{m(L/2)}$ vs g. In the para- and ferromagnetic phases $r(L)$ depends on L (large g corresponds to a ferromagnet, small g to a paramagnet), while at the critical point this ratio is a constant. Defining the scaling dimension x via $m \sim L^{-x}$, we have $2^{-x} \approx 0.53$ or $x \approx 0.92$. The critical point is $g_c = 0.425$. **c)** Average magnetic moment $\overline{\mu_{\rm M}}$ vs L giving $\overline{\mu_{\rm M}} \sim L^{d_f}$ with $d_f = 1.085 \pm 0.024$. This is consistent with $x + d_f = 2$.

giving rise to graphs of increasingly intricate connectivity. Instead of implementing the RG in the naive sequence described above (i.e., always decimating a single largest coupling), we follow standard techniques [174] to optimize the decimation sequence. (We have checked that at the end of the RG procedure, the optimized and naive decimation sequences yield identical couplings, so this step is *not* an approximation.)

3.4.3 Critical properties

Magnetization and fractal exponent. At the end of the RG, the surviving cluster with moment $\mu_{\rm M}$ determines the magnetization of the system, $m(L, g) = \mu_{\rm M}/L^2$, where L is the linear size of the system. To locate the critical point we plot $r(L, g) =$

$m(L,g)/m(L/2,g)$ vs g for various L; away from the criticality $r(L,g)$ changes with L, while being scale independent at the critical point [181]. The critical magnetization scales as $m(L,g_c) \sim L^{-x}$ giving the crossing value $r(L,g_c) = 2^{-x}$. The average moment of the cluster at the critical point scales as $\mu_{\rm M} \sim L^{d_f}$ with d_f being the fractal dimension of the spins in the cluster. Those two exponents satisfy the scaling relation $d_f + x = 2$. Those quantities are plotted for the $q = 3$ Potts model in Fig. 3.5, and we find $2^{-x} \approx 0.53$ or $x \approx 0.92$ and $d_f = 1.085 \pm 0.024$, consistent with the relation $d_f + x = 2$.

Correlation length. Assuming single parameter scaling with a diverging correlation length $\xi \sim |g - g_c|^{-\nu}$, we expect the following scaling form for the magnetization $m(L,g) = L^{-x} f((g-g_c)L^{1/\nu})$, where f is a universal scaling function. Using the values of g_c, and x obtained from the plot of $r(L)$, we find a nice collapse for $\nu \approx 1$. We now argue that this result $\nu = 1$ holds exactly, at least for some classes of quasiperiodic potentials.

The argument for $\nu = 1$ is as follows. Let us first consider the case where the quasiperiodic modulation is parallel to the lattice vectors, i.e., $\boldsymbol{k}_1 = (1,0)$, $\boldsymbol{k}_2 = (0,1)$ in (3.10). We now consider running the RG for two realizations of the lattice, one at criticality and one detuned by a distance δ. We now look for "defects," or points on the lattice where the two RG realizations begin to diverge (because one of them decimates fields and the other bonds). Defects occur when locally, fields are close ($\lesssim \delta$) in magnitude to the neighboring bonds; thus, a small detuning is enough to change the order of decimations. However, because the quasiperiodic structure is approximated to precision $\sim \delta$ by a rational approximant with period $\sim 1/\delta$, each defect has an almost perfect repeat at a distance $\sim 1/\delta$ (along both lattice directions). This can be seen by observing that $\cos(2\pi\varphi(x + F_n) + \phi) = \cos(2\pi\varphi x + \phi) + \mathcal{O}(\varphi^{-n})$, where F_n is the nth Fibonacci number: defects must repeat along the vertical and horizontal axis, forming a QP tilling, with a length scale $\xi = F_n \sim \varphi^n$, with $\delta \sim \varphi^{-n}$

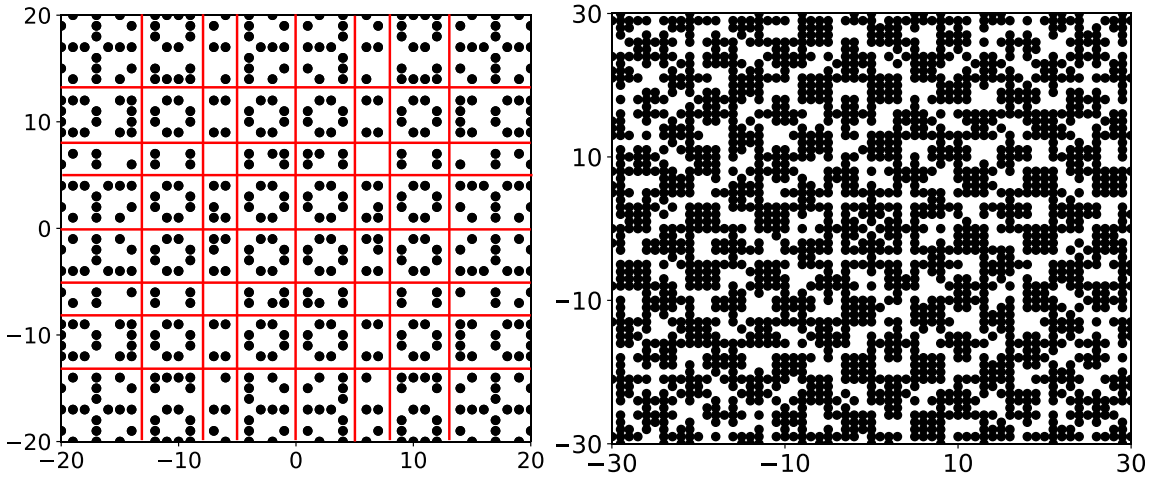

Figure 3.6. Critical defects and quasiperiodic tiling structure. *a*) Geometry of the set $S = \{i : \min\{\ell^{\mathrm{J}}_{ij}\} < \ell^{\mathrm{h}}_i\}$ where ℓ^{h}, ℓ^{J} are defined in (3.10) with the angle $\theta = 0$. We have taken $g = 0.4$ for illustration purposes. Black sites belong to S; white region are sites not belonging to S and. hence, form single-site clusters. We see pockets of black sites separated by 1d section of white sites, marked by red lines; these red lines form a square QP tilling. Local clusters are formed by running RG within the faces of the red tilling and large clusters in later steps of the RG are formed by joining these small local clusters. Defects are breaks in the pattern of inter tile connections away from the critical point. The number of breaks are proportional to the inverse of detuning parameter δ, giving $\nu = 1$. *b*) Geometry of S for $g = g_c = 0.425$ and $\theta = \sqrt{2}\pi$. The structure is not as clear and well defined as in the $\theta = 0$ case but we can still see local puddles in S.

giving $\xi \propto \delta^{-1}$ (see Section 3.1.2 for a similar argument in quantum spin chains). Thus, when the RG reaches length scale $1/\delta$, defects will proliferate and drive the system away from criticality, corresponding to $\nu = 1$. To illustrate the tilling pattern, we define the set $S = \{i : \min\{\ell^{\mathrm{J}}_{ij}\} < \ell^{\mathrm{h}}_i\}$. All sites not belonging to S have local maximum magnetic field and hence can be decimated in one go forming trivial clusters. We plot the set S for $\theta = 0$ in Figure. 3.6. We see a QP lattice formed by trivial clusters. The geometry of defects for non zero θ is less transparent but numerics again suggests $\nu = 1$ (see Figure 3.5) with the the set S showing correlated structures.

We now argue that, if this anisotropy persists under the RG, it leads to a modification of the Harris-Luck bound on ν [163]. The standard argument for this criterion runs as follows. In a large patch of the sample of linear dimension ℓ, the apparent local detuning from the critical point is $\delta_\ell \equiv \langle g \rangle_\ell - g_c \sim \ell^{w-d}$ where w is the wandering exponent. Setting ℓ to the correlation length $\xi \sim \delta^{-\nu}$, we get $\delta_\xi \sim \delta^{\nu(d-w)}$. When δ_ξ is small compared with the global detuning δ, the transition is well-defined. This criterion amounts to $\nu > 1/(d-w)$. Generic patches of a quasiperiodic system have wandering exponent $\mathrm{w} = 0$ in the bulk so the standard Luck criterion reads $\nu > 1/d$. However, this analysis ignores boundary terms due to lines or other sub-dimensional regions of the sample where δ is locally away from its average value. If one includes these boundary contributions, the deviation is $\delta_\ell \sim \ell^{(d-1)-d}$, so that $\nu \geq 1$ regardless of dimensionality. The quasiperiodic Potts model appears to saturate this modified bound, with $\nu = 1$ (up to logarithmic corrections).

Dynamical scaling and RG error. We now turn briefly to the dynamical scaling properties at this transition. One can argue analytically that the timescale for a region of ℓ spins grows at least as $\ln t_\ell \gtrsim \ln^2 \ell$. This scaling follows naturally from the RG rules; recall that these rules involve a factor $\kappa > 1$ at each step. One can check that upon decimating a region of size ℓ to a single spin, one picks up at least $\ln^2 \ell$ factors of κ in the effective couplings (see supplemental material of [156] for a proof), implying an energy scaling $-\ln E_\ell \sim \ln t_\ell \gtrsim \ln^2 \ell$. This scaling can be interpreted as the scaling of the finite size gap of a region of size ℓ. This divergence might be subleading (as it is in the random case), but guarantees "activated" scaling, where t grows faster than any power of ℓ. As we see in Fig. 3.7b, the numerical results are consistent with $\ln t_\ell \sim \ln^2 \ell$, i.e., the same dynamical scaling as in one dimension [84].

A consequence of activated dynamical scaling is that the RG becomes increasingly accurate at late stages. The typical RG error (defined as $\log \Delta_{\mathrm{RG}} \equiv \langle \log(\frac{\max J_{ij}, h_i}{\Omega}) \rangle$, where the max function is over all neighboring terms of Ω, with $\langle \cdot \rangle$ denoting average

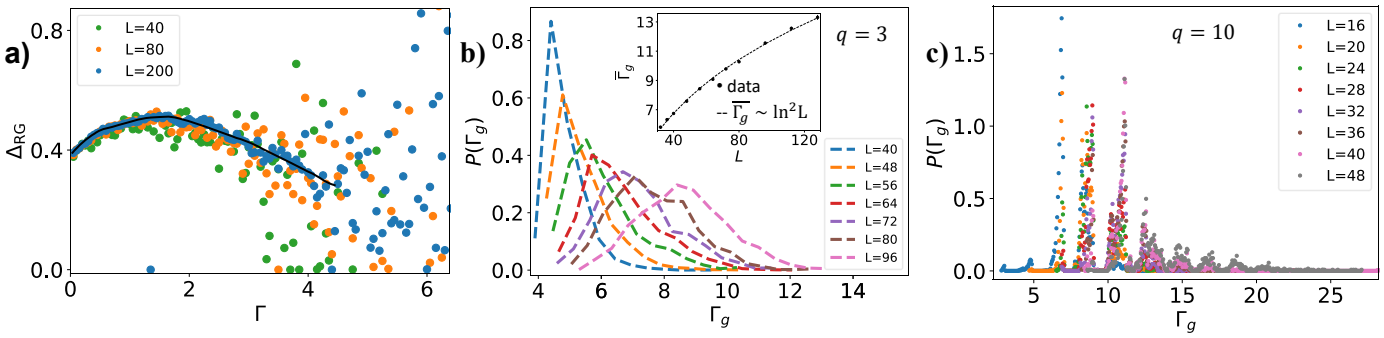

Figure 3.7. RG errors and gap distribution. *a*) Plot of the RG error, Δ_{RG}, vs RG time $\Gamma(\equiv -\ln\Omega)$ at the critical point. Data from 9 different phase realizations are combined and averaged over windows of Γ of size 0.05. We see a trend of the error decreasing with the RG, i.e increasing Γ (the black curve is a guide for the eye), whereas towards the end of the RG the data becomes more scattered and noisy. As we increase system sizes, the onset of the data scattering shifts towards latter stages of the RG, consistent with the noisiness in the error at higher Γ being a finite size effect. *b*) Distribution of logarithmic of gap for $q = 3$, $-\ln \Delta E_g \equiv \Gamma_g$. With increasing system size, the average is increasing with the distribution becoming broader, indicating a broadening of couplings and fields along the RG flow. *Inset:* Scaling of the finite-size gap, showing $\overline{\Gamma}_g$ vs L; the fit is compatible with $\overline{\Gamma}_g \sim \ln^2 L$. Binning window for Γ_g was taken to be 0.5. *c*) Distribution of logarithmic of gap for $q = 10$ with window size of 0.05. Unlike the $q = 3$ case, we see a systematic rise and fall in $P(\Gamma_g)$, with the probability going to zero for some values of the gap. This is reminiscent of the 1d case where a similar banding of couplings and gaps was observed [84].

over a small window of $-\log\Omega$, and several phase realizations) vs $-\ln\Omega(\equiv \Gamma)$ at the critical point is plotted in Fig. 3.7. a). We see that on average, the RG error decreases along the RG flow, suggesting that the RG becomes asymptotically exact, as in the random case [157]. While the system sizes we can access remain away from the asymptotic regime where the RG is fully controlled, we observe very good quality critical data (Fig. 3.5) with no signs of finite-size drifts. Extrapolating these results, we expect the error of a typical RG step to go to zero asymptotically with Γ.

Critical behavior *vs* q**.** We conclude this section by briefly discussing the case of $q > 3$. For $q > 3$, we observe a similar behavior as for $q = 3$; there is a 2nd order transition with the RG becoming more controlled with the flow. The correlation

exponent $\nu = 1$ seems to hold, as expected from the general arguments discussed above. Unsurprisingly, the location of critical point is non-universal and changes with q and θ. The d_f and x exponents appear to be same for all values of $q > 2$, suggesting the same universality class for different q's, though we cannot exclude small differences based on our numerical data. Interestingly, for larger values of q, we observe that the distributions of the gap and of couplings form "bands", with forbidden values in between the allowed bands (see Fig. 3.7.c). This is reminiscent of similar banding properties that were observed in QP quantum spin chains [84]; it would be interesting to investigate whether this can be leveraged to understand this RG analytically in the future.

The case of $q = 2$ (the Ising model), is special. In this case, we find that the RG *does not* flow towards infinite quasiperiodicity, and is therefore not controlled. A similar scenario occurs in 1d *weak* QP modulations are marginally irrelevant [74, 75, 76, 84] at the clean fixed points. However, unlike the 1d case, we observe that even on introducing strong QP modulations, the RG *does not* flow to infinite quasiperiodicity. From the modified version of the Luck criterion, we expect QP modulations to be relevant at the clean Ising transition, driving the system to a finite quasiperiodicity fixed point that cannot be described using RSRG. It would be especially interesting to investigate the nature of this QP Ising transition, as we expect it to be very different from the transitions described in this section — in particular, it likely has a finite dynamical exponent z, as a consequence of the prefactor $\kappa = 1$ in the RG rules.

Part II

Measurement induced phase transitions in monitored quantum circuits

CHAPTER 1

INTRODUCTION

In recent decades, the notions of quantum entanglement and information have emerged as essential ingredients across multiple branches of physics, ranging from quantum many-body systems to black hole physics, and as a resource for quantum computation. Many of these historically disjointed fields are now starting to become more and more entangled. The scrambling of quantum information under unitary evolution into non-local degrees of freedom has emerged as a fundamental ingredient in the understanding of quantum thermalization, chaos, and the spread of errors in quantum computations. As such, the dynamics of quantum information in isolated and open quantum systems has become a central theme in the study of quantum dynamics in the past few years.

In this part of the thesis, we will focus on studying the robustness of the scrambling dynamics in protecting quantum information and entanglement from external disturbances. A quantum system is never perfectly isolated but interacts with an environment, which thus leads to competing forces where, on one hand, the unitary dynamics try to scramble the quantum information across the system, and on the other hand, the external interactions try to irreversibly destroy this information by revealing it to the environment. This also poses a natural challenge for the development of quantum computers.

In the last few years, quantum circuits (Fig.1.1) have proved to be useful minimal but powerful models for exploring ideas related to the question posed above. The robustness of the scrambling dynamics to external interference has been studied by

subjecting the system to random projective measurements which compete to pause the dynamics of the information (see Fig. 1.2). Interestingly, a phase transition characterized by the unitary evolutions ability/inability to scramble extensive amount of information occurs as a function of the rate of the measurements [182, 183, 184]. This dynamical phase transition occurs in the individual quantum trajectories of the evolution – output state after each measurement is randomly selected based on the Born probability rule. When the rate of measurements is above some threshold, the measurements can "unravel" the quantum evolution into trajectories with very little entanglement between distant particles (area law phase). On the other hand, for rate of measurements below the critical threshold, the measurements are not dense enough to destroy enough quantum superposition, and thus an extensive amount of entanglement survives in the steady state (volume law phase).

The presence of a stable volume law phase is closely tied [185, 186, 187] to the ability of the unitary evolution to protect extensive amount of quantum information from the measurements: the non-local degrees of freedom contributing to the volume law form a non-local logical codespace that acts as an encoder for extensive amount of quantum information. The above transition can then be seen in the channel capacity, which measures the amount of information that can be transmitted through the system, as it gradually decays to zero at the critical point [185].[1] This has led to new insights and perspectives on the role of unitary evolution as an efficient quantum encoder protecting quantum information from outside interference.

In conventional systems, global symmetries play a vital role in stabilizing various phases of matter. Many universal properties can be understood from generic symmetric principles without relying on microscopic details. The quantum dynamics of

[1]The transition in the channel capacity need not coincide with the entanglement transition. It does for the simple case considered here but in general the entanglement transition gives an upper bound to the transition in the channel capacity.

a system is also strongly modified in the presence of symmetries. For example, in the presence of U(1) symmetry, there exists a local conserved charge operator that leads to slow hydrodynamics modes at late times which are known to modify the scrambling dynamics of the operators having high overlap with the conserved charge [188, 189]. The conservation laws also lead to a slower growth of entanglement. The Renyi entropies of a sub-region A

$$S_n = \frac{1}{1-n}\mathrm{Tr}\rho_A^n,$$

, where ρ_A is the reduced density matrix for the region A, grows sub-ballistically $\sim \sqrt{t}$ as oppose to the linear $\sim t$ growth in non-symmetric systems (von Neumann entropy $S_1 = -\mathrm{Tr}\rho_A \ln \rho_A$ still grow as $\sim t$) [190, 191, 192, 193]. The central role played by the scrambling dynamics in the stability of the volume law phase thus leads to a natural question: how are measurement-induced phase transitions and phases affected by constraints on the scrambling dynamics imposed by the symmetries?

Previous studies [194] on Z_2 symmetric monitored circuits showed the possibility of having multiple measurement induced phase transitions *inside* the volume law phase. However, the scrambling of Z_2 symmetric modes is much different than that of, let's say, U(1) symmetric modes due to the latter having local conserved charge density. As a result, the U(1) monitored circuits are expected to be fundamentally different than Z_2 symmetric circuits and it is interesting to investigate how the nature of measurement induced phase transition are modified for such systems. In this section, we introduce U(1) monitored circuits and study many-body dynamics of charges and entanglement. We find that in addition to the entanglement transition, these circuits undergo another measurement-induced phase transition *inside* the volume law phase which we call a "charge sharpening" transition. The sharpening transition is a transition in the system's ability/inability to protect the global charge of the system from measurements; in the "fuzzy" phase, measurements are not able to reveal the charge of the system for a long time (to be made precise below), whereas in the

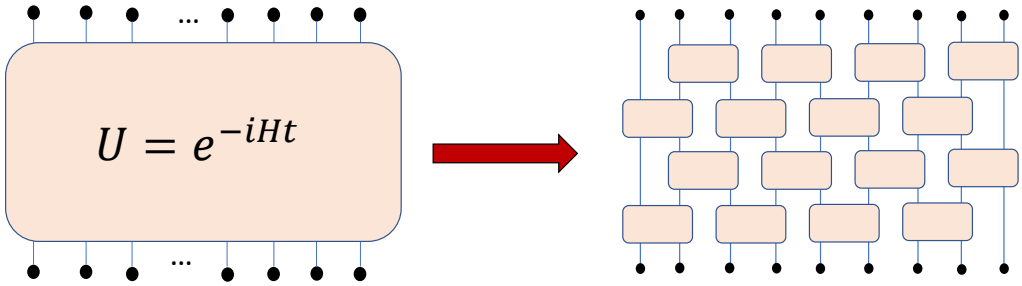

Figure 1.1. Quantum circuits. The Hamiltonian evolution is replaced with a random unitary operator formed out of random unitary bricks. The bricks are arranged in a brickwall geometry. Each black dot represents some d dimensional local Hilbert space. For example, for spin 1/2 chain each black dot corresponds to a spin 1/2 particle.

"sharp" phase the charge fluctuations are destroyed on short time scales independent of the system size. We also study this transition using a novel mapping of the circuit to a stochastic dynamics of classical particles, which can systematically be generalized to the study of any monitored circuits with Abelian symmetries, including Z_2.

The rest of the section is organized as follows. In the rest of the introduction, we introduce and discuss essential features common to all monitored circuits and measurement induced phase transitions. In the next chapter, we study the sharpening transition using two models and conclude that the sharpening transition is universal to U(1) systems and not exclusive to a particular model. We also introduce a mapping from the quantum circuit to a classical statistical mechanics model and study the sharpening transition via this classical model. We defer the technical details and additional results to appendices.

Quantum circuits

As mentioned above, understanding the dynamics and robustness of entanglement in a quantum many-body system is an important but challenging task. In the last few years, a lot of progress has been made in understanding this by replacing the Hamiltonian evolution with a random evolution made of random unitaries arranged in a circuit fashion (see Fig. 1.1). The hope is that the universal and leading features of the dynamics of a choatic many-body system are well captured by the random circuit. This is similar in spirit to using random matrix theory to study the level spectrum properties of a physical Hamiltonian.

The random unitary bricks in Fig. 1.1 can be sampled from a variety of ensembles. Some of these includes, Clifford gates [195, 196], dual unitary gates [197, 198, 199, 200, 201], Haar random gates, instantaneous quantum polynomial-time (IQP) gates [202, 203]. For the purpose of the thesis, we will restrict ourselves to the case of Haar random gates, where the gates are uniformly sampled from the Unitary group using the Haar measure. Other ensembles are also quite useful as they allow for efficient classical simulation and/or analytically tractable calculations.

We expect the average behavior of these random unitary circuits to describe the typical behavior of the circuit. Averaging of random Haar circuit is made possible due to the following theorem [204]

$$E_U[\underbrace{U \otimes \cdots \otimes U}_{k} \otimes \underbrace{U^* \otimes \cdots \otimes U^*}_{k}] \equiv \int dU U^{\otimes k} U^{*\otimes k} \tag{1.1}$$

$$= \sum_{\sigma,\tau} Wg(\sigma\tau^{-1}; k) \left| o_1 \cdots o_k; o^*_{\tau(1)} \cdots o^*_{\tau(k)} \right\rangle \left\langle i_1 \cdots i_k; i^*_{\sigma(1)} \cdots i^*_{\sigma(k)} \right|, \tag{1.2}$$

where k is some integer, the integral dU denotes Haar averaging, σ, τ are members of permutation group S_k, and $|i, o\rangle$ belongs to the Hilbert space on which the unitary U acts; function $Wg(\sigma\tau^{-1})$ are called Weingarten functions. We won't go into details but the above theorem allows for the averaged circuit to be mapped to a 2d classical

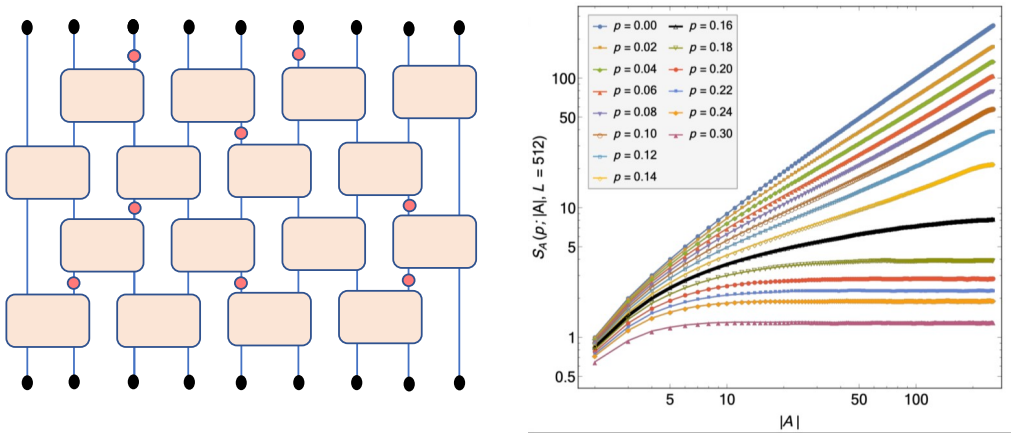

Figure 1.2. Monitored Circuits. *Left.* The circuit model as in Fig. 1.1 but with measurements (red circles) interspersing the unitary evolution. *Right.* It is observed that entanglement of an interval of size $|A| = L/4$ at steady state goes through a phase transition from a phase with volume law entanglement $S \propto |A|$ (for low p) to a phase with area law $S \sim \mathcal{O}(1)$. Plot reproduced from [208].

stat mech model which allows for a better grasp at many many-body properties, at least qualitatively if not quantitatively. We defer the readers to [205, 206, 207] for more details about the stat mech model mapping and subsequent predictions based on it.

Monitored circuits

In the last few years, quantum circuits have also been highly successful in studying the robustness of these properties to external interference. For example, any measurement of a spin will lead to the spin becoming disentangled from the rest of the system. One way to model this disruption caused by the measurements is to take the circuit model in Fig. 1.1 and intersperse the unitary gates with projective measurements of some operator; see Fig. 1.2. These modified circuits are called monitored circuits for obvious reasons; sometimes they are also referred to as hybrid circuits. In the absence of measurements, entanglement of an interval A with rest of the system A_c scales with the volume of the interval $|A|$ [209]; the entanglement is thus volume

law, $S \sim |A|$. Surprisingly, the entanglement remains volume law for a finite range of rate of measurements, p. There system goes through a measurement induced phase transition at p_c, such that for $p > p_c$ the system is in what is known as the area law phase where the entanglement is independent of the interval size, $S \sim \mathcal{O}(1)$.

Quantum channel vs trajectories

An open quantum system is coupled to an environment and it is the combined dynamics of the system (S) + environment (E) that is given by unitary evolution; tracing out E from the resulting combined evolution then gives a mixed density matrix for the system. The unitary evolution of SE can be written as $U |\psi_0\rangle |0\rangle_E = \sum_m K_m |\psi_0\rangle |m\rangle_E$, where $|m\rangle_E$ are orthonormal. Tracing out E gives a quantum channel description for the system with the initial density matrix $\rho_0 \equiv |\psi_0\rangle \langle\psi_0|$ evolving to $\rho(t) = \sum_m K_m \rho_0 K_m^\dagger$. The operators K_m, called Kraus operators, satisfy $\sum_m K_m K_m^\dagger = \mathbb{I}$ and system is said to be acted on by a quantum channel; unitary evolution is a special case of quantum channel with a single Kraus operator.

However, as noted above, we are interested in cases where the system is evolving under the influence of unitary gates + projective measurements. In terms of quantum channels this would mean following a particular "trajectory" m such that $\rho \to K_m \rho K_m^\dagger$ with K_m being one of the many possible Kraus operators. Different m then corresponds to various possible measurement outcomes. For projective measurements, K_m are the projection operator on the subspace associated with the measurement outcome. For unitary + projective measurement dynamics as shown in Fig. 1.2 K_m is made up of random unitary gates and projection operators to m. From now on, we will denote the measurement outcomes by $\mathbf{m}$ denoting the fact that we have multiple measurement locations and outcomes. We further break down $\mathbf{m}$ to $\mathbf{m} = \{\mathbf{X}, \mathcal{M}(\mathbf{X})\}$ where $\mathbf{X}$ are measurement locations in spacetime and $\mathcal{M}(\mathbf{X}$ are the corresponding measurement outcomes.

We will be concerned with general properties of the single-trajectory state $\rho_{\mathbf{m}} \equiv K_{\mathbf{m}} \rho K_{\mathbf{m}}^{\dagger}$. (As a concrete example, consider the purity $\Pi_{\mathbf{m}} = \mathrm{Tr}(\rho_{\mathbf{m}}^2)/(\mathrm{Tr}\rho_{\mathbf{m}})^2$.) We then average over quantum trajectories, weighting each set of measurement outcomes by its probability of occurrence, i.e., the Born probability $p_{\mathbf{m}} = \mathrm{Tr}(\rho_{\mathbf{m}})$. Finally, we average the answers across the ensemble of quantum circuits.

A few comments are in order here.

1. For an initially pure state $|\psi\rangle$ the Born probability takes the familiar form $p_{\mathbf{m}} = \|K_{\mathbf{m}}|\psi\rangle\|^2$, i.e., it is just the norm of the projected state. For a series of measurements interspersed with unitary gates, one can pick each measurement outcome based on the Born probability or *equivalently* apply a set of projectors at random and evaluate the probability of the entire measurement history by computing the norm of the state at the end of the trajectory.

2. There are four different types of average that we will consider here: (i) the quantum expectation value of an observable A in a single trajectory $\rho_{\mathbf{m}}$, namely $\mathrm{Tr}(A\rho_{\mathbf{m}})/\mathrm{Tr}\rho_{\mathbf{m}}$, which we will write as $\langle A \rangle_{\mathbf{m}}$; (ii) the (Born-weighted) average of a single-trajectory function, such as purity or entanglement entropy, over quantum trajectories (measurement outcomes); (iii) the average over unitary gates, chosen with Haar measure; and (iv) the average over spacetime points where the measurements occur (measurement locations). In much of this work, we will present results for which averages (ii)-(iv) have been done. We will use the notation $[\cdot]$ for this full average. At some point it will be useful to separate these averages. In these cases we will use the explicit notations $\sum_{\{\mathcal{M}(\mathbf{X})\}}(\cdot)$, $\mathbb{E}_U(\cdot)$, and $\mathbb{E}_{\mathbf{X}}(\cdot)$ for averages over measurement outcomes, gates, and measurement locations respectively. We will also use a shorthand notation $\mathbb{E}_{\mathbf{m}} \equiv \sum_{\mathbf{m}} p_{\mathbf{m}}(\dots)$ to denote summation over all possible measurement locations $\mathbf{X}$ including appropriate probability factors of p and $1-p$, and over all measurement outcomes $\mathcal{M}(\mathbf{X})$, including the associated Born probability factor $p_{\mathbf{m}}$.

3. It is crucial that the quantities of interest to us are *nonlinear* functions of $\rho_{\mathbf{m}}$ [183], such as $\Pi_{\mathbf{m}}$. To see the significance of this, let us compare the quantity $\Pi_{\mathbf{m}}$ to that of some simple expectation value. In $\rho_{\mathbf{m}}$, the expectation value of a local operator A would be $\mathrm{Tr}(A\rho_{\mathbf{m}})/\mathrm{Tr}\rho_{\mathbf{m}}$. Averaging this over trajectories (measurement outcomes) with the Born probabilities would simply give infinite temperature behavior [2]: $\sum_{\{\mathcal{M}(\mathbf{X})\}}(p_{\mathbf{m}}\langle A\rangle_{\mathbf{m}}) = \sum_{\{\mathcal{M}(\mathbf{X})\}}\mathrm{Tr}(A\rho_{\mathbf{m}}) = \mathrm{Tr}(A\rho(t))\approx \mathrm{Tr}(A)/\mathrm{Tr}(1)$, where $\rho(t) = \sum_{\{\mathcal{M}(\mathbf{X})\}} K_{\mathbf{m}}\rho K_{\mathbf{m}}^{\dagger}$ describes the dynamics of the density matrix in the case where the environment does not monitor or keep track of the measurement outcomes. By contrast, $\sum_{\{\mathcal{M}(\mathbf{X})\}}\Pi_{\mathbf{m}}p_{\mathbf{m}} = \sum_{\{\mathcal{M}(\mathbf{X})\}}\mathrm{Tr}(\rho_{\mathbf{m}}^2)/\mathrm{Tr}\rho_{\mathbf{m}}$, which cannot simply be written in terms of $\rho(t)$. The averaged density matrix $\rho(t)$ is blind to measurement transitions; only nonlinear functions of single-trajectory wavefunctions detect it.

[2]The ensemble-averaged $\rho(t)$ resulting from maximally-random, local, open-systems dynamics is indistinguishable from an infinite temperature state over distances $\sim t$.

CHAPTER 2

U(1) SYMMETRIC MONITORED CIRCUITS

The plan for this chapter is as follows. In Sec. 2.1 we specify the models we have explored and present some general considerations on their steady state phases and dynamics. In Sec. 2.2 we present numerical results for U(1)-symmetric qubit chains. In Sec. 2.3 we present a tractable limit in which the model can be mapped onto the statistical mechanics of constrained random walkers. In Sec. 2.4 we present numerical results for the transfer matrix of this statistical model. Finally in Sec. **??** we summarize our results and discuss their broader implications. This chapter is based on [210].

2.1 Overview of Results

In this section we will introduce a family of U(1)-symmetric circuits, and present some general observations concerning their steady-state phase structure and entanglement dynamics. The numerical evidence supporting these observations will be presented below, in Secs. 2.2 and 2.4.

2.1.1 Model

Following [185], we consider a one-dimensional chain in which each site hosts a two-level system ("qubit") and a d-level system ("qudit"), i.e., the on-site Hilbert

space is $\mathbb{C}^2 \otimes \mathbb{C}^d$ for $d > 1$ and $\mathbb{C}^2$ for $d = 1$. The dynamics will consist of local unitary gates and measurements, which are chosen to conserve the U(1) charge

$$\mathcal{Q} \equiv \sum_i \mathfrak{q}_i \otimes \mathbb{I}_i, \text{ where } \mathfrak{q}_i = (\sigma_i^z + 1)/2 \tag{2.1}$$

is acting on the ith site of the chain of length L and $\mathbb{I}$ is the identity matrix on the qudits. These chains evolve under (i) unitary two-qubit gates, acting on nearest neighbor sites, which conserve the global charge $\mathcal{Q}$, and (ii) single-site projective measurements in which the qubit is measured in its Z basis and the qudit is simultaneously measured in some reference basis [1]. At each time-step, a given site is measured with probability p; for specificity, we assume that when this happens both the qubit *and* the qudit are measured, so the measurement acts on that site as a rank-1 projector. The symmetry-preserving two-site unitary gates are arranged in a brickwork geometry and take the form

$$U_{i,i+1} = \begin{pmatrix} U^0_{d^2\times d^2} & 0 & 0 \\ 0 & U^1_{2d^2\times 2d^2} & 0 \\ 0 & 0 & U^2_{d^2\times d^2} \end{pmatrix}, \tag{2.2}$$

where i labels a site, $U^{\mathfrak{q}}_{D\times D}$ is a unitary matrix of size $D \times D$ acting on the charge $\mathfrak{q}_1 + \mathfrak{q}_2 = \mathfrak{q} \in \{0, 1, 2\}$ sector (a local charge is defined to take values 0 and 1), and D is the dimension of the Hilbert space of the charge sector. Each matrix is drawn independently from the Haar random ensemble of unitary matrices of the appropriate size.

We present numerical results for this class of circuits in two limits. First, we consider the limit $d = 1$, where there is no qudit degree of freedom, and one simply

[1] Since the unitaries acting on the qudits are random, the randomizing measurement basis is superfluous.

has a chain of qubits interacting via gates that conserve the charge $\mathcal{Q}$. In this limit, we obtain numerical results by direct time evolution. Second, we consider the complementary limit $d = \infty$, in which we can map the problem to a statistical mechanics model and explicitly write down a transfer matrix that generates the observables of interest. The phase diagrams in the two complementary limits are similar.

The qubit-only ($d = 1$) model is directly realizable in existing quantum processors. The $d > 1$ model is perhaps less natural experimentally, but could be realized in circuit quantum electrodynamics setups [211] in which superconducting transmon qubits are coupled to multilevel superconducting cavities (qudits), or by blocking multiple qubits together (e.g. $d = 2$ could be realized as a two-leg ladder of qubits). Regardless of experimental implementation, we expect the $d > 1$ models to capture the generic universal behavior of phases and transitions, while allowing greater theoretical control in the large-d limit.

2.1.2 Results

In the following, we unveil a charge sharpening transition that takes place before the entanglement transition in two distinct models of monitored U(1) symmetric random quantum circuits. Our main results are summarized in Fig. 2.1 and discussed in more detail below.

2.1.2.1 Entanglement transition

A general feature of unitary-projective circuits is the presence of an *entanglement transition*, separating a phase where initially unentangled states develop volume-law entanglement from one where their entanglement remains area-law at all times. We briefly review the general properties of this transition and discuss how they are modified by the presence of a conservation law.

This transition occurs at some critical measurement rate p_c. In the volume-law phase, the half-system entanglement entropy grows linearly in time and saturates on

timescales $t \sim L$. At times $t > L$, the entanglement entropy (averaged over circuits and trajectories) reaches a steady state value $[S(L/2)] = cL$, where c is a constant that decreases continuously to zero at p_c. At $p = p_c$, we have that $[S_n(L/2)] = \alpha_n \log L$, where α_n (which generally depends on the Rényi index n) is part of the universal critical data [183, 212].

An equivalent way to understand the entanglement transition is as a "purification transition" for an initially mixed state [185]. For $p < p_c$, an initially mixed state for a system of size L evolves to a pure state on a timescale $t_\pi \sim \exp(L)$, whereas for $p > p_c$ purification happens on a timescale that grows sub-linearly in L. If one takes the limits $L \to \infty$, $t/L =$ constant, the purity of an initially mixed state for $p < p_c$ is essentially constant in time: i.e., the steady state is defined to be at early times compared with the slow purification dynamics for $p < p_c$.

The purity of an initially mixed state on timescales $t \sim L$ can be used to define an effective order parameter for the volume-law phase, as follows [213, 212]. Consider evolving a pure state along some trajectory until times $t \sim L$, and then entangling some local degree of freedom with an ancilla qubit. The reduced density matrix of the system is now a rank-2 mixed state. For $p < p_c$, this mixed state remains mixed for an exponentially long time. Therefore, by evolving for another $t \sim L$ and then measuring the entanglement entropy of the ancilla (which is equivalent to measuring the purity of the system density matrix in this setup), one can extract a local order parameter for the volume-law phase [213]. By studying the correlations of this local order parameter—e.g., by coupling in two ancillas at distinct spacetime points and tracking their mutual information—it was established (in the absence of the U(1) symmetry) that the critical theory has an emergent Lorentz invariance with dynamical scaling exponent $z = 1$.

One of our results is to locate and characterize this entanglement transition in the presence of the U(1) conservation law. In the $d \to \infty$ limit, we find that $p_c = 1/2$,

exactly as in the absence of a conservation law. Moreover, the entanglement transition corresponds to a percolation transition. For $d = 1$, we find that $p_c = 0.105(3)$ moves to substantially lower measurement rate than in the generic circuit without a conservation law ($p_c^{\text{Haar}} \approx 0.17$ [212]). The correlation length exponent $\nu = 1.32(6)$ is close to the percolation value 4/3, but the coefficients α_n differ from the percolation value as well as the value for Haar-random circuits without a $U(1)$ symmetry. Finally, we find compelling numerical evidence that the dynamical scaling $z = 1$ holds at this critical point. That this holds regardless of the diffusive ($z = 2$) dynamics of the U(1) conserved charge is perhaps puzzling at first sight. We return below in Section 2.1.2.3 to the resolution of this puzzle.

2.1.2.2 Charge-sharpening transition

In addition to changing the critical properties of the entanglement transition at p_c, the conservation law gives rise to a *distinct* "charge-sharpening" transition at a measurement rate $p_\#$ inside the volume-law phase. The charge-sharpening transition separates a "charge-sharp" phase for $p > p_\#$, in which the measurements along a typical trajectory can rapidly collapse an initial pure superposition (or mixture) of different charge sectors, and a "charge-fuzzy" phase where this collapse is parametrically slower occurring on a time scale $t_\# \sim L$. Specifically, we can distinguish charge-sharp or fuzzy behavior by the variance of the conserved charge $\mathcal{Q}$ in Eq. (2.1) over a single trajectory, averaged across trajectories and samples, i.e.,

$$[\delta\mathcal{Q}^2] = [\langle\mathcal{Q}^2\rangle_{\mathbf{m}} - \langle\mathcal{Q}\rangle_{\mathbf{m}}^2], \tag{2.3}$$

where the quantity in parentheses is the *quantum* number variance in a given trajectory. In the sharp phase, $[\delta\mathcal{Q}^2] = 0$ while in the fuzzy phase it remains non-zero at times of order $t \sim L$.

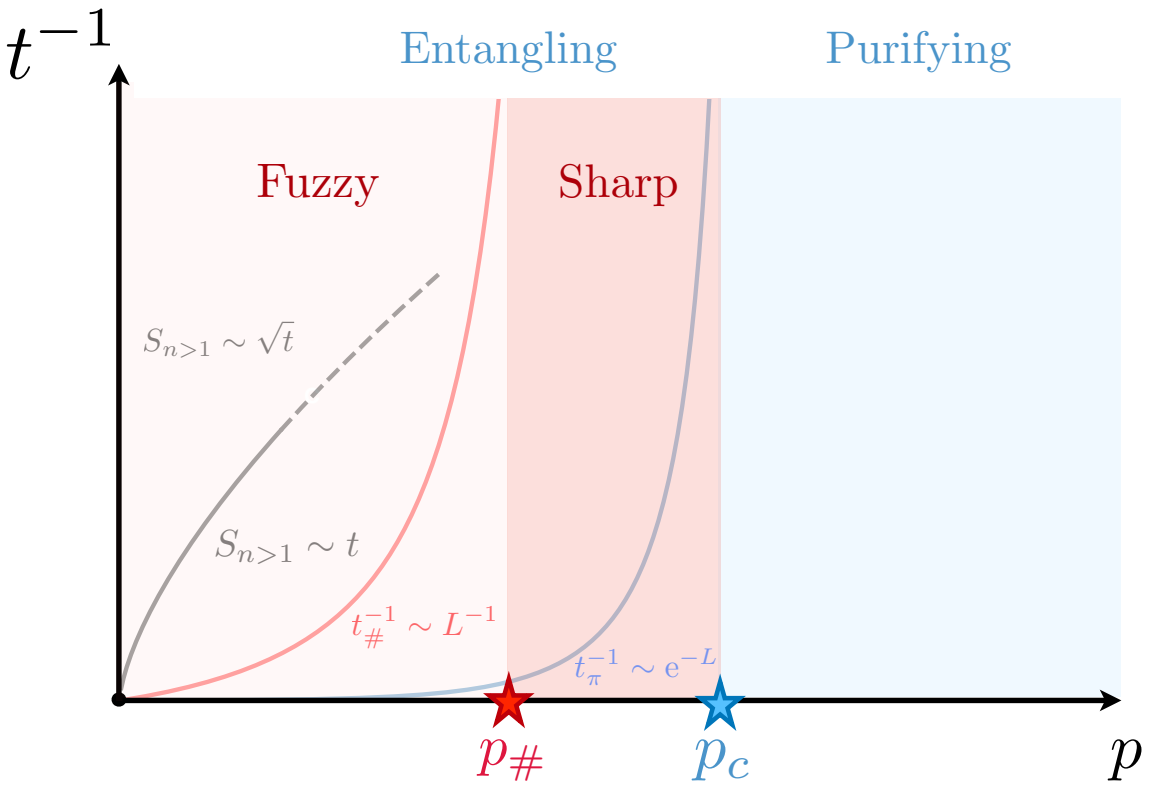

Figure 2.1. Phase diagram and crossover time scales in U(1) symmetric monitored quantum circuits. Our numerical results indicate that there are two distinct phases in the entangling (volume-law) regime $p < p_c$, separated by a charge-sharpening critical point as $p = p_{\#}$. In the charge-fuzzy phase ($p < p_{\#}$), we identify three relevant time scales in the dynamics: For a large enough system, first (1) average Rényi entropies crossover from diffusive $[S_{n>1}] \sim \sqrt{t}$ to ballistic $\sim t$ scaling over a time scale $\sim p^{-3/2}$, then (2) charge sharpens after the crossover time scale $t_{\#} \sim L$, and finally (3) the system purifies over a much long time scale $t_{\pi} \sim \mathrm{e}^{L}$.

The dynamics of charge sharpening at small p can be qualitatively understood in terms of a simple classical model, in which one ignores the spatio-temporal correlations between measurements. One can then ask how many independent density measurements $\mathcal{N}_M$ are required to distinguish systems with N particles on L sites from those with $N-1$ particles on L sites, where $n \equiv N/L = \mathcal{O}(1)$. Assuming Gaussian density fluctuations (as in the $p = 0$ thermal state) we expect the N-particle and

$(N-1)$-particle states to become distinguishable when $\mathcal{N}_M \sim L^2$.[2] Since $\mathcal{N}_M = pLt$ in the circuits we consider, sharpening happens on a crossover timescale $t_\# \sim L/p$. For timescales $t \geq t_\#$, we expect that $[\delta\mathcal{Q}^2] \sim \exp(-t/t_\#)$. This follows, e.g., from using the central limit theorem to estimate the probability that an N particle state will give an average density of $n \pm 1/L$ after pLt measurements. This simple model of the volume law phase predicts that a crossover to charge sharpening should take place on a timescale $t_\# \sim L/p$, consistent with our numerical findings (see Sec. 2.2 and 2.4), and parametrically faster than purification. Importantly, at any finite t/L, $[\delta\mathcal{Q}^2]$ remains non-zero in the fuzzy phase (albeit exponentially small for $t \gg t_\#$).

By contrast, for $p > p_\#$, charge-sharpening happens on a timescale that is sublinear (logarithmic) in system size. In the limit $L \to \infty, t/L =$ constant, each trajectory has a definite charge. Thus there is a sharp phase transition at $p_\#$, for which $[\delta\mathcal{Q}^2]$ acts as an order parameter. Our numerical results also indicate that charges become devoid of quantum superposition in some regions of space-time exhibiting locally minimal spacing of measurements (see Sec. 2.4).

As with the entanglement transition, one can probe the charge-sharpening transition by coupling an ancilla to the circuit. One entangles the ancilla with the system such that each ancilla state is coupled to a system state with a different value of $\mathcal{Q}$. The system-ancilla entanglement vanishes when $\mathcal{Q}$ sharpens under the circuit dynamics.

2.1.2.3 Entanglement dynamics

We now turn to the dynamics of entanglement at times of order unity. Recall that, absent measurements, the Rényi entropies $S_n \sim \sqrt{t}$ for all $n > 1$ in random circuits

[2]This can seen by the central limit theorem as follows: assuming each measurement outcome to be independent, the statistical error in the outcomes of the measurement of charge density goes as $1/\sqrt{\mathcal{N}_M}$. To distinguish the states with global charge N and $N-1$, we require this error to become smaller than $\sim 1/L$. This gives $\mathcal{N}_M \sim L^2$.

with U(1)-symmetric gates [191, 214, 192]. This diffusive entanglement dynamics appears to be a generic property of random circuits, so one might expect it to hold throughout the volume-law phase. If it held at the critical point, it would prevent the critical theory from being a conformal field theory (CFT). We now discuss why Rényi entropies in fact scale *ballistically* for any non-zero measurement probability, $p > 0$, allowing both the sharpening and entanglement transitions to obey relativistic $z = 1$ dynamic scaling.

First, we review the argument for diffusive scaling in the absence of measurements [191, 214, 192]. This phenomenon arises from rare fluctuations that leave a region empty (or maximally filled), as follows. Consider, for concreteness, the dynamics of the initial product state for the qubit $|\psi\rangle = \otimes_{i=1}^{L} |+_x\rangle_i$ where $|+_x\rangle = \frac{1}{\sqrt{2}}(|0\rangle + |1\rangle)$. Suppose we are interested in the entanglement across a cut at $L/2$ at some later time t. We can divide the system into three regions: a central region of radius $\ell = \sqrt{Dt}$ centered at the entanglement cut, and regions to the left and right. Define

$$|\psi_{\text{dead}}\rangle = \bigotimes_{i=1}^{L/2-\ell} |+_x\rangle_i \bigotimes_{i=L/2-\ell+1}^{L/2+\ell} |0\rangle_i \bigotimes_{i=L/2+\ell+1}^{L} |+_x\rangle_i. \tag{2.4}$$

Initially, $|\langle\psi_{\text{dead}}|\psi\rangle| = 2^{-2\ell}$. After evolving for time t, $|(\langle\psi_{\text{dead}}|U_t^\dagger)(U_t|\psi\rangle)| = 2^{-2\ell}$ by unitarity. However, $U_t|\psi_{\text{dead}}\rangle$ is a product state with respect to the cut at $L/2$: by construction, t is not long enough for particles to have diffused to the entanglement cut, and unless there is a $|10\rangle$ or $|01\rangle$ configuration at the cut the gates acting across the cut cannot generate entanglement. The largest Schmidt coefficient of $U_t|\psi\rangle$ is its maximal overlap with *any* product state, so we can lower-bound the largest Schmidt coefficient of $U_t|\psi\rangle$ as $2^{-2\ell} = 2^{-\sqrt{Dt}}$, and therefore $S_\infty \leq 2\ell \ln 2 \sim \sqrt{Dt}$. All Rényi entropies with $n > 1$ are dominated by this largest Schmidt coefficient and grow as $\sqrt{t}$. The Von Neumann entropy S_1 is dominated instead by *typical* Schmidt coefficients:

the number of these grows exponentially in t, but they are also exponentially small in t and are therefore subleading for $n > 1$.

We now address how this argument changes when $p > 0$. In a typical trajectory, on a timescale t, there are $p\ell t \sim pt^{3/2}$ measurements in the putative dead region near the entanglement cut, and about half the measurements observe a qubit to be in the charge state $|1\rangle$. There are rare circuits with few measurements near the cut, as well as rare histories in a typical circuit where all the measurements yield the same outcome $|0\rangle$. However, both are *at least* exponentially suppressed in ℓ and cannot dominate the trajectory-averaged entanglement (since *any* trajectory contributes at most $\sim t$ entanglement, and in any case these atypical trajectories have unusually slow entanglement growth). Therefore, to compute the trajectory-averaged Rényi entropies it suffices to consider trajectories with typical measurement locations and typical outcomes. In typical trajectories, one observes a $|1\rangle$ charge after $\mathcal{O}(1)$ measurements in the region near the cut, so the putative dead region survives only until a time $t \sim p^{-2/3}$. At longer times, the overlap of the wavefunction with dead regions is zero. We conclude that the trajectory-averaged Rényi entropies $[S_n]$ grow linearly in time whenever $p > 0$ [3]. We also note that, the existence of diffusive hydrodynamic modes, which are a purely classical phenomena, does not affect the $z = 1$ dynamical scaling at the volume-to-area law entanglement transition at p_c. Our numerical estimates of the dynamic exponent in Sec. 2.2 are consistent with this result that $z = 1$ scaling applies and diffusive hydrodynamics decouples also at the charge-sharpening transition at $p_\#$.

[3]Though other quantities such as $\log[e^{-S_n}]$ are dominated by rare dead-region contributions and do exhibit $\sqrt{t}$ growth due to rare dilute measurement locations. The parametrically strong discrepancy between the average purity and the average Rényi entropies is also seen numerically in our statistical model approach (Sec. 2.4).

2.2 Numerics on qubit chains

In this section we present numerical results on a model of random U(1)-conserving gates acting on a chain of qubits (i.e., the $d = 1$ limit of the general model in Sec. **??**). Specifically, in the basis of the adjacent qubits $\{|\downarrow\downarrow\rangle, |\uparrow\downarrow\rangle, |\downarrow\uparrow\rangle, |\uparrow\uparrow\rangle\}$ the two-qubit gates at site i take the block diagonal form

$$U_{i,i+1} = \begin{pmatrix} e^{i\phi_0} & & & \\ & U^1_{2\times 2} & & \\ & & & e^{i\phi_1} \end{pmatrix} \tag{2.5}$$

where ϕ_1 and ϕ_0 are chosen at random from the interval $[0, 2\pi)$ and $U^1_{2\times 2}$ is a Haar-random 2×2 unitary matrix that can be parameterized by 4 angles

$$U^1_{2\times 2}(\alpha, \phi, \psi, \chi) = e^{i\alpha} \begin{pmatrix} e^{i\psi}\cos\phi & e^{i\chi}\sin\phi \\ -e^{-i\chi}\sin\phi & e^{-i\psi}\cos\phi \end{pmatrix} \tag{2.6}$$

where $0 \leq \phi_{0,1} \leq \frac{\pi}{2}$ and α, ψ, χ, and ϕ are chosen so that $U^1_{2\times 2}$ is uniformly sampled from U(2) [4]. In between layers of gates, projective measurements are performed: with a probability p, the qubit is projected onto $|\uparrow\rangle$ or $|\downarrow\rangle$ given by the Born rule. Utilizing the conservation law, we work in definite number-sectors to reduce the memory load of the exact numerics.

The conservation law leads to different charge sectors defined by eigenspaces of $\mathcal{Q}$ in Eq. (2.1). We will typically focus on charge sectors near the central subspace ($\mathcal{Q} = L/2$).

---

[4] To obtain a uniform distribution over $U(2)$ we must pick $\alpha, \psi, \chi \in [0, 2\pi)$ and $\xi \in [0, 1]$ uniformly and compute $\phi = \arcsin\sqrt{\xi}$.

2.2.1 Entanglement transition

We begin by locating the entanglement transition point p_c in this model. In order to probe the location of the critical point and the correlation length critical exponent, we study two quantities that have been identified as good measures of the transition: the tripartite mutual information [212] and an order parameter defined through the use of an ancilla [213] that is coupled to one charge-$\mathcal{Q}$ sector. In the following it is essential that we use an accurate estimate of p_c to be able to numerically disentangle it from the charge sharpening transition at $p_{\#}$.

First, the tripartite mutual information for the Rényi index n is defined as

$$\begin{aligned}\mathcal{I}_{3,n}(A,B,C) \equiv\ & S_n(A)+S_n(B)+S_n(C)- \\ & -S_n(A\cup B)-S_n(A\cup C)-S_n(B\cup C)+ \\ & +S_n(A\cup B\cup C),\end{aligned} \tag{2.7}$$

where we have chosen regions $A, B,$ and C to be adjacent regions of size $L/4$ and $S_n(A)$ is the Rényi entropy defined in Eq. (**??**). For $\mathcal{I}_{3,n}$ at late times ($t = 4L$) we apply the finite size scaling hypothesis $\mathcal{I}_{3,n} \sim f(L^{1/\nu}(p-p_c))$, to locate the critical point, where $f(x)$ is a scaling function and ν is the correlation length exponent. The data for $n = 1$ is shown in Fig. 2.2(a) where we find the data collapses with the minimum χ^2 for the choice of $p_c = 0.105(3)$ and $\nu = 1.32(6)$. A similar analysis can be performed for the other Rényi entropies and the resulting values of p_c and ν are similar for all $n \geq 1$ investigated, we find $p_c = 0.103(4), 0.12(2), 0.12(1)$ and $\nu = 1.37(8), 1.47(3), 1.5(2)$ for $n = 2, 5, \infty$, respectively.

At the critical point, the bipartite entanglement entropy shows a logarithmic dependence on the system size and the coefficient of the logarithmic divergence shows strong Rényi index dependence (Fig. 2.2(c)). This behavior can be described by

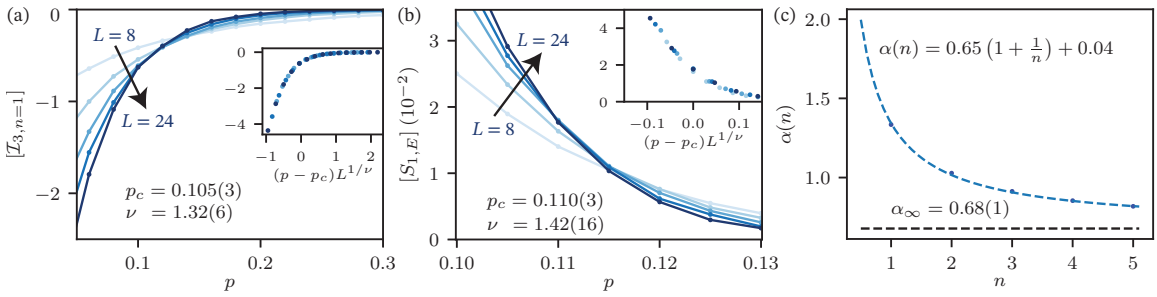

Figure 2.2. Entanglement transition in qubit chains. (a) Data and collapse of the tripartite mutual information, $\mathcal{I}_{3,n=1}$, used to determine the critical point of the entanglement transition, $p_c = 0.105(3)$ and the correlation length exponent, $\nu = 1.32(6)$. (b) Data and collapse of the entanglement transition order parameter, $[S_{1,E}]$, used as an alternative method to determine the critical point of the entanglement transition, $p_c = 0.110(3)$, and the correlation length exponent $\nu = 1.42(16)$. (c) At the critical point, the bipartite entanglement entropy shows logarithmic scaling with the system size. The coefficient of the logarithm has strong Rényi index dependence that can be described by a functional form $\alpha(n) = 0.65(1)\left(1 + \frac{1}{n}\right) + 0.04(1)$. This closely resembles the standard result for the groundstate of a CFT, but has an offset slightly larger than zero.

$$S_n(p_c, L) \sim \alpha(n) \ln L, \;\; \alpha(n) = 0.65(1)\left(1 + \frac{1}{n}\right) + 0.04(1). \tag{2.8}$$

Apart from the small offset, this Rényi index dependence matches the result one expects for the ground state of a CFT [215], $\alpha_{\mathrm{CFT}}(n) = \frac{c}{6}\left(1 + \frac{1}{n}\right)$. The coefficients in Eq. (2.8) clearly differ from those at the measurement induced transition without a conservation law [212].

As an alternative way of locating the entanglement transition, we also study the "order parameter" [213]. In order to have the ancilla couple to the system within a particular global charge sector, we consider the qubits at two adjacent sites i and $i+1$ to be in the entangled state with an ancilla: $|\Psi_0\rangle = \frac{1}{\sqrt{2}}(|\uparrow\downarrow\rangle\,|1\rangle + |\downarrow\uparrow\rangle\,|0\rangle)$ where the ancilla has orthogonal basis states $|1\rangle$ or $|0\rangle$. We then evolve the system in time $t = 2L$ without measurements in order to create a state $|\Psi\rangle = \frac{1}{\sqrt{2}}(|\psi_1\rangle\,|1\rangle + |\psi_0\rangle\,|0\rangle)$ where $|\psi_{0,1}\rangle$ are orthogonal and in the same charge sector. We then run the circuit

with measurements for an additional time $2L$ and compute the von Neumann entropy of the ancilla, which we denote as $S_{1,E}$ (as it probes the entanglement transition).

The results for the von Neumann entanglement entropy of the ancilla $S_{1,E}$ are shown in Fig. 2.2(b), and are consistent with $\mathcal{I}_{3,n}$ data: From the scaling ansatz $S_{1,E} \sim f_E((p-p_c)L^{1/\nu})$, where $f_E(x)$ is a universal scaling function, we obtain $p_c = 0.110(3)$ and $\nu = 1.4(2)$ in good agreement with $\mathcal{I}_3$.

Summarizing these results, the entanglement transition in U(1)-symmetric circuits has a critical exponent ν that is consistent with the value for Haar-random circuits with no symmetries, although the nonuniversal p_c has drifted down from the Haar value $p_c^{\text{Haar}} \approx 0.17$ (as one might expect since each gate cannot generate as much entanglement). At $p = p_c$ we extract the dynamical exponent of the entanglement transition using the scaling ansatz $[S_{1,E}] \sim g_E(t/L^z)$, which shows a good quality as seen in Fig. 2.3 for $z = 1$ and $g_E(x)$ some universal scaling function. Again, this result is consistent with the non-conserving case. While we have focused on $\mathcal{Q} = L/2$ we have checked that for the largest system sizes considered p_c is only very weakly affected for $\mathcal{Q} = L/2 - 1$ (not shown).

2.2.2 Charge sharpening transition

We now turn to estimating $p_\#$ in two ways: the charge variance of a state and the entropy of an ancilla entangled with two different number sectors.

First, we compute the variance of the total charge (Eqs. (2.1) and (2.3)). For a trajectory that lies in a well defined charge sector, $\delta\mathcal{Q}^2 = 0$, otherwise $\delta\mathcal{Q}^2 \neq 0$. Therefore, we start with an initial state that is spread out over all of the different $\mathcal{Q}$-sectors, $|\psi_0\rangle = \bigotimes_{i=1}^{L} \frac{1}{\sqrt{2}}(|\uparrow\rangle_i + |\downarrow\rangle_i)$, and run the conserving hybrid dynamics to late times to determine if the system has sharpened into a single charge sector for some measurement probability $0 \leq p_\# \leq p_c$, where $p_c \approx 0.11$ is the critical point of the entanglement transition. In this situation, the critical point of the charge

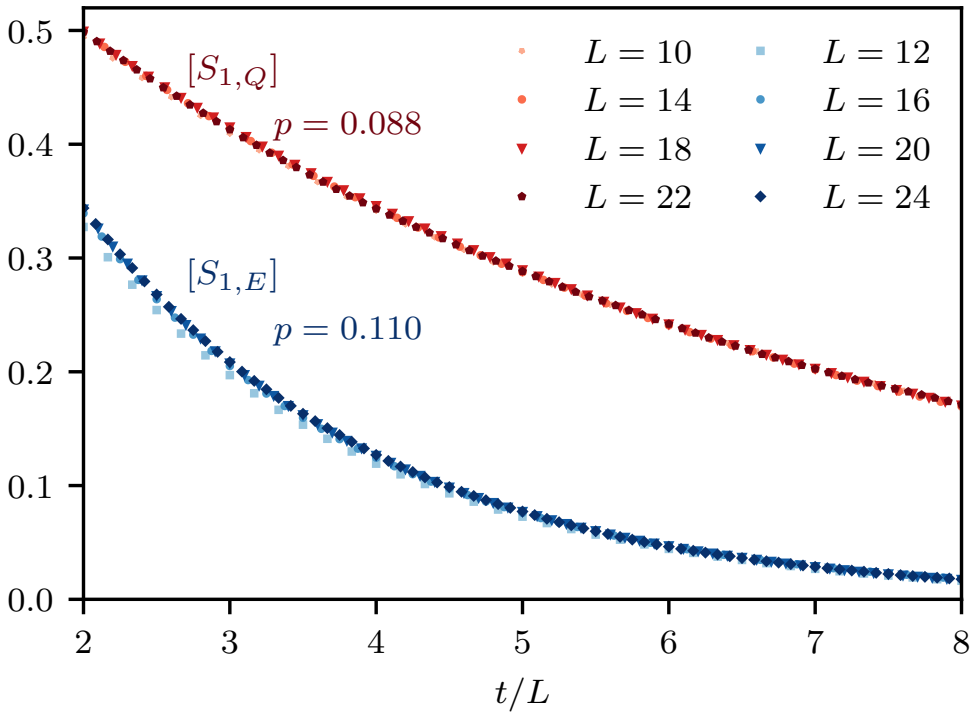

Figure 2.3. Dynamical exponent. Plot of the rescaled time-dependence of the ancilla-circuit entanglement entropy for the entanglement transition at $p = p_c \approx 0.11$ (blue curve) and the charge-sharpening transition at $p = p_{\#} \approx 0.088$ (red curve). The finite size collapse indicates a dynamical exponent $z = 1$ for both transitions.

sector transition can be determined by the studying the probability, $P(\delta\mathcal{Q}^2 = 0)$. (Recall that $\delta\mathcal{Q}^2$ is a quantum uncertainty that is a property of each trajectory; the probability distribution $P(\delta\mathcal{Q}^2)$ is over trajectories and circuits, where each trajectory is weighted by its Born probability.) For large systems, $P(\delta\mathcal{Q}^2 = 0) \to 0$ when the system is distributed over multiple sectors while $P(\delta\mathcal{Q}^2 = 0) \to 1$ when the system has been constrained to a single sector. In Fig. 2.4(a), the fraction N_0 of trajectories having a variance $x = \delta\mathcal{Q}^2 \leq s$ (with $s = 10^{-2}$) is shown for various system sizes and measurement probabilities. The critical point can be identified by the crossing near $p = 0.1$. Performing a finite size scaling analysis, we find the data for different system sizes collapses onto a universal curve for the critical point $p_{\#} = 0.094(3)$ and correlation length exponent $\nu_{\#} = 2.0(3)$.

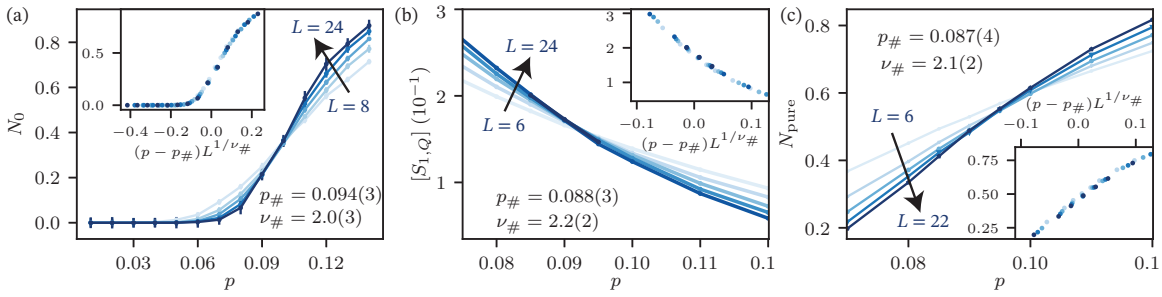

Figure 2.4. Charge sharpening transition in qubit chains. (a) Data and collapse of N_0, the fraction of trajectories with $\delta\mathcal{Q}^2 < \epsilon$ used to determine the critical point of the charge sharpening transition, $p_\# = 0.094(3)$ and correlation length exponent, $\nu_\# = 2.0(3)$. The value of $\epsilon = 10^{-2}$ and is chosen such that it maximizes the quality of collapse at $t/L = 4$. (b) Data and collapse of the entanglement transition order parameter, $[S_{1,Q}]$, used as an alternative method to determine the critical point of the entanglement transition, $p_\# = 0.088(3)$, and the correlation length exponent $\nu_\# = 2.15(15)$. (c) Data and collapse of the fraction of trajectories where the ancilla qubit is purified N_{pure} at the charge-sharpening transition. The transition point $p_\# = 0.087(4)$ and the correlation length exponent $\nu_\# = 2.1(2)$ are consistent with the ancilla probe.

Lastly, we consider an ancilla coupled to two different charge sectors, in particular we take $|\Psi\rangle = |\psi_\mathcal{Q}\rangle|0\rangle + |\psi_{\mathcal{Q}-1}\rangle|1\rangle$ where $|\psi_\mathcal{Q}\rangle$ represents states within the charge sector $\mathcal{Q}$ (while $|1\rangle$ and $|0\rangle$ are states of the ancilla as before). Since there is no unitary that mixes these sectors, we can say definitively that the reduced density matrix has the form

$$\rho_{\text{anc}} = \begin{pmatrix} |\langle\psi_\mathcal{Q}(t)|\psi_\mathcal{Q}(t)\rangle|^2 & 0 \\ 0 & |\langle\psi_{\mathcal{Q}-1}(t)|\psi_{\mathcal{Q}-1}(t)\rangle|^2 \end{pmatrix}. \tag{2.9}$$

This formulation is convenient for the numerical algorithm we have developed that conserves charge since if the ancilla were just considered an extra qubit, $|\Psi\rangle$ would be in the conserving sector M for $L+1$ qubits. Doing this, we compute the von Neumann entanglement entropy of the ancilla qubit that we denote as $S_{1,\mathcal{Q}}$, that is shown in Fig. 2.4(b). Based on the crossing in the data and the ansatz $S_{1,\mathcal{Q}} \sim g_\mathcal{Q}((p-p_\#)L^{1/\nu_\#})$ we obtain $p_\# = 0.088(3)$ and $\nu_\# = 2.2(2)$, which matches the $p_\#$ and $\nu_\#$ found by

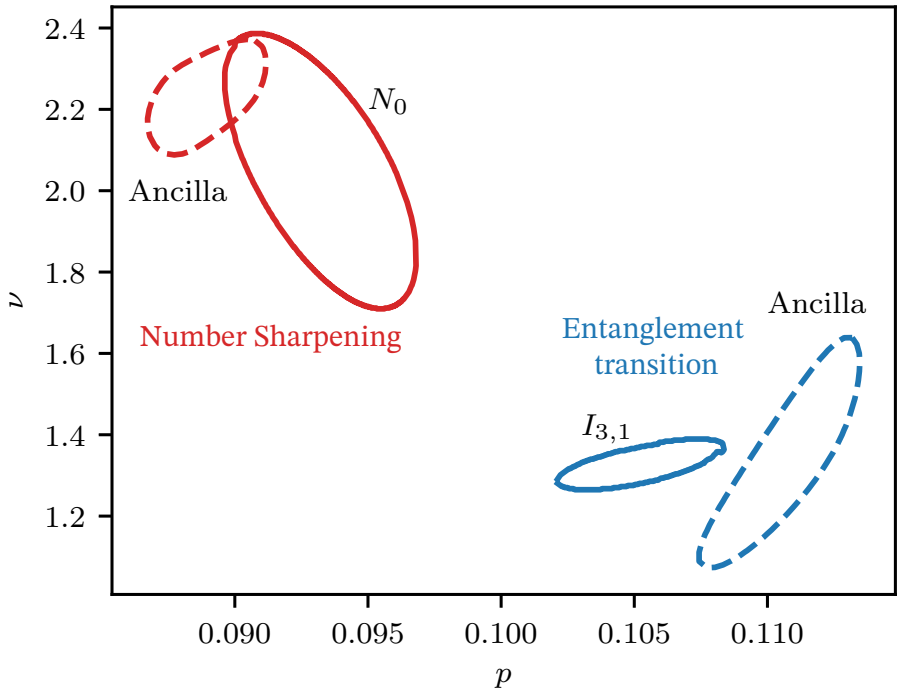

Figure 2.5. Two transitions. Plot of the 68% confidence interval of the critical point p and the correlation length exponent ν for both the entanglement and charge transitions. The mutual information $I_{3,1}$ (solid blue circle) and the ancilla probe (dashed blue circle) are for the entanglement transition, while the fraction of trajectories N_0 (solid red circle) and the ancilla probe (dashed red circle) are for the charge-sharpening phase transition. The two transitions appear to be different with statistical significance, although we cannot exclude systematic finite-size effects that would change this conclusion in the thermodynamic limit.

$P(\delta\mathcal{Q}^2 = 0)$. In addition, we extract the charge sharpening transition from the probability that the ancilla has fully disentangled from the circuit by computing the fraction of trajectories N_{pure} that have fully purified the ancilla [Fig. 2.4(c)]. From the crossing of N_{pure} we find a third consistent estimate of $p_\#$ and $\nu_\#$. Thus, we have identified the charge sharpening transition across all sectors of $\mathcal{Q}$ with the transition in $S_{1,\mathcal{Q}}$ across $\mathcal{Q} = L/2, L/2-1$. The dynamical exponent of the charge sharpening transition is also $z = 1$, as $[S_{1,\mathcal{Q}}] \sim g_{\mathcal{Q}}(t/L)$ at criticality (Fig. 2.3).

The two critical points we have identified in this model at $p_\#$ and p_c are at least ~ 3.5 error bars from each other, providing evidence that a charge sharpening tran-

sition occurs *before* full purification. This is further exemplified by the estimated confidence intervals for the two transitions for the various probes we have considered as shown in Fig. 2.5. Moreover, the correlation length exponent for charge-sharpening quantities is distinct from that of the entanglement purification transition, further suggesting that these represent distinct critical points with different universality classes.

We note, however, that the close proximity of the putative two transitions make them challenging to cleanly separate numerically in small scale systems, and acknowledge that this data could in principle be accounted for by large, systematic finite-size errors in the critical exponents that affected the charge and entanglement properties differently[5]. In the following sections, we will see that for the model with large-d qudits, the location of the two transitions become clearly distinct.

2.3 Statistical mechanics model

In this section, we show that in the $d \to \infty$ limit, the calculation of entanglement in monitored U(1) circuits can be mapped exactly onto a classical statistical model defined on a square lattice. In this limit, the contributions to the entanglement entropy from the qubit with conserving dynamics and the qudit decouple. The resulting qubit contribution can then be obtained from a constrained symmetric exclusion process.

Our main goal is to compute averaged Rényi entropies $[S_n]$. The Rényi entropies of a spatial sub-region, A, for a fixed quantum trajectory are given by

$$S_n(A, \mathbf{m}) = \frac{-1}{n-1} \left(\ln \mathrm{Tr} \left(\rho_{\mathbf{m}}^{\otimes n} T_{n,A} \right) - \ln \mathrm{Tr} \rho_{\mathbf{m}}^{\otimes n} \right), \tag{2.10}$$

[5]In the absence of a conservation law, it has been shown that the probes we have used for the entanglement transition ($\mathcal{I}_{3,n}$ and $[S_{1,E}]$) have weak finite size drifts in Clifford circuits [212] by examining small and large system sizes.

where $\rho_{\mathbf{m}} = |\psi_{\mathbf{m}}(t)\rangle \langle\psi_{\mathbf{m}}(t)|$, $|\psi_{\mathbf{m}}(t)\rangle = K_{\mathbf{m}} |\psi_0\rangle$ is the state ("trajectory") of the system after evolution by time t for a measurement history $\mathbf{m}$, and $T_{n,A}$ is a "SWAP" operator permuting the n copies of the input state in the entanglement region A:

$$T_{n,A} = \prod_i |s_{\sigma_i(1)} s_{\sigma_i(2)} \ldots s_{\sigma_i(n)}\rangle\langle s_1 s_2 \ldots s_n|$$
$$\sigma_i = \begin{cases} \text{identity} = e, & i \notin A \\ (12\ldots n), & i \in A \end{cases}, \tag{2.11}$$

where the index i runs over all physical sites, $|s_i\rangle$ are members of the onsite Hilbert space, σ_i is an element of the permutation group $\mathcal{S}_n$, and $(12\ldots n)$ denotes a cyclic permutation of the n copies of ρ. The key technical difficulty in this problem is to perform the average over gates, measurement locations and outcomes, and to normalize the state after the projective measurements since entanglement is intrinsically non-linear in the density matrix. To bypass this problem, we follow Refs. [216, 206] (see also [217, 207] in the context of random tensor networks) and introduce k replica copies of the system. The average Rényi entropy S_n is then written as:

$$[S_n] = \lim_{k\to 0} \frac{-1}{k(n-1)} \sum_{\mathbf{m}} \left(Z_A(\mathbf{m}) - Z_\emptyset(\mathbf{m})\right), \tag{2.12}$$

where

$$Z_A(\mathbf{m}) = \mathbb{E}_U \left[\mathrm{Tr}\left(\left(K_{\mathbf{m}} |\psi_0\rangle \langle\psi_0| K_{\mathbf{m}}^\dagger\right)^{\otimes nk+1} T_{n,A}^{\otimes k}\right)\right]$$
$$Z_\emptyset(\mathbf{m}) = \mathbb{E}_U \left[\mathrm{Tr}\left(\left(K_{\mathbf{m}} |\psi_0\rangle \langle\psi_0| K_{\mathbf{m}}^\dagger\right)^{\otimes nk+1}\right)\right], \tag{2.13}$$

with $T_{n,A}$ defined in (2.11), and $|\psi_0\rangle$ is the quantum state of the system at $t = 0$. As the notation suggests, $Z_{A,\emptyset}$ will correspond to the partition function of an effective statistical model, where Z_A and $Z_\emptyset$ only differ with respect to the boundary condition

at the top boundary region A (see Appendix A Fig. A.1). We will denote the total number of replicas as $Q = nk+1$ in the subsequent discussion. The additional replica is due to the Born probability factor, which ensures quantum trajectories are weighted appropriately [216]. Also note that since the original non-linear quantity has been converted to a linear quantity defined on Q copies, we are free to do various averages in any order we want.

The rest of this section is organized as follows. We start by giving a very brief overview of the statistical model for random monitored circuits without any symmetries, following Refs. [216, 206], before moving on to summarize the result for the U(1) symmetric system. We include a detailed and technical derivation of the above model in Appendix A. This technical section can be skipped without breaking any continuity.

2.3.1 Statistical model for systems without symmetry

We briefly review the mapping for random monitored circuits without symmetries to a statistical model [216, 206]. We focus on the details required for our subsequent discussion, in particular on the large dimension limit $d \to \infty$. To calculate Eq. (2.13) we need to average over Q copies of the circuit over Haar gates and measurement outcomes (but *not* over measurement locations). Since the random Haar gates are drawn independently, we can individually average Q copies of each gate. The combinatorial results of the averaging can be captured as a partition function that can be computed as follows: each unitary gate in the circuit is replaced by a vertex associated with a pair of permutation "spins" $\sigma_a, \bar{\sigma}_a$, each belonging to the permutation group $\mathcal{S}_Q$. In the $d \to \infty$ limit, these spins become locked together in a single $\mathcal{S}_Q$ degree of freedom, σ_a. Vertices from adjacent gates, i.e. those which share an input/output qubit, are connected by links. The weight associated with a vertex in the partition function is given by $V_a = 1/d^{2Q}$. The weight of the links connecting vertices with elements $\sigma_{a,b}$

is given by

$$W_{ab}[\sigma_b^{-1}\sigma_a] = \begin{cases} d^{|\sigma_b^{-1}\sigma_a|} & \text{if link (ab) is not measured} \\ d & \text{if link (ab) is measured} \end{cases}, \tag{2.14}$$

where $|\sigma_b^{-1}\sigma_a|$ is equal to the number of cycles in the cycle decomposition of $\sigma_a^{-1}\sigma_b = C_1...C_{|\sigma_b^{-1}\sigma_a|}$. Note that the above weights are symmetric under left and right multiplication by elements of $\mathcal{S}_Q$.

We see that in this $d \to \infty$ limit, spins (permutations) connected by unmeasured links are forced to be the same, whereas spins on measured links are effectively decoupled, i.e. a measurements "break" the links connecting spins, diluting the lattice. This naturally yields a picture of the purification transition in terms of *classical percolation* of clusters of aligned permutation "spins" [183, 216, 206], though of course this simple percolation picture is special to $d \to \infty$: $1/d$ fluctuations are a relevant perturbation to the percolation critical point such that finite d transitions are described by a distinct universality class from percolation [216, 218].

As we saw in Eq. (2.12), the calculation of S_n requires taking the difference between two partition functions of the model described above but with different boundary condition (see Fig. A.1); in the replica limit, this difference in partition functions becomes equivalent to a difference in free energies $F_{A,\emptyset} = -\log Z_{A,\emptyset}$ (since the partition functions approach unity in the replica limit). The boundary condition for the calculation of Z_A forces a different boundary condition in region A, and thus introduces a domain wall (DW) near the top boundary. In the limit $d \to \infty$, the DW is forced to follow a minimal cut, defined as a path cutting a minimum number of unmeasured links (assumed to be unique for simplicity [6]). This can be seen as fol-

[6] DWs are restricted by unitarity to only make certain "turns" (See [205] for details). E.g, for $p = 0$, this leads to a unique DW where the DW follows a "light cone". For $p > 0$ one can still have many degenerate paths [219].

lows: due to the boundary condition in $Z_\emptyset$, all vertex elements in $Z_\emptyset$ are equal[7], and $Z_\emptyset = d^{(1-Q)N_m}$, where N_m is the number of measured sites. Z_A would be same as $Z_\emptyset$ except for the fact that due to the DW some links contribute different weights to Z_A. More precisely, we have $Z_A = d^{(k+1-Q)\ell_{\rm DW}} Z_\emptyset$, where $\ell_{\rm DW} = \ell_{\rm DW}(\mathbf{X})$ is equal to the number of unmeasured links that the DW crosses. Since $k+1-Q = (1-n)k < 0$ for $n > 1$, the DW will follow the path that minimizes $\ell_{\rm DW}$ [8]. Using the expression of $Z_{A,\emptyset}$ in Eq. (2.12) and taking the replica limit $k \to 0$, we find $S_n = \ell_{\rm DW}(\mathbf{X}) \ln d$, which is valid for each configuration of measurement locations. Averaging over measurement locations, we have

$$[S_n] = (\mathbb{E}_{\mathbf{X}} \ell_{\rm DW}(\mathbf{X})) \ln d, \tag{2.15}$$

where $\mathbf{X}$ denotes a configuration of measurement locations (measurement outcomes and Haar gates have been averaged over to get the statistical model). In the language of the statistical model, $\mathbf{X}$ denotes a percolation configuration. $\ell_{\rm DW}$ is the length of the minimal cut from one end of the sub system A to the other end.

In the $d \to \infty$ limit, equation (2.15) is valid for any measurement probability, p [9]. For $p = 0$, there are no measured links and hence $\ell_{\rm DW} = |A|$, where $|A|$ is the length of subsystem A. In fact, $\ell_{\rm DW}$ undergoes a percolation transition at $p_c = 1/2$, where $\ell_{\rm DW}$ is extensive in $|A|$ for $p < 1/2$, and becomes $\mathcal{O}(1)$ for $p > 1/2$ [183].

---

[7] Any difference in the vertex elements will lead to the creation of DW which are suppressed as $\mathcal{O}(1/d)$ and whose contribution goes to zero as $d \to \infty$.

[8] Note that the DW permutation element $(1...n)^{\otimes k}$ has $k+1$ cycles and each cycle can follow an independent path (to the leading order) [205]. However, this subtlety will not change the final result about the minimal cut, but only leads to fluctuations contributing sub-leading logarithmic corrections (for $p > 0$).

[9] Note that this description of the $d \to \infty$ differs from that of Ref. [216]. There the measurement locations $\sum_{\mathbf{X}}$ were averaged over directly in the partition function, in an annealed way, while we chose here to keep the measurement locations as quenched disorder. Our approach predicts a minimal cut picture consistent with Ref. [183]. We leave a discussion of the validity of the replica trick in this limit to future work.

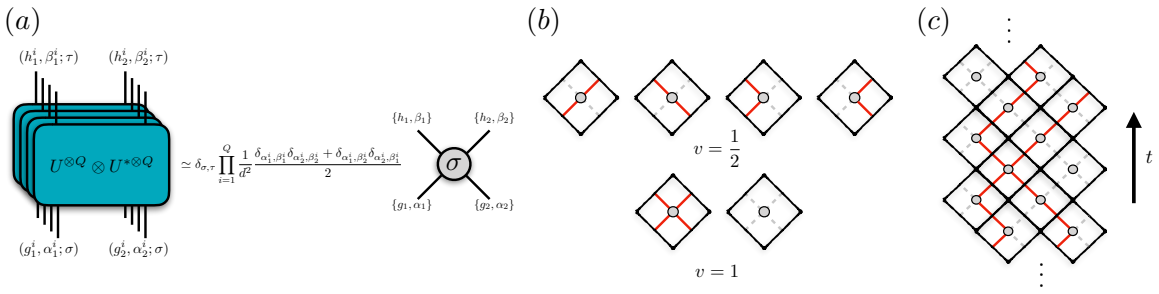

Figure 2.6. Statistical mechanics model. (a) The average of $\mathcal{U} = U^{\otimes Q} \otimes U^{*\otimes Q}$ over Haar gates is non-zero if and only if the conjugate (bra) replicas are permutations of the non-conjugate (ket) replicas. Hence we can conveniently write each leg in the circuit as a set of Q copies of non-conjugate states combined with a permutation group element (see Eq. (A.1)). In the large d limit, the permutation group elements for in-going and out-going legs become locked together in a single permutation, and the corresponding permutation group element σ can be associated with a vertex (one per gate), while the charge states live on links. The U(1) charges α, β are constrained by charge conservation. (b)The charge dynamics in each replica are given by an effective 6-vertex model with weights v, corresponding to a symmetric exclusion process constrained by the measurements and entanglement cut. (c) Example of charge configuration.

2.3.2 Statistical Model with U(1) qubits – Summary

Here we provide a concise summary of the statistical model in the case of U(1) circuits, deferring the technical details to Appendix A.

Introducing a U(1) qubit on top of each qudit modifies the above model by introducing an additional degree of freedom (per replica) α_{ij} defined on links, which can take value 0 or 1 and correspond to the charge of the U(1) qubits. The weight of each vertex is modified according to the input and output U(1) charges as follows,

$$\begin{aligned}
&(1,1) \to (1,1) \\
&(0,0) \to (0,0) \\
&(1,0) \to \frac{1}{2}\left((1,0)+(0,1)\right) \\
&(0,1) \to \frac{1}{2}\left((1,0)+(0,1)\right), \qquad (2.16)
\end{aligned}$$

where the left-hand side denotes the two input charges and the right-hand side denote output charges. The constants before the output spins are the contribution to the vertex weights. For all other configurations of charges, the weight is equal to 0 thereby enforcing charge conservation. These rules can also be seen as a special case of a 6-vertex model where the states $0, 1$ denote two species of links and the weight of the vertex depends on the configuration of the links around the vertex; see Fig. 2.6. Alternatively, those weights can be interpreted as describing hard-core random walkers (symmetric exclusion process), where each state "1" corresponds to a walker (solid link), with the number of walkers being conserved as a function of time (vertical direction in the statistical mechanics model).

We cannot directly average over the measurement outcomes of the U(1) qubits due to the non-local nature of the vertex weights. Hence, we only write a statistical model for a given set of measurement locations $\mathbf{X}$ and outcomes $\mathcal{M}(\mathbf{X})$ for the U(1) qubits; we collectively denote this set by $\mathbf{m}$, as above. The charges in the statistical model at broken links of the percolation sample are pinned by the measurement outcome of the qubit on that link. In other words, for a given configuration $\mathbf{m}$, all measured links (broken links in the percolation cluster) carry a fixed value of the local charge 0 or 1 determined by the measurement outcome of the qubit, which is fixed in $\mathbf{m}$.

The statistical model is then given by

$$Z(\mathbf{m}) = \sum_{\{\alpha\}} \prod_{i \in \text{vertices}} V_i(\{\alpha\}), \tag{2.17}$$

where the sum over $\{\alpha\}$ denotes the sum over the set of charges α on all links, V_i is the 6-vertex model weight corresponding to the rules (2.16), $\mathbf{m}$ represents a percolation configuration combined with a set of values of pinned charges on broken links, corresponding to the measurement outcomes of the qubits on those links. This statistical model has a straightforward physical interpretation: it counts histories of

the charge degrees of freedom compatible with a given set of measurement locations and measurement outcomes.

To calculate $S_n(\mathbf{m})$, we first need to find the minimal cut in the percolation configuration. Recall that ℓ_{DW} is the number of unbroken links (not measured) along the cut. There are $2^{\ell_{\mathrm{DW}}}$ different charge configurations along the cut; we denote this set of different configurations by $\{\beta_{\mathrm{DW}}\}$. From the partition function (2.17), one can straightforwardly compute the probability of finding configuration β_{DW} along the minimal cut. We denote this $p_{\beta_{\mathrm{DW}}}$. Taking the replica limit exactly (see Appendix A), we find that the Rényi entropy is given by

$$S_n(\mathbf{m}) = \frac{-1}{n-1} \ln \left(\sum_{\{\beta_{\mathrm{DW}}\}} p_{\beta_{\mathrm{DW}}}^n \right) + \ell_{\mathrm{DW}} \ln d. \tag{2.18}$$

The entropy S_n averaged over all trajectories is then given by,

$$[S_n] = \sum_{\mathbf{m}} Z(\mathbf{m}) S_n(\mathbf{m}), \tag{2.19}$$

where $Z(\mathbf{m})$ in Eq. (2.17) can be interpreted as some effective Born probability for observing the trajectory $\mathbf{m}$, where unitary gates have been averaged over. In particular, note that $\sum_{\mathbf{m}} Z(\mathbf{m}) = \mathbb{E}_{\mathbf{X}} \sum_{\{\mathcal{M}(\mathbf{X})\}} Z(\mathbf{m}) = 1$.

Note that the second term in Eq. (2.18) is the entropy of a pure qudit system. We thus interpret the first term as coming from the qubit sector and treat it as the qubits' contribution to the entanglement entropy. This first term also has an appealing physical interpretation as the classical Rényi entropy of qubit configurations along the minimal cut. This is a special feature of the $d \to \infty$ limit. From now on, we will use S_n^T to denote total entropy of the qubits and qudits in (2.18) S_n^d for the contribution to the entropy from the qudit sector alone, and $S_n = S_n^T - S_n^d$ which is equal to the first term in (2.18).

While this expression can, in principle, be computed using Monte Carlo sampling with *no sign problem*, for the one dimensional systems considered here, we find it more convenient to use a disordered transfer matrix to evolve the initial state up to some time t. Specifically, we fix $\mathbf{m}$ by randomly generating a percolation configuration, and use the vertex rules described in (2.16) to evolve the system in time. At each broken link (measured qubit) encountered in the evolution, we choose the outcome of the measurement (and hence the fixed value of the charge degree of freedom on that link) with probability equal to the Born probability. This is equivalent to a Monte Carlo sampling for the probability distribution given by $Z(\mathbf{m})$ in Eq. (2.17). Many samples are generated and for each sample we calculate the probability distribution $\{p_{\beta_{\mathrm{DW}}}\}$. Any physical quantity is then calculated as $[O] = \frac{\sum_{i=1}^{N_s} O(\mathbf{m})}{N_s}$, where N_s is the number of samples generated.

We remark that, in addition to the direct simulation of the transfer matrix techniques we employ in this work, it could also be interesting to investigate further the scaling of the transition using tensor network techniques applied to the transfer matrix of the constrained 6-vertex model [220].

2.4 Numerical results from the statistical mechanics model

In this section, we present numerical results for the U(1) statistical mechanics of constrained symmetric exclusion process described in the previous section, valid in the $d \to \infty$ limit. Unless otherwise stated, we focus on the contribution of the qubit to entanglement, and ignore the qudit contribution $\ell_{\mathrm{DW}} \ln d$ which is entirely given by classical percolation physics. We first present late time ($t \sim L$) entanglement data, and present evidence for the existence of the charge-sharpening transition occurring for $p_{\#} = 0.315 \pm 0.01 < p_c = \frac{1}{2}$. We also analyze the time dependence of the Rényi entropies, and show that they all grow linearly in time for any $p > 0$, in sharp contrast with the $p = 0$ behavior.

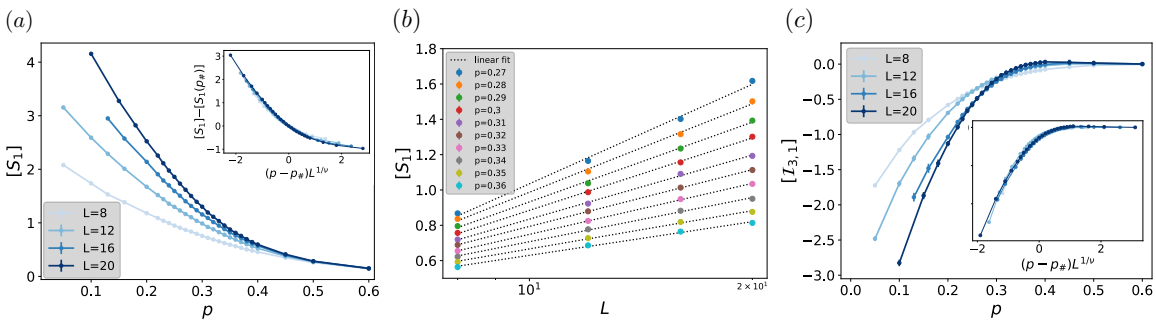

Figure 2.7. Entanglement transition in the statistical model qubit contribution. (a) Plot of the qubit entanglement entropy S_1 vs p. The *inset* shows the finite size collapse using the ansatz discussed in the main text, with $\nu \sim 1.3$ and $p_\# \approx 0.29$. (b) Plot of S_1 vs L near the critical point. We find that at the critical point S_1 grows logarithmically with L. (c) Tripartite mutual information $\mathcal{I}_{3,1}$ vs p, showing a crossing around $p_\# \approx 0.29$. The *inset* shows the finite size collapse using the same correlation length exponent as in (a).

In the statistical model, the total entanglement entropy of the subsystem A, S_n^T, depends on the minimal cut which undergoes a percolation transition at $p_c = \frac{1}{2}$; for $p < p_c$, the length of the minimal cut scales with L_A while for $p > p_c$ the measurement locations percolate and $\ell_{\rm DW}$ becomes $\mathcal{O}(1)$. Clearly the total entanglement entropy follows the area law for $p > p_c$, and is extensive (and dominated by the qudit contribution) for $p < p_c$. As discussed below (2.19), S_n^T is given by the sum of two contributions from the qudit and qubit sectors, respectively. In what follows, we will focus on the qubit contribution $S_n = S_n^T - S_n^d$, and argue that this quantity undergoes an entanglement transition from volume law to area law for $p = p_\#$. We will show that this entanglement transition from the qubit sector coincides with a charge-sharpening transition, which can also be diagnosed in a scalable way using a local ancilla probe, as in Sec. 2.2.

2.4.1 Entanglement transition in the qubit sector

In this section we look at the Rényi entropies S_n at long times, $t > 4L$ as a function of p. We consider the qubit initial state $|\psi_0\rangle = \left(\frac{|0\rangle+|1\rangle}{\sqrt{2}}\right)^{\otimes L}$. To study the behavior of

S_n for $p > 0$, we numerically run the statistical model (2.18) and calculate the half system S_n by averaging S_n over various time steps in the interval of 4 for $t > 4L$. We present results for the S_1 in Fig. 2.7.

In analogy with the non-symmetric measurement transition [183, 221], we use the following scaling ansatz for S_n

$$[S_n] - S_n^c = f(L/\xi), \tag{2.20}$$

where $\xi \sim (p - p_\#)^{-\nu_\#}$, and $S_n^c = [S_n(p_\#)] \sim \alpha_n \ln L$. Using both the entanglement entropy scaling and tripartite mutual information as in Sec. 2.2, we find that the qubit contribution shows an entanglement transition from volume-law to area law at a critical value $p_\#$ less than $p_c = 1/2$. Finite size collapses are compatible with $p_\# = 0.3 \pm 0.02$ and $\nu_\# = 1.3 \pm 0.2$. We emphasize that this entanglement transition occurs *inside* the entangling phase of the total system (the qudit contribution obeys a volume-law scaling in this regime), and occurs only as a subleading contribution to the total entanglement entropy.

From the point of view of the statistical mechanics model, this transition is especially surprising, as it indicates that the entropy (2.18) of the charge degrees of freedom along the minimal cut does not scale with its length for $p > p_\#$. Instead, our numerical results indicate that measurements are enough to constrain most charges along the cut, so the charges are almost completely "frozen" by the measurements near the minimal cut.

2.4.2 Charge-sharpening transition

Following Sec. 2.2 we probe charge-sharpening by following the dynamics of the single-trajectory charge variance $\delta\mathcal{Q}^2_{\mathbf{m}}$ starting from an initial pure state that is a superposition over charge sectors. We first discuss the average of this quantity over all trajectories. We compute this quantity using the statistical model and plot $[\delta\mathcal{Q}^2]/L$

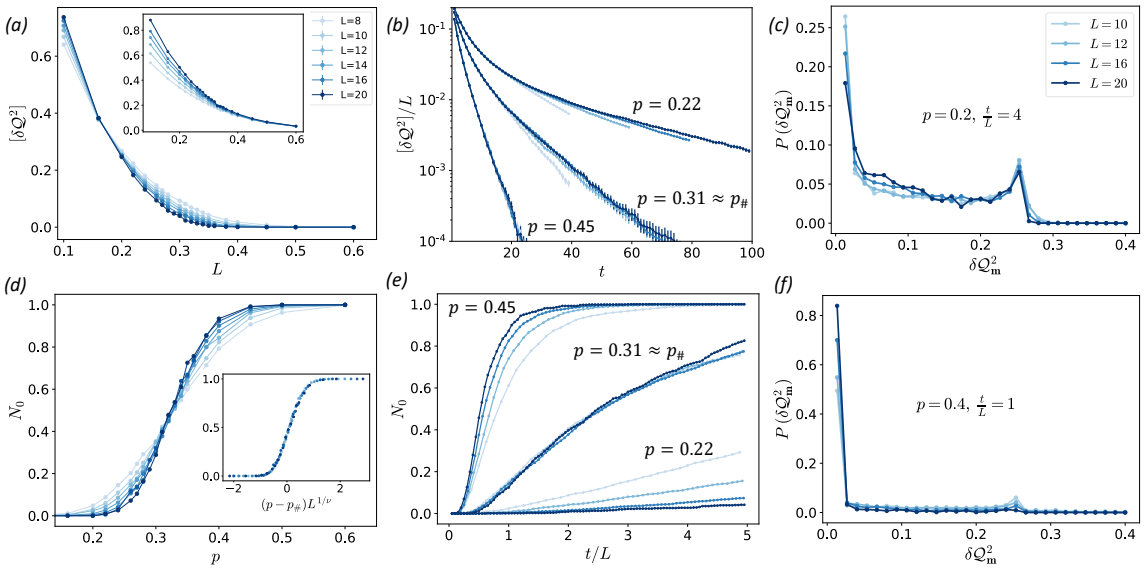

Figure 2.8. Charge-sharpening transition in the statistical mechanics model. **(a)** Plot of $[\delta\mathcal{Q}^2]$ vs p plotted for $t/L = 2$. We find that with increasing L the value of $[\delta\mathcal{Q}^2]$ approaches zero for $p > p_\# \approx 0.3$. This is consistent with the entanglement transition in the qubit sector where we observed area-law scaling for $\langle S_n \rangle$ for $p > p_\#$. Inset: charge variance in half of the system. **(b)** Charge variance $[\delta\mathcal{Q}^2]/L$ vs time t. For $p \lesssim p_\#$, $[\delta\mathcal{Q}^2]/L$ decays exponentially with a decay rate decreasing with L . For $p > p_\#$, the decay rate is same for all L suggesting that $\langle\sigma^2\rangle/L$ goes to zero faster with increasing system size (faster in units of t/L). **(c)** Histogram of the charge variance in the charge fuzzy phase. **(d)** Plot of N_0 vs p with finite size collapse in the inset. N_0 was calculated at $t/L = 2$. We find excellent collapse for $p_\# = 0.315$ and $\nu = 1.3$. **(e)** Time evolution of N_0. We clearly see a reversal in trend with system size L around $p_\# \approx 0.31$. At the transition $p = p_\#$ we find that $N_0 \sim h(t/L)$, with $h(x)$ some scaling function, consistent with a dynamical exponent $z = 1$. **(f)** Histogram of the charge variance in the charge sharp phase. The peak at 0.25 are due to trajectories with superposition of two charge sectors $\mathcal{Q}$ and $\mathcal{Q}+1$. The peak is stronger and more stable in the fuzzy phase than in the sharp phase.

as a function p in Fig. 2.8.a. We see that for $p \gtrsim p_\# \approx 0.3$, which is the threshold of the area law phase in the qubit sector, $[\delta\mathcal{Q}^2]/L$ goes to zero exponentially as a function of time in a way that is independent of L. This implies that the time scale $t_\#$ for charge sharpening for $p > p_\#$ (defined as the time it takes for the charge variance to reach a given small value ϵ) scales logarithmically with system size. In contrast, for $p < p_\#$, this charge sharpening time scales as $t_\# \sim L$ (see Appendix C.2). Fixing $t = 2L$, $[\delta\mathcal{Q}^2]/L$ behaves as an order parameter for the charge sharpening transition, coinciding with the entanglement transition in the qubit sector described in the previous section. We observe the same behavior in the bipartite charge variance.

To extract $p_\#$ it is useful to analyze a quantity that has a discontinuity at the transition. To this end, we consider N_0, the fraction of trajectories with $\delta\mathcal{Q}^2_{\mathbf{m}} < \epsilon$ for a given threshold ϵ, as in Sec. 2.2. We check that the results does not depend on ϵ for small enough values. We plot this quantity in Fig. 2.8.b and find a crossing around $p_\# = 0.31$. Note that for all L, we chose ϵ to be small enough so that N_0 counts only configurations where the charge is essentially perfectly sharp to numerical accuracy. Defined in this way, N_0 approaches 0 in the fuzzy phase, while it goes to 1 in the sharp phase. If we increase the threshold ϵ, instead, we find that N_0 behaves more like an order parameter, being fixed to $N_0 = 1$ in the sharp phase and continuously decreasing in the fuzzy phase. It is possible that that the above transition in terms of the fraction of *exactly sharp* trajectories, N_0, may be special to the case of perfectly projective measurements, as any slight weakening of the measurements would allow some non-zero quantum fluctuations of charge to persist in a finite space-time volume. Nevertheless, the transition in N_0 provides an upper bound for the "true" sharpening transition, and can, for example, establish whether the true sharpening transition resides within the volume law phase (for both qubits and qudits). We further explore these questions and the properties of the sharpening transition in the next chapter,

where we give evidence that the N_0-sharpening transition corresponds to a percolation of exactly-sharp regions that occurs within the true charge-sharp phase.

Using a scaling ansatz $N_0 = f\left((p-p_\#)L^{1/\nu_\#}\right)$, we find the best collapse for $\nu = 1.3 \pm 0.15$, consistent with the entanglement data of the qubit. We also look at the evolution of N_0 with t/L in Fig. 2.8. We find that N_0 goes to 1 for all p at long times but the rate of increase of N_0 decreases with L for $p < p_\#$ and increase with L for $p > p_\#$, while remaining constant for $p = p_\#$. We check that the exponent ν and the critical probability $p_\#$ do not vary much with the time chosen for calculating N_0 as long as it is not too large. The crossing value of N_0 tends to increase with increasing t/L: We focus here on the regime where the thermodynamic limit is taken first so t/L is "small" (in practice, $t/L = 2$ is small enough to obtain stable results). We thus conclude that the volume- to area-law transition of $[S_n]$ in the qubit sector can be interpreted as a charge sharpening transition wherein starting from a mixed superposition of all charge sectors, the measurements collapse the wave function to one charge sector for $p > p_\# = 0.315 \pm 0.01$.

2.4.3 Local ancilla probe

As in Sec. 2.2 for the qubit-only ($d = 1$) model, we now present a scalable probe of the charge-sharpening transition by entangling a reference ancilla qubit to different charge sectors $|\Psi_0\rangle = |\psi_{\mathcal{Q}}\rangle|0\rangle + |\psi_{\mathcal{Q}-1}\rangle|1\rangle$. Our numerical protocol is identical to that of Sec. 2.2 (Fig. 2.9). Those results are obtained by taking the minimal cut to be always at the link connecting the ancilla to the system: this is correct in the thermodynamic limit below the percolation threshold $p < p_c = 1/2$, and removes spurious finite size effects due to percolation physics. Our results for this quantity are qualitatively different from the $d = 1$ model of Sec. 2.2, which showed a possible crossing in that quantity, while we observe here a behavior consistent with that of an order parameter for the charge-sharpening transition. This difference might be

due to different "magnetization" exponents β, with the $d = 1$ model being closer to percolation. Analogous to the N_0 quantity defined above, we introduce N_{pure} which is equal to number of trajectories where the reference qubit is purified. We observe a crossing N_{pure} near $p_\# \approx 0.315$ and plot the finite size collapse in Fig. 2.9.

To conclude this section we compare our results for the charge sharpening transition in the two limits of $d = 1$ and $d \to \infty$. In both cases we have found Lorentz invariant critical points with $z = 1$ to within numerical accuracy. In the limit of $d \to \infty$ we have a correlation length exponent $\nu_\# = 1.3 \pm 0.15$, which is consistent with the percolation universality class that is also found in the qudit sector at $p_c = 1/2$. Whereas in the limit of $d = 1$ we have $\nu_\# \approx 2.0$, which points to a unique universality class that is distinct from both the limit of $d \to \infty$ and the entanglement transition at p_c.

2.4.4 Entanglement dynamics

Finally, we briefly turn to the dynamics of the Rényi entropies $S_n(t)$ using the statistical model. As before, S_n is the contribution of the U(1) qubits to the entanglement entropy: the total entropy S_n^T always grows linearly for $p < p_c = 1/2$ due to the qudit sector. The results below should be interpreted as sub-leading corrections to the growth of the total entanglement entropy arising due to the slow dynamics of the U(1) qubits.

In the absence of measurements, the statistical mechanics model predicts that all Rényi entropies scale diffusively $S_{n>1} \sim \sqrt{t}$, whereas $S_{n=1} \sim t$, in agreement with earlier results [191, 214, 192] (see Appendix C.1). As argued in Sec. 2.1, in the presence of measurements, the "dead regions" responsible for this unusual behavior survive only until a time $t \sim p^{-2/3}$ in typical trajectories. At long times, the overlap of the wavefunction with dead regions is zero, and we expect the trajectory-averaged Rényi entropies $[S_n]$ to grow linearly in time for all $p > 0$.

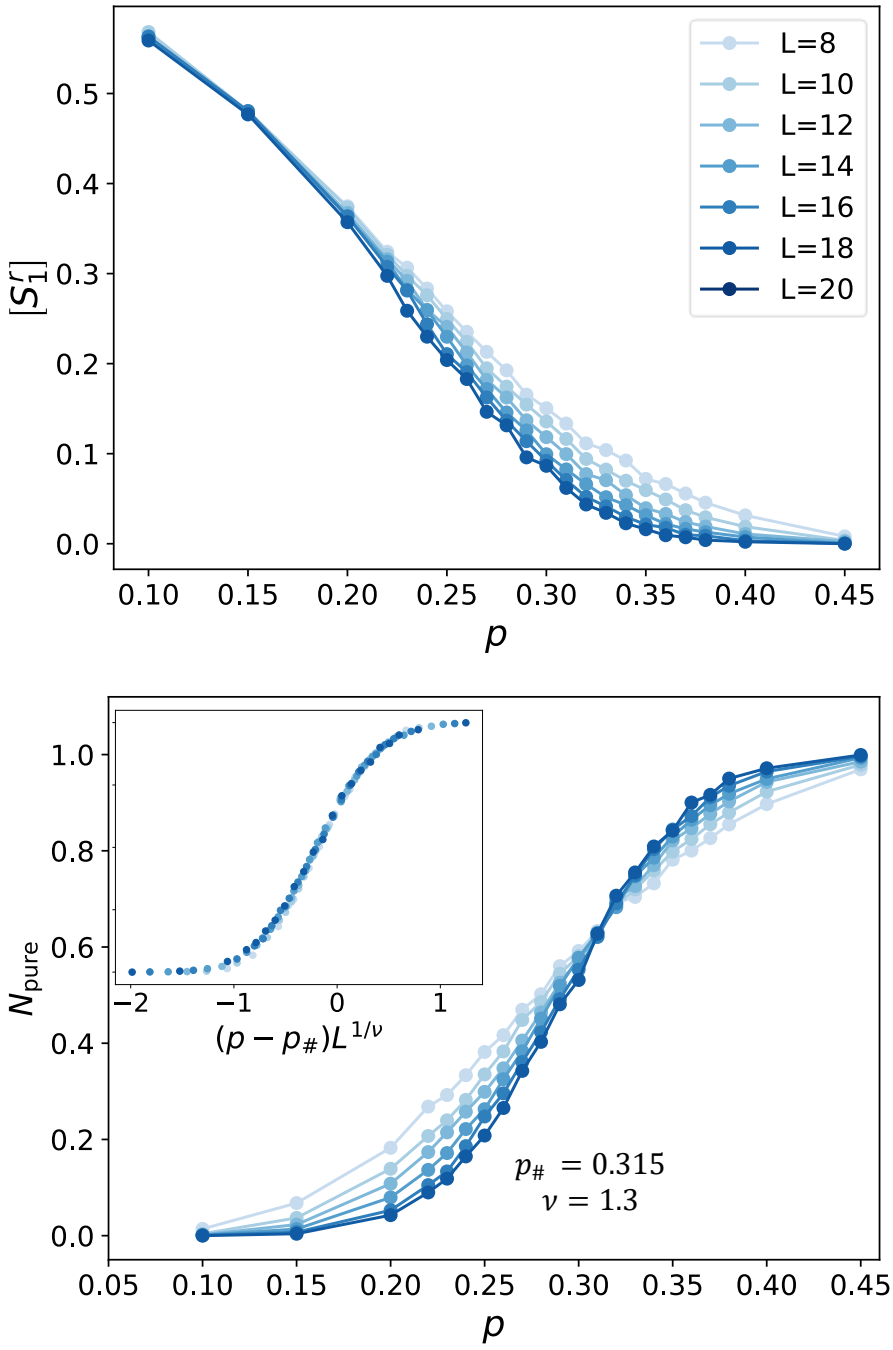

Figure 2.9. Ancilla probe in the statistical mechanics model. Top: entanglement entropy of the ancilla qubit, which behaves as an order parameter for the charge-sharpening transition. Bottom: Finite size scaling of the number of trajectories where the ancilla qubit is purified N_{pure}, probing the charge-sharpening transition.

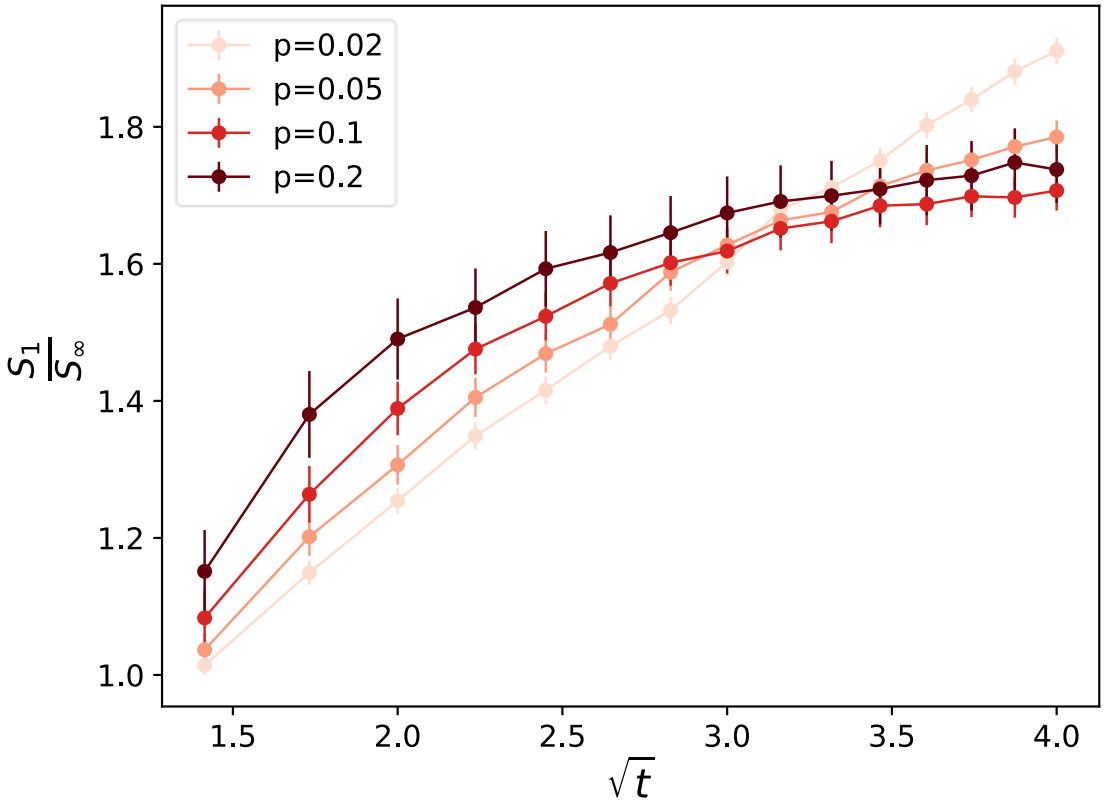

Figure 2.10. Entanglement dynamics in the statistical mechanics model. Ratio $R_s = \frac{S_1}{S_\infty}$ vs $\sqrt{t}$ for $L = 12$. We find that R_s saturates implying that S_∞ and S_1 are growing at the same rate $\sim t$. As expected, the saturation time is longer at low p.

To confirm this, we plot the ratio $R_s = [S_1]/[S_\infty]$ in Fig. 2.10. The average von Neumann entropy $[S_1]$ is expected to grow linearly for all p. The quantity R_s is thus a measure of the growth of $[S_\infty]$: if $[S_\infty]$ were to increase as $\sqrt{t}$, then we would expect R_s to grow as $\sqrt{t}$ too. This is indeed what we observe at $p = 0$. At higher p we find that R_s saturates to a constant value implying that $[S_1] \sim [S_\infty] \sim t$, in agreement with our general argument. Other observables confirming this scaling are presented in Appendix C.1.

CHAPTER 3

EFFECTIVE FIELD THEORY FOR SHARPENING TRANSITIONS

In this chapter, building on a statistical mechanics mapping developed in Chapter 2, we construct a replica field-theory framework to analytically study phases and critical phenomena in the volume-entangled regime of monitored random circuits (MRCs). We focus on the application of this technique to studying charge-sharpening transitions in more generic $1d$ MRCs with a conserved $U(1)$ charge or spin and show that this transition is captured by a modified Kosterlitz-Thouless transition. We validate this prediction against large-scale matrix-product state (MPS) numerics. This chapter is based on [222].

3.1 Statistical Model for U(1) MRC – A recap

In Section 2.3.2, we considered a model consisting of a $1d$ lattice, with a charged qubit with charge-basis states $|q = \pm 1\rangle$ and a neutral d-level qudit on each site, that evolves under a "brick wall" circuit of nearest-neighbor gates that conserve the total charge of the qubit pair, but are otherwise Haar-random in each block of fixed total charge. We consider randomly-placed single-site projective measurements with probability p. These measurements occur in the charge basis of the qubits and an arbitrary basis of the qudits. As shown in Chapter 2, this model supports two types of phase transitions (separating three distinct dynamical phases): an area-to-volume law entanglement transition at $p = p_c$ (identical to that of asymmetric circuits), and a "charge-sharpening" transition at $p = p_\#$ occurring within the volume-law entangled

phases. The charge-sharpening transition distinguishes a charge-fuzzy phase ($p < p_{\#}$) in which scrambling is able to "hide" quantum superpositions of total charge from the measurements for a time that diverges with the system size, and a charge-sharp phase ($p > p_{\#}$) in which the measurements collapse quantum superpositions of different total charge at a finite-rate. Throughout both phases the neutral qudit degrees of freedom remain volume-law entangled.

As shown in Chapter 2, the statistical properties of entanglement and charge correlators for this MRC ensemble can be captured, via a replica trick, by a classical statistical mechanics model defined on the graph of the quantum circuit (i.e. identifying gates with vertices and qubit world-lines between gates with links), and consisting of the following degrees of freedom: i) replica permutation "spins" $s_i \in S_Q$ on each vertex i where Q is the number of replica copies, and ii) charge degrees of freedom $q_{\ell,a} \in \{\pm 1\}$ on each link ℓ and replica $a = 1 \dots Q$. As previously described in multiple works [207, 205, 206, 216] the entanglement transition at p_c appears as an order/disorder transition of the permutation spins.

Here, we focus on the charge-sharpening transition that occurs in the volume-law phase where the permutation spins remain ordered, and can be traced out to obtain a description purely in terms of the charge degrees of freedom. This can be done exactly in the limit of large qudit dimension d. Since the permutation degrees of freedom are gapped for $p = p_{\#} < p_c$, we expect finite d corrections to only renormalize the parameters of the effective field theory to be derived below. The resulting charge dynamics are then described by a classical stochastic process in which charge world-lines execute hardcore random walks in each replica. Measurements force the charges to coincide across replicas at the measured link, creating a space-time-disordered inter-replica interaction.

These charge dynamics are described by a stochastic Markov process for the diagonal components of the (replicated) density matrix in the charge basis (with off-

diagonal coherences strictly vanishing due to the qudit "baths"). These form a 2^{LQ} component vector: $|\rho_Q\rangle$, which, if correctly normalized, satisfies $\langle 1|\rho_Q\rangle = \mathrm{tr}\hat{\rho_Q} = 1$ where $|1\rangle$ is the vector with all unit entries. The measurement- and gate- averaged evolution is described by a transfer matrix:

$$|\rho_Q(t+1)\rangle = T_{\boldsymbol{m}(t+1/2)} T_{U,o} T_{\boldsymbol{m}(t)} T_{U,e} |\rho_Q(t)\rangle, \tag{3.1}$$

where $T_{U,e/o} = \prod_{\langle ij\rangle \in e/o} \prod_{a=1}^{Q} \frac{1}{4}\left(\boldsymbol{\sigma}_{a,i}\cdot\boldsymbol{\sigma}_{a,j}+3\right)$ project onto the spin-triplet sector for each bond and represent the evolution from random gates on even(e)/odd(o) bonds, and $\boldsymbol{\sigma}$ are Pauli matrices with $\sigma^z_{a,i}$ eigenvalue corresponding to the charge at link $i \in \{1\dots L\}$ in replica $a \in \{1\dots Q\}$. The measurement operators: $T_{\boldsymbol{m}(t)} = \prod_{i\in\mathcal{M}(t)} \prod_{a=1}^{Q} \delta_{\sigma^z_{a,i}, m_i(t)}$ simply force the charges in all replicas to agree with the measurement outcomes $\boldsymbol{m}(t)$ on measured links $\mathcal{M}(t)$ at time-slice t.

In the following, we will not work with explicitly normalized states, and use the replica trick to properly compute moments of local observables as:

$$\begin{aligned}\mathbb{E}\left[\langle\hat{O}_1\rangle\langle\hat{O}_2\rangle\right] &= \mathbb{E}\left[\frac{\langle 1|O_1^{(d)}|\rho_1\rangle\langle 1|O_2^{(d)}|\rho_1\rangle}{\langle 1|\rho_1\rangle^2}\langle 1|\rho_1\rangle\right] \\ &= \lim_{Q\to 1}\langle 1|O_1^{(d)}\otimes O_2^{(d)}\otimes \mathbb{1}\cdots\otimes\mathbb{1}\,|\mathbb{E}\left[\rho_Q\right]\rangle\,,\end{aligned} \tag{3.2}$$

where $\mathbb{E}[\dots]$ denotes an average over trajectories, and $\langle\dots\rangle$ denotes the quantum average within a trajectory, an we define the diagonal part of a quantum operator $\hat{O}$ as $O^{(d)} = \sum_m \langle m|\hat{O}|m\rangle |m\rangle\langle m|$ where $|n\rangle$ is a basis state with definite $\hat{\sigma}^z_{a,i} = m_{a,i}$. In the first line, the factors of $\langle 1|\rho\rangle$ in the denominator serve to explicitly normalize the state, and the extra factor of $\langle 1|\rho\rangle$ in the numerator weights each measurement outcome by its Born probability.

In Chapter 2, this transfer-matrix model was analyzed explicitly using exact diagonalization (ED) methods. Here, we benchmark the field-theory predictions representing $|\rho\rangle$ as a matrix product state (MPS) using time-evolving block decimation

(TEBD) analysis of Eq. 3.1 [223, 224, 220]. We emphasize that in this statistical mechanics-description, the volume law phases of the physical qubits correspond to area-law (with log-violation for $p < p_{\#}$) phases of the statistical mechanics "spins", $\boldsymbol{\sigma}$, enabling us to obtain results on much larger systems than ED (up to ≈ 60 sites.)

3.2 Effective field theory

To gain an analytic handle on the charge dynamics, we define a continuous time version of the stroboscopic/circuit evolution of Eq. 3.1, by replacing the spin-triplet projectors in the T_U terms with a ferromagnetic interaction $\frac{1}{4}\left(\boldsymbol{\sigma}_i \cdot \boldsymbol{\sigma}_j + 3\right) \to e^{J\boldsymbol{\sigma}_i \cdot \boldsymbol{\sigma}_j dt}$, and replacing sharp projective measurements in $T_{\boldsymbol{m}}$ by Gaussian-softened "weak" measurements: $\delta_{\sigma^z_{a,i}, m_i(t)} \to \exp\left[-\frac{\gamma}{2}\sum_a \left(\sigma^z_{a,i} - m_i(t)\right)^2\right]$, where J and γ are now treated as adjustable parameters that respectively control the strength of unitary gate evolution and measurements respectively. We note that a similar strategy was used in [194] to study $\mathbb{Z}_2$-symmetric circuits with $Q = 2$ replicas. Here, we will use the large-d qudits to take the proper replica limit and recover exact scaling results.

Averaging over measurement outcomes, the transfer matrix for time t then takes the form of imaginary time with respect to a lattice Hamiltonian: $T(t) = e^{-tH}$ with:

$$H = -J \sum_{\langle i,j\rangle;a} \boldsymbol{\sigma}_{a,i} \cdot \boldsymbol{\sigma}_{a,j} + \frac{\gamma}{2} \sum_{i;a,b} \sigma^z_{a,i} \Pi_{ab} \sigma^z_{b,i}, \tag{3.3}$$

where $\Pi_{ab} = \left(\delta_{ab} - \frac{1}{Q}\right)$ is a projector onto replica-asymmetric modes.

Without measurements ($\gamma = 0$), the random circuit dynamics simply takes the form of imaginary time evolution with $SU(2)$ invariant Heisenberg ferromagnet dynamics. The long-time steady states (ground-states of H) are simply equal weight superpositions over all charge configurations with each fixed total charge. The elementary excitations of $H_{\gamma=0}$ (corresponding to decaying perturbations to the steady-state) are magnon excitations with dispersion (wave-vector dependent decay rate)

$\varepsilon_k \sim Jk^2$. These simply reflect the diffusive relaxation dynamics of conserved charges. Measurements penalize differences in σ^z between different replicas. After averaging over the space-time quenched disorder due to measurement locations and outcomes, this introduces inter-replica interactions and produces an easy-plane anisotropy for the inter-replica modes.

We next construct an effective field theory by writing $T(t)$ as a spin-coherent state path integral in terms of polar angles $\theta_{i,a}$ and azimuthal angles $\phi_{i,a}$ for each spin which leads to following Lagrangian

$$L = -\frac{i}{2}\sum_{a,i}\cos\theta_{a,i}\partial_\tau\phi_{a,i} - J\sum_{\langle i,j\rangle,a}\left[\cos\theta_{a,i}\cos\theta_{a,j} + \sin\theta_{a,i}\sin\theta_{a,j}\cos\left(\phi_{a,i}-\phi_{a,j}\right)\right] \tag{3.4}$$

For specificity, we work near zero charge density $\theta = \pi/2 + \delta\theta$. Then, expanding in small fluctuations around this mean value $\delta\theta = \theta - \theta_0$, and in the azimuthal angle $\phi_i - \phi_j \approx \hat{e}_{ij}\cdot\nabla\phi$ where $\hat{e}_{ij}$ is a unit vector along link ij, and converting lattice sums into continuous integrals over space gives Lagrangian density:

$$\mathcal{L} \approx i\frac{1}{2}\sum_a \delta\theta_{a,i}\partial_\tau\phi_a + \frac{J}{2}\sum_{i,a}\left[\left(\partial_x\delta\theta_a\right)^2 + \left(\partial_x\phi_{a,i}\right)^2\right] + \frac{\gamma}{2}\sum \delta\theta_a\Pi_{a,b}\delta\theta_b \tag{3.5}$$

Integrating out all $(Q-1)$ components of the out-of-plane fluctuations in the inter-replica modes, $\Pi\theta$, which are massive for any $\gamma > 0$, and performing a fluctuation and gradient expansion gives an effective action $\langle 1|T(t)|\rho_Q\rangle = \mathcal{Z}_Q = \int D[\theta,\phi]e^{-\int_0^t dt\int dx\mathcal{L}_{\text{eff}}}$ with:

$$\mathcal{L}_{\text{eff}} = \frac{i}{2}\delta\bar{\theta}\partial_t\bar{\phi} + \frac{\bar{\rho}}{2}\left[\left(\partial_x\delta\bar{\theta}\right)^2 + \left(\partial_x\bar{\phi}\right)^2\right] + \frac{\rho_s}{2}\left(\partial_\mu\Pi\phi\right)^2, \tag{3.6}$$

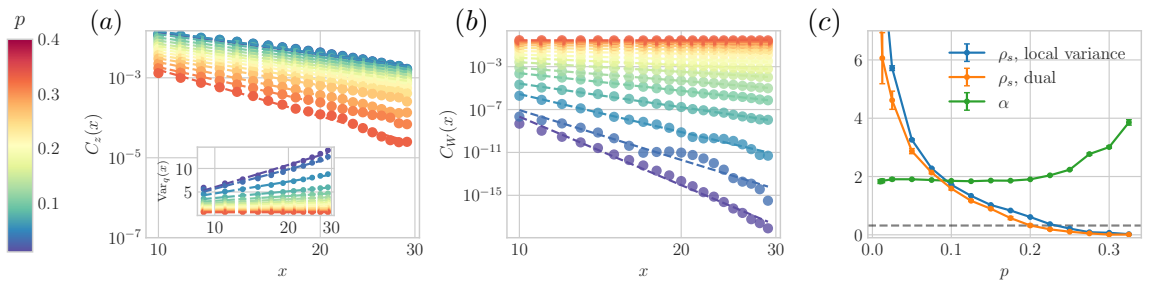

Figure 3.1. TEBD data – (a) Charge fluctuations $C_z(x) = \mathbb{E}\left[\langle\sigma_x^z\sigma_0^z\rangle - \langle\sigma_x^z\rangle\langle\sigma_0^z\rangle\right]$, scaling as $C_z(x) \sim x^{-\alpha}$ in the fuzzy phase. Inset: charge variance of an interval of size x , $\mathrm{Var}_q(x) = \sum_{0<i,j<x} \mathbb{E}\left[\langle\sigma_i^z\sigma_j^z\rangle_c\right]$, predicted to scale as $\sim \frac{8\rho_s}{\pi}\log x$. (b) Dual string disorder parameter $C_W(x) = \mathbb{E}\left[\langle W_{[0,x]}\rangle^2\right]$ with $W_{[0,x]} = \prod_{0<i<x}\sigma_i^z$, showing power-law decay $C_W(x) \sim x^{-2\pi\rho_s}$ in the charge-fuzzy phase. (c) Continuously evolving superfluid density ρ_s as a function of p, extracted from the local charge variance (blue) and the dual correlator $C_W(x)$ (orange). The dashed horizontal line indicates the critical threshold $(\rho_s)_{\#} = \pi^{-1}$. For $p < p_{\#} \sim 0.2$, the charge correlator $C_z(x)$ decays with an exponent $\alpha = 2$ (green).

where $\mu \in \{t, x\}$, and repeated indices are implicitly summed, $\bar{\rho} \sim J$, $\rho_s \sim \sqrt{J/\gamma}$, and we have defined the replica average modes: $\bar{\phi}, \bar{\theta} \equiv \frac{1}{Q}\sum_{a=1}^{Q}\phi_a, \theta_a$ [1]. We have ignored higher order derivative terms like $(\nabla\delta\theta)^2(\nabla\phi)^2$. To compute correlators as in Eq. 3.2, this action should be supplemented by boundary conditions corresponding to the final state $\langle 1|$ which is an equal weight superposition of all charge states, corresponding to a product state of spins point along the $\hat{x}$ direction: $(\theta, \phi) = (\frac{\pi}{2}, 0)$ at the final time, t. In particular, steady-state ($t \sim L \to \infty$) correlators are generated from the partition function on the half- plane $(t, x) \in (-\infty, 0] \times \mathbb{R}$ with boundary conditions $\phi_a(t = 0, x) = 0$ and appropriate (charge-diagonal) operators inserted. As a consequence, steady-state properties of MIPTs will correspond to *boundary-critical properties* of the statistical mechanics problem.

[1] More generally, ρ_s depends on the space-time local charge density. But this coupling is RG-irrelevant in 1+1d so we drop it here, although it can become relevant in higher d, as we discuss later.

The "replica-average" modes $\bar{\phi}$ determine simple linear observable averages, $\bar{O} = \mathbb{E}[\langle \hat{O} \rangle]$. These are unaffected by measurements and have a simple FM spin-wave action and converge to tr $\hat{O}$ at late times independent of γ. This accords with the well-known fact that MIPTs are only visible in higher-moments and non-linear functions of state.

The inter-replica fluctuations, $\Pi\phi$, control disconnected moments of correlation functions such as $\mathbb{E}\left[\langle O(x)O(0)\rangle - \langle O(x)\rangle\langle O(0)\rangle\right]$. When singular vortex configurations in the phase-fields are irrelevant ($0 < \gamma < \gamma_{\#}$) the inter-replica modes follow a superfluid action with $(Q-1)$ decoupled relativistic Goldstone-mode excitations which indicate that charge fluctuations with wave-vector k decay at rate $\sim |k|$ (dynamical exponent $z = 1$). This inter-replica-superfluid (IRSF) phase represents the charge-fuzzy phase ($0 < p \leq p_{\#}$ in the circuit model). Since the effective "superfluid stiffness" ρ_s decreases monotonically with increasing measurement strength, γ, it is natural to expect that the charge-sharpening transition in 1+1d is a Kosterlitz-Thouless (KT)-type transition where vortex-proliferation destroys the IRSF QLRO for $p > p_{\#}$, i.e. $\gamma > \gamma_{\#}$, resulting in a "Mott insulating" phase. This picture will turn out to be qualitatively correct, albeit with important quantitative changes to the usual KT transition due to the replica structure.

3.3 Charge-sharpening in 1+1d

To obtain a controlled theory of the transition, we introduce vortex defects into Eq. 3.6 by standard duality methods [225] to obtain modified "sine-Gordon" model:

$$\begin{aligned}\mathcal{L}_{\text{dual}} =& \frac{1}{8\pi^2\bar{\rho}}\left[\left(\partial_t\bar{\vartheta}\right)^2 + D^2\left(\partial_x^2\bar{\vartheta}\right)^2\right] + \\ &+ \frac{1}{8\pi^2\rho_s}(\Pi\partial_\mu\vartheta)^2 - \lambda\sum_{a\neq b}\cos(\vartheta_a - \vartheta_b),\end{aligned} \tag{3.7}$$

where $D \sim J$, $e^{-i\vartheta_a}$ inserts a (spacetime/instanton) vortex, and ϑ are related to the original fields by $\rho_s\partial_\mu\phi_a \leftrightarrow \frac{\epsilon^{\mu\nu}}{2\pi}\partial_\nu\vartheta_a$, $\lambda \approx e^{-\sqrt{J/\gamma}}$ is the vortex fugacity, and we have

kept only the most relevant vortex terms. Note that the minimal topological defects that can appear are actually a bound states of a vortex and anti-vortex in different replicas. Formally, this is because individual vortices, which contribute vorticity to $\bar{\phi}$, are linearly confined by the diffusive replica-average mode. Intuitively, this simply reflects the absence of quantum fluctuations in the Heisenberg ferromagnet ground-state that describes replica-averages in the steady-state. An immediate consequence of this vortex-"doubling" is that it *halves* the critical superfluid stiffness compared to the ordinary KT transition: $(\rho_s)_{\#} = \pi^{-1} = \frac{1}{2}(\rho_s)_{\mathrm{KT}}$. We further note, that in an ordinary superfluid, vortex condensation requires commensuration between particle density and the lattice, otherwise vortex instantons acquire non-trivial Berry phases and are suppressed. Here, the density conjugate to the composite vortex operators are inter-replica density fluctuations, which has vanishing average independent of the physical (replica-average) charge density. Consequently, in 1+1d, there is a single universality class for charge-sharpening, in contrast to the ordinary superfluid-Mott transition which arises only at integer densities and exhibits different scalings in the presence or absence of particle-hole symmetry.

Observables and numerics In 1+1d, the fuzzy-phase/IRSF exhibits only quasi-long-range order (QLRO), with algebraic decay of charge ($\sigma^z \approx \frac{1}{\pi}\partial_x\vartheta$) correlators, $C_z(x) = \mathbb{E}\left[\langle\sigma^z(x)\sigma^z(0)\rangle - \langle\sigma^z(x)\rangle\langle\sigma^z(0)\rangle\right]$, which are negative at large distance in the steady state. This changes to short-range correlations in the gapped phase:

$$C_z(x) \sim -\begin{cases} \rho_s(a/x)^{-2} & p \le p_{\#} \\ e^{-x/\xi} & p > p_{\#} \end{cases} + \dots \tag{3.8}$$

where a is a non-universal UV cutoff (lattice spacing), ξ is a finite correlation length and $(\dots)$ denote asymptotically subleading terms. This behavior is consistent in TEBD results for the discrete-time model Eq. 3.1 showing an algebraic decay of

$\mathbb{E}[\langle\sigma^z(x)\sigma^z(0)\rangle_c]$ with power-law fit that is constant over an extended range $0 < p < p_\# \approx 0.2$ (Fig. 3.1a,c).

A hallmark of KT-physics is that certain correlators exhibit continuously evolving critical exponents in the QLRO Goldstone-phase. Constraining ourselves to charge-diagonal quantities that can be physically probed in the original qubit language, a convenient observable that displays this behavior are the string operators: $W_{[0,x]} = e^{-i\pi\sum_{i\in(0,x)}\sigma_i^z/2} \approx e^{-i\frac{1}{2}\int_0^x d\vartheta} = e^{-i\vartheta(x)/2}e^{i\vartheta(0)/2}$, which inserts a π-phase twist in the ϕ-fields in the interval $[0, x]$, and can be thought of as a dual (boundary) order parameter for vortex condensation:

$$C_W(x) = \mathbb{E}\left[\langle W_{[0,x]}\rangle^2\right] \approx \begin{cases} |x|^{-2\pi\rho_s} & p \leq p_\# \\ \text{constant} & p > p_\# \end{cases}. \tag{3.9}$$

The scaling dimension of W decreases monotonically with measurement rate γ (as $\sim \gamma^{-1/2}$ for small γ), and jumps (for $L \to \infty$) discontinously to 0 in the charge-sharp phase ($\gamma > \gamma_\#$), achieving a minimum non-zero value of $\Delta_W = 1$ at the sharpening transition ($\gamma = \gamma_\#$).

The predicted power-law decay of charge- and string- correlators are in excellent agreement with TEBD data (Fig. 3.1) for $0 < p \leq p_\# \approx 0.2$. We note that, as is typical for two-parameter scaling KT-transitions, incorrectly applying a single-parameter scaling analysis with finite correlation-length exponent, ν as in Chapter 2 dramatically overestimates the critical measurement strength, and misses the key physics of continuously evolving scaling exponents in the charge-fuzzy phase.

3.4 Modified percolation for charge degree of freedoms

In this section we argue that for large Hilbert space dimension for the qudits, the sharpening transition must occur inside the volume law phase in any spatial dimension d. The basic idea is that charge conservation induces correlations between

measurement outcomes, and allows multiple measurements to extract more information about charge than they could about neutral degrees of freedom. A measured site is charge sharp in the sense that the projective measurements will collapse the charge to either -1 or $+1$. In addition to this, charge conservation can dictate the charge of an unmeasured site based on the outcome of nearby measurements. For example, measuring three out of four legs of a gate determines the charge at the fourth. Figure 3.2 shows various related scenarios where unmeasured sites become sharp. Thus we expect charge sharp sites to start percolating at a smaller value $p_{\#p}$ compared to that for the percolation of measured sites; that is $p_{\#p} < p_c$ where p_c is the percolation transition of the measured links. In the limit we are working in in this paper (Hilbert space dimension $\to \infty$), the entanglement transition coincides with the percolation transition for the measured links. Thus, the percolation of the charge sharp sites happens inside the volume law phase. The presence of the percolation transition for charge sharp sites implies that a sharpening transition must happen at value $p_{\#} \leq p_{\#p}$. In other words, the sharpening transition must happen inside the volume law phase. Note that this result is true for any dimension. Thus, we have the result that the sharpening transition, in all dimensions, must occur *inside* the volume law phase, well separated from the entanglement transition.

To numerically study this modified percolation in $1+1$ dimension, we entangle the charge at every space-time point to a ancilla qubit. A site at (x, t) is then charge sharp iff the corresponding ancilla at (x, t) becomes charge sharp. (Note that the ancilla becoming charge sharp is a stronger condition than the ancilla getting disentangled from the system. In general the ancilla might become disentangled without becoming sharp.) This allows us to determine space time points with sharp charge. A standard percolation analysis then shows that the sharp sites start percolating at $p_{\#p} \approx 0.31$ which is much less than the percolation transition for the measured sites at $p_c = 0.5$. Figure 3.2 shows the probability for sharp sites to percolate along spatial direction.

These curves show a clear crossing with increasing system size at $p_{\#p}$, and collapse upon rescaling with the standard percolation form with correlation exponent $\nu = 4/3$.

We emphasize that this percolation of charge-sharp sites does not reflect the true charge sharpening transition that occurs at a smaller measurement value, $p_{\#} \approx 0.2$, and has $\nu = \infty$ KT-like scaling rather than percolation scaling. In fact we conjecture that this sharp-site percolation transition may not be visible in any physical degrees of freedom for generic models where measurements are not perfectly projective (as this blurs the distinction between sharp and unsharp sites). However, the sharp-site percolation threshold clearly upper-bounds the critical measurement probability for sharpening: $p_c > p_{\#p} \geq p_{\#}$ in the projective measurement limit, supports the argument that the charge-sharpening transition generically occurs in the volume-law entangled phase. We also note that the charge-sharpening transition identified as

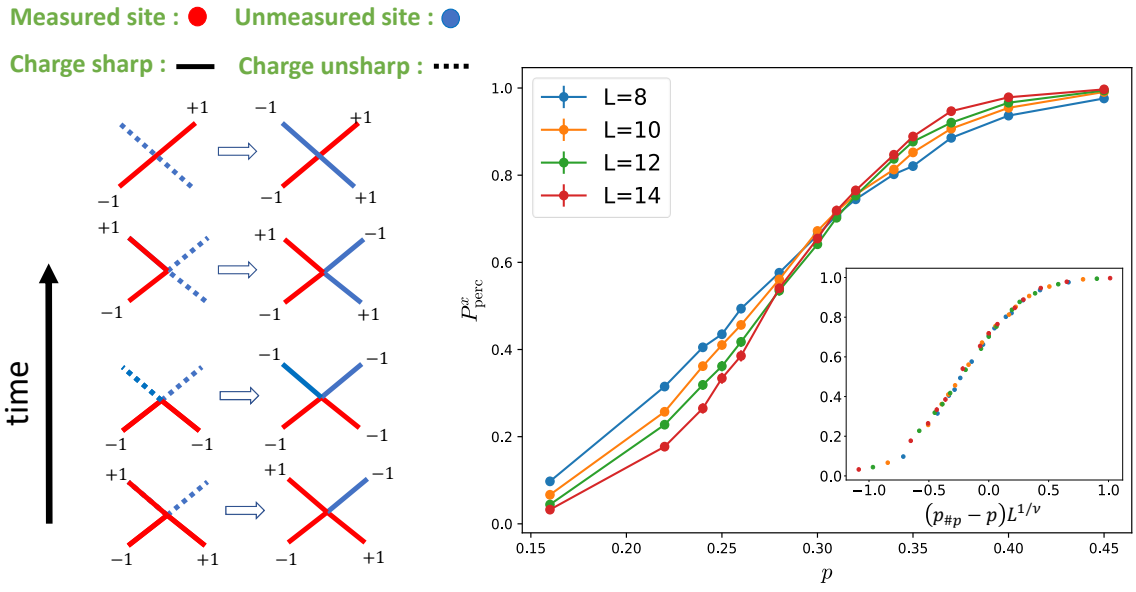

Figure 3.2. *Left.* Illustration of some ways in which unmeasured sites become charge sharp. Other scenarios can be obtained similarly. The bold links percolate at around $p_{\#p} \approx 0.31$ and red links percolate at $p_c = 0.5$. *Right.* Probability for a cluster of charge sharp sites to wrap around the spatial direction vs p. The inset shows collapse with $p_{\#p} = 0.31$ and $\nu = 4/3$.

a finite-size crossing in the fraction, N_0 of exactly-charge-sharp trajectories in the previous chapter occurs at $p \approx p_{\#p}$, and may be probing this auxiliary critical point rather than the true charge-sharpening transition at $p_\# \approx 0.2$ (an issue exacerbated by the strong finite-size corrections to scaling near KT transitions).

CHAPTER 4

CONCLUSION

In this section, we have studied measurement-induced phases and phase transitions in monitored quantum circuits with charge conservation. We argued that measurements can have a dramatic effect on entanglement growth. While all Rényi entropies with index $n > 1$ grow diffusively in the absence of measurements, for any $p > 0$, the effect of these rare regions are washed out by measurements leading to ballistic scaling $S_n \sim t$ at long times.

Whereas, in the absence of symmetry, there can only be two possible steady-states, entangling or purifying, charge conservation enriches this dynamical phase diagram. We uncovered a new type of charge-sharpening transition that separates distinct entangling phases. Even as the dynamics remain scrambling and lead to a volume-law entangled state, the U(1) charge can either be "fuzzy" or "sharp" depending on the rate of measurements. This charge-sharpening transition occurs at a critical measurement rate $p_\#$ that is generically smaller than p_c, corresponding to the purification transition. This new transition is also fundamentally different from the purification entanglement transition, as for any $p > 0$, the charge will eventually become sharp with exponentially small corrections for $t \gg t_\# \sim L$ (up to logarithmic corrections) for a system of size L, whereas the purification time diverges exponentially in the system size in the entangling phases. The sharpening time scale for U(1) circuits is also parametrically much faster than that in $\mathbb{Z}_2$ symmetric circuits [194] (linear vs exponential), highlighting the fundamental difference between scrambling of U(1) and $\mathbb{Z}_2$ symmetric modes. Thus the measurement-induced phases inside the

volume law for U(1) systems are conceptually very different than those in $\mathbb{Z}_2$ symmetric systems [194]. The type of sharpening transitions studied here are unique to systems with diffusive modes.

We presented evidence for the existence of this transition using both exact numerical results in a symmetric qubit model ($d = 1$), and from the numerical analysis of an emergent statistical mechanics model describing the evolution of charged qubits coupled to large qudits ($d \to \infty$). For the model in the $d \to \infty$ limit, the correlation length exponent ν of the charge-sharpening transition is consistent with that of percolation. In contrast, in the qubit-only model we showed that the charge-sharpening correlation length exponent is distinct from the that found for the entanglement transition with $\nu_{\#} \approx 2$. Understanding the critical properties of this transition represents a clear challenge for future works. A conceivable scenario could be that the charge-sharpening and entanglement transitions could merge into a single transition below a critical qudit dimension, $d < d_c$. Establishing on firmer grounds the existence of a distinct charge-sharpening transition would also be an important task for future works.

The statistical mechanics model is also an important step in the understanding of symmetric monitored circuits. We were able to take the replica limit analytically which is a crucial step to uncover key properties of measurement-induced phase transitions and is often the most daunting challenge in the studies of monitored circuits [194]. We find that the contribution of the U(1) degrees of freedoms to the Renyi entropies is related to the entropy of local charge fluctuations along the minimal cut (eq. (2.18)). Though this mapping is restricted to the $d \to \infty$ limit, since the permutation degrees of freedom are gapped in the volume-law phase we do not expect them to change the general structure of the phase diagram or the universality class of the sharpening transition for finite d. The stat mech approach can also be

readily generalized to arbitrary Abelian symmetries (Appendix B) thus providing a controlled platform for future studies of symmetric circuits, for example $\mathbb{Z}_n$ circuits.

We also studied the effective field theory of the classical stat mech model which predicts that the local sharpening transition is in a Kosterlitz-Thouless universality class (KT). In this picture, the fuzzy phase corresponds to the quasi-long range order and the charge sharp phase is the symmetric phase. A proper analysis of the replica limit is however crucial to uncover the peculiar nature of this transition, including the dynamical properties distinguishing the phases – see 3.1. It would be interesting to look for signatures of such KT scaling in the qubit model ($d = 1$), even though KT criticality is notoriously hard to study in finite size numerics.

The conservation law has not affected the universality class of the entanglement transition in the limit of $d \to \infty$. Whereas, in the limit of $d = 1$ we have shown that the log-scaling of the Renyi entropy at criticality $S_n \sim \alpha(n) \log L$, has an $\alpha(n)$ that is clearly distinct from the transition with Haar random gates [212], which implies the (boundary) universality class is distinct in the presence of a conservation law. Interestingly, we have found that $\nu \approx 1.3$, which is not sensitive enough to discern between percolation, stabilizer dynamics, and the Haar universality class. It will be interesting in future work to probe other critical exponents of the entanglement transition with a conservation law to discern other uniques properties of this transition.

It would also be interesting to extend our results to other symmetry groups or kinetic constraints. Our results can be readily generalized to arbitrary Abelian groups (see Appendix B). Moreover, it is clear by now that new types of dynamical phases can be obtained in the steady state of monitored quantum circuits, from the combination of different competing (non-commuting) measurements and unitary dynamics [226, 227, 228, 229]. The full phase structure allowed by the microscopic symmetry group and the dynamical symmetries of such monitored quantum circuit appears to be particularly rich [194], and remains largely unexplored. We expect non-Abelian sym-

metries to be especially interesting, as they could lead to fundamental constraints on the entanglement structure of the steady-state, as in the case of many-body localized systems [230].

APPENDIX A

MAPPING TO THE STATISTICAL MODEL WITH U(1) QUBITS

In this appendix, we present a in detail discussion of the mapping to the statistical model, and derive Eq. (2.18) in the limit $d \to \infty$. To evaluate the quantities in Eq. (2.13), we need to calculate the average of $\mathcal{K} \equiv K_{\mathbf{m}}^{\otimes Q} \otimes K_{\mathbf{m}}^{\dagger \otimes Q}$, corresponding to Q copies of the random circuit. Each unitary gate in $\mathcal{K}$ is repeated Q times and since they are drawn independently we can individually average them over the random unitary ensemble. Let us denote the tensor product of Q copies of a gate by $\mathcal{U} \equiv U^{\otimes Q} \otimes U^{\dagger \otimes Q}$. We view $\mathcal{U}$ as a super-operator which acts on two sites with each leg containing Q ket states and Q bra states; let $|g^i \alpha^i\rangle \langle g^{i*} \alpha^{i*}|$ be a basis where g^i is a basis of the qudit Hilbert space $\mathbb{C}^d$, and α^i is the computational basis for the qubit. The index i labels replicas, and runs from 1 to Q. Using standard Haar calculus and Weingarten formulas, we find that the action of $\overline{\mathcal{U}}$ on the above basis is non trivial after averaging if and only if $g^{i*} = g^{\sigma(i)}$ and $\alpha^{i*} = \alpha^{\sigma(i)}$, where $\sigma \in \mathcal{S}_Q$ is a permutation. Therefore, we introduce a shorthand notation for writing the relevant members of the basis as

$$(g^i \alpha^i; \sigma) \equiv \left|g^i \alpha^i\right\rangle \langle g^{\sigma(i)} \alpha^{\sigma(i)}|. \tag{A.1}$$

More precisely, each unitary gate in the circuit is replaced by a vertex associated with a pair (corresponding to in- and out-going legs) of permutation "spins" $\sigma, \bar{\sigma}$, each belonging to the permutation group $\mathcal{S}_Q$. In the $d \to \infty$ limit, these spins become locked together in a single permutation degree of freedom, σ_a, that we associate with

that vertex. Vertices from adjacent gates, i.e. those which share an input/output qubit and qudits, are connected by links in a way that will be explained below. In the large d limit, the weight associated with a vertex in the partition function is given by $V_a = 1/D^Q$, where D is the size of the block of the relevant symmetry sector. We have $D = d^2$ if all incoming and outgoing charges are the same, and $D = 2d^2$ otherwise, see eq. (2.2).

The results for $\overline{\mathcal{U}}$ to leading orders are summarized in Fig. 2.6; the sub-leading corrections are suppressed as $\mathcal{O}(1/d^2)$ which we will ignore in rest of the paper. The factor of $\frac{\delta_{\alpha_1^i\beta_1^i}\delta_{\alpha_2^i\beta_2^i}+\delta_{\alpha_1^i\beta_2^i}\delta_{\alpha_2^i\beta_1^i}}{2}$ in Fig. 2.6 enforces U(1) charge conservation, and follows from the size of the different blocks in eq. (2.2). In fact, if we view charge 0 as vacuum and charge 1 as a particle, then the dynamics of the U(1) degree of freedom can be understood as a hard core random walk these particles, known as the symmetric exclusion process. Alternatively, it can be seen as a special case of the 6-vertex model (see Fig. 2.6.b). Though we have focused mainly on the case of U(1) symmetry groups, our approach readily extends to other Abelian groups. In Appendix B we provide a general derivation for arbitrary Abelian symmetry groups.

A.1 Link weights

Combining Fig. 2.6 with the brick wall geometry of the circuit leads to a model described on a square lattice as shown in Fig. A.1. Each vertex has an element from the permutation group $\mathcal{S}_Q$ and each link has Q copies of the elements of the basis of the local Hilbert space. The vertex weights V_a are given by the rule described in Fig. 2.6.b. The link weight W_{ab} has two kind of contributions: 1) due to the presence of domain wall (DW) in the permutation group elements $\sigma_{a,b}$ (DW constraint), 2) the state at the link $\langle ab\rangle$ is being measured (measurement constraint). We describe these constraints in detail in the following.

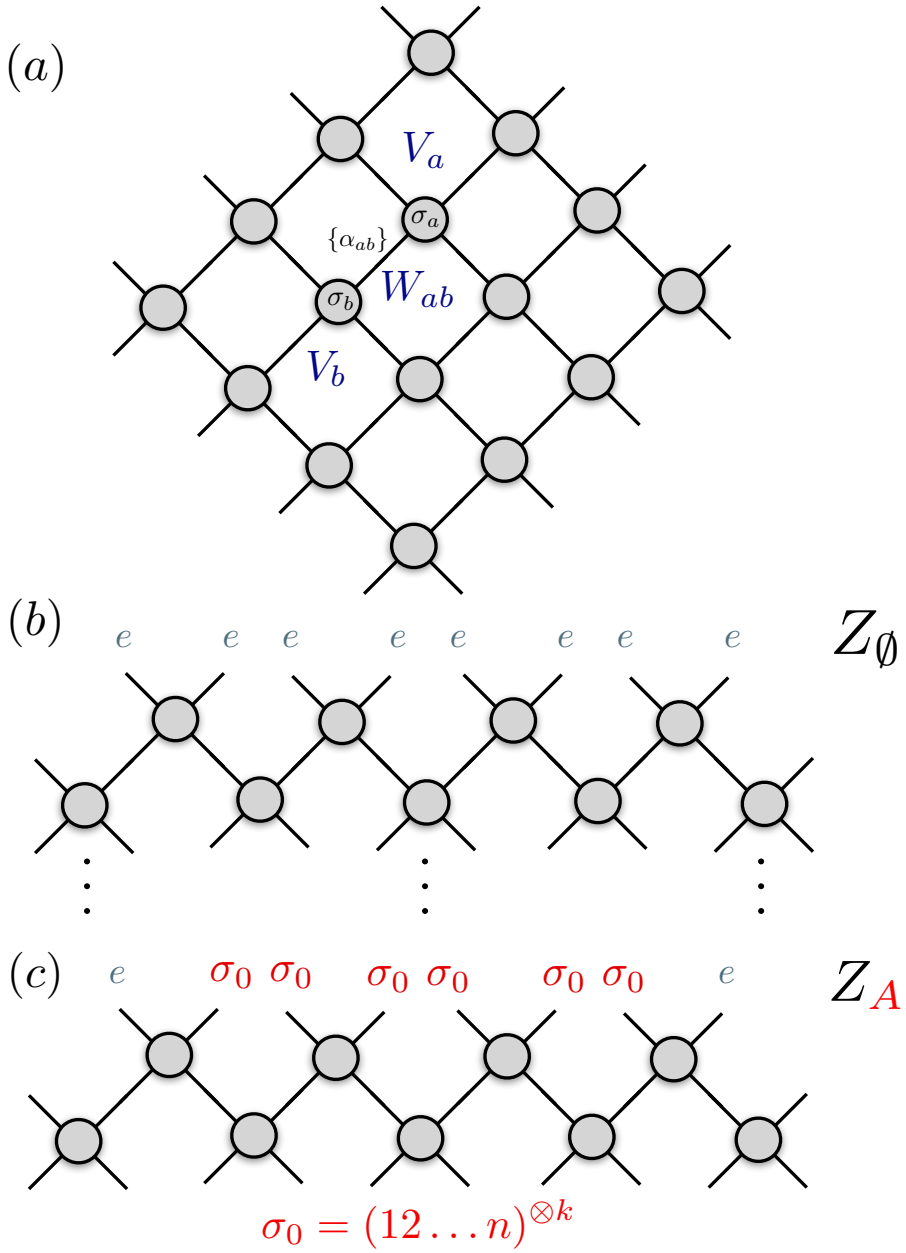

Figure A.1. Replicated statistical mechanics model. (a) The replicated statistical model is defined on a tilted square lattice, with permutation degrees of freedom $\sigma_a \in \mathcal{S}_Q$ living on vertices, and charge degrees of freedom $\{\alpha^i\}_{i=1,\ldots,Q}$. The Boltzmann weights have contributions from both vertices V_a, see Eq. (A.10), and links W_{ab}, Eq. (A.9). (b) Fixed boundary conditions in $Z_\emptyset$ at the top layer (ending the circuit at a given time t), with all permutations fixed to e. (c) The partition function Z_A differs from $Z_\emptyset$ by the boundary condition fixed to σ_0 in the entanglement interval A. This creates a domain wall (DW) that follows a minimal cut in the limit $d \to \infty$.

1) DW constraint. We first consider a link joining two vertices that we label "1" and "2". If we integrate out the qudit degrees of freedom, we find the following weight for the links

$$\begin{aligned} W_{12}(\sigma_2^{-1}\sigma_1) &= \sum_{g_1^i, g_2^i} \mathrm{Tr}\left[(g_1^i \alpha_1^i; \sigma_1)(g_2^i \alpha_2^i; \sigma_2)^\dagger\right] \\ &= d^p \delta_{C_1} ... \delta_{C_p}, \end{aligned} \tag{A.2}$$

where $C_1 ... C_p$ is the cycle structure of the permutation element $\sigma_2^{-1}\sigma_1$, p is the number of cycles in that permutation, and δ_{C_i} is equal to 1 if all charge states of the replicas within cycle C_i are the same, and otherwise equal to 0. Note that we cannot sum over the charges α^i as these depends on the states at neighboring links (see Fig. 2.6).

Intuitively we can interpret the above result as follows. Since the link is shared between vertices with different permutations σ_1 and σ_2 then we must have the following constraint

$$(g^i \alpha^i; \sigma_1) = (g^i \alpha^i; \sigma_2), \tag{A.3}$$

which is true if and only if $\sigma_2^{-1}\sigma_1(\{\alpha_i\}) = \{\alpha_i\}$, and $\sigma_2^{-1}\sigma_1(\{g_i\}) = \{g_i\}$. Let us take the simple case where $\sigma_2^{-1}\sigma_1$ is equal to a transposition, say, (12). We can interpret the above equation as saying that $g_1 = g_2$ and $\alpha_1 = \alpha_2$. The $g_1 = g_2$ condition will reduce the number of allowed basis qudit states from d^Q to d^{Q-1}, and since all qudit contributes equally, the weight of the link in this case will be reduced by a factor $1/d$ due to the reduced configurational entropy in the qudit sector. For the qubit degrees of freedom, we cannot sum over all spins due to the non-local charge conservation constraint. The more general case of $\sigma_2^{-1}\sigma_1 \in \mathcal{S}_Q$ follows similarly, giving (A.2). An important thing to note is that each transposition in $\sigma_2^{-1}\sigma_1$ reduces the weight by $1/d$ and the weight is strongest when $\sigma_2 = \sigma_1$, that is when there is no DW –

corresponding to a ferromagnetic interaction. Thus at large d limit, it is expensive to have a DW and the system will remain in an ordered phase unless DW are forced, for example, at the entanglement cut (see Fig. A.1). This will play an important role in the subsequent discussion.

2) Measurement constraint. If the link $\langle 12 \rangle$ happens to be measured, then the measurement outcomes are same in all replicas, that is, all copies are acted on with the same projection operator. If the projection operator is denoted as $P = P^q \otimes P^d$, then we have the weight

$$W_{12}(\sigma_2^{-1}\sigma_1; P) = \mathrm{Tr}\left[(g_2^i \alpha_2^i; \sigma_2)^\dagger P^{\otimes Q} (g_1^i \alpha_1^i; \sigma_1) P^{\otimes Q}\right]. \tag{A.4}$$

Averaging over all measurement outcomes results in

$$\begin{aligned} W_{12} &= \sum_{s=0,1} \sum_{x=1,\ldots,d} W_{12}(\sigma_2^{-1}\sigma_1; P_s^q \otimes P_x^d), \\ &= d \sum_{s=0,1} \prod_i \delta_{\alpha^i, s}, \end{aligned} \tag{A.5}$$

where $\delta_{\alpha^i,s}$ ensures that the charge state of the i^{th} replica is compatible with the measurement outcome $s = 0, 1$ of the qubit. Whenever a measurement occurs, all Q charges on the corresponding link are constrained to be same. This gives the δ factor in (A.5). For the qudit sector, this leads to a decrease in configurational entropy from d^Q to d. An important observation is that the link weights W_{ab} do not depend on the permutation $\sigma_b^{-1}\sigma_a$, a result of crucial importance for the discussion below.

A.2 Replicated model

Combining all these results we can write a statistical model with the partition function given by,

$$Z = \sum_{\mathbf{m}} Z[\mathbf{m}], \tag{A.6}$$

$$Z[\mathbf{m}] = \sum_{\text{configurations}} \left(\prod_{(ab)\in\text{links}} \prod_{v\in\text{vertices}} W_{ab}(\sigma_b^{-1}\sigma_a) V_v \right), \tag{A.7}$$

where $\sum_{\mathbf{m}} \equiv \sum_{\{\mathbf{X}\}} p^{N_{\mathbf{X}}}(1-p)^{LT-N_{\mathbf{X}}} \sum_{\{\mathcal{M}(\mathbf{X})\}}$, where $\mathbf{X}$ denotes a configuration of measurement locations, $N_{\mathbf{X}}$ is the number of links being measured (number of bonds in the percolation configuration $\mathbf{X}$), L is the spatial length of the system, T is the number of time steps; and $\mathcal{M}(\mathbf{X})$ is the set of qubit measurement outcomes at measurement locations $\mathbf{X}$. The sum over configurations is given by

$$\begin{aligned} \sum_{\text{configurations}} &\equiv \sum_{\{\sigma_v\}\in\mathcal{S}_Q} \sum_{\{\alpha^1\}=0,1} \cdots \sum_{\{\alpha^Q\}=0,1} \\ &\equiv \sum_{\{\sigma_v\}\in\mathcal{S}_Q} \sum_{\{\alpha\}}, \end{aligned} \tag{A.8}$$

corresponding to permutation and charge degrees of freedom in each replica. The link weights W_{ab} are given by

$$W_{ab}(\sigma_b^{-1}\sigma_a) = \begin{cases} d^{|\sigma_b^{-1}\sigma_a|-Q}\delta_{C_1}\ldots\delta_{C_{|\sigma_b^{-1}\sigma_a|}} & \text{if } (ab) \text{ not in } \mathbf{X} \\ d^{1-Q}\delta_{\alpha^i,s_{ab}} & \text{if } (ab) \text{ in } \mathbf{X} \end{cases}, \tag{A.9}$$

with $s_{(ab)} \in \mathcal{M}(\mathbf{X})$ the measurement outcome of the qubit on link (ab). Finally, the vertex weight V_v is given by

$$V_v = \prod_{i=1}^{Q} \frac{\delta_{\alpha_1^i\beta_1^i}\delta_{\alpha_2^i\beta_2^i} + \delta_{\alpha_1^i\beta_2^i}\delta_{\alpha_2^i\beta_1^i}}{2} = \prod_{i=1}^{Q} V_v^i, \tag{A.10}$$

where $\alpha_{1,2}$ and $\beta_{1,2}$ are incoming and outgoing charges (see Fig. 2.6). We note that V_v factorizes over the replicas, that is, $V_v = \prod_{i=1}^{Q} V_v^i$; this will play an important role in factorizing $Z[\mathbf{m}]$ in the discussion below.

α_l^i	Charge at link l and copy i
$\{\alpha^i\}$	Set of charges on all links for copy i
$\{\alpha_l\}$	Set of charges on link l for all copies
$\{\alpha\}$	Set of charges on all links and copies
$\delta_{\{\alpha\}}^{\{l\}}$	All copies of α on set of links $\{l\}$ are equal
$\delta_{\{\alpha\},\{\mathcal{M}\}}^{\{l\}}$	All copies of $\{\alpha\}$ on links $\{l\}$ are equal to $\{\mathcal{M}\}$

Table A.1. Table summarizing the meaning of various notations used in this appendix.

Note that we have integrated out the qudit sector from the model. This was possible due to each qudit on a given link being independent of the values at other links. However, this is not possible for the U(1) sector on account of non-local constraints due to the charge conservation. Importantly, the statistical model $Z(\mathbf{m})$ should be thought of as a quenched disordered model where the measurement locations and outcomes (for the qubit) are quenched "impurities"; averaged quantities in the original problem have become quenched average in the statistical model. From now on, $\mathbf{m} = \{\mathbf{X}, \mathcal{M}(\mathbf{X})\}$ will denote the system's quantum trajectory with measurement locations + U(1) measurement outcomes fixed, corresponding to a fixed "disorder" realization of the statistical model. This is unlike the previous-works on the non symmetric problem where the randomness in the measurement locations were absorbed in the statistical model in an annealed way.

A.3 Replica limit

We now proceed to take the replica limit, and will use various notations summarized in Table A.1.

We first focus on the partition function $Z_\emptyset(\mathbf{m})$, where the links at the top boundary are restricted to be of the form $(g^i\alpha^i; e)$. The permutation identity element e represents the fact that we are tracing over all the system and is equal to the Born probability of observing the particular trajectory $\mathbf{m}$. As mentioned above, a DW in

the statistical model is suppressed by $1/d^{Q-p}$, where p is the number of cycles in the DW. Thus, the leading order contribution to $Z_\emptyset$ comes when all vertex elements being equal to e. This simplifies $Z_\emptyset(\mathbf{m})$ dramatically as we do not need to sum over the permutation elements. We have

$$Z_\emptyset(\mathbf{m}) = d^{(1-Q)N_m} \left(\sum_{\{\alpha\}=0,1} \delta^{\mathbf{m}}_{\{\alpha\},\mathcal{M}(\mathbf{m})} \prod_v V_v \right),$$

where N_m is the number of measured links, $\delta^{\mathbf{m}}_{\{\alpha\},\mathcal{M}(\mathbf{m})}$ is non-zero and equal to 1 if and only if the charges $\{\alpha\}$ on the measured sites are equal to the measurement outcomes $\mathcal{M}(\mathbf{m})$ of the qubit, and V_v is given in (A.10). Intuitively, we should only sum over charge configurations compatible with the measurement outcomes. The partition function can be factorized over replicas to give,

$$Z_\emptyset(\mathbf{m}) = d^{(1-Q)N_m} \left(Z^{(1)}_\emptyset(\mathbf{m}) \right)^Q, \tag{A.11}$$

where $Z^{(1)}_\emptyset(\mathbf{m})$ is given by

$$Z^{(1)}_\emptyset(\mathbf{m}) = \sum_{\{\alpha\}} \delta^{\mathbf{m}}_{\{\alpha\},\mathcal{M}(\mathbf{m})} \prod_v V^{(1)}_v. \tag{A.12}$$

The superscript (1) denotes the fact that the quantity is for a single replica.

We can similarly factorize $Z_A(\mathbf{m})$ with the caveat that we now have a minimal cut for the permutation degrees of freedom running through the system (see discussion in Section 2.3.1). A DW between e and $(1...n)^{\otimes k}$ reduces the link weight by $d^{k+1-Q} = d^{-(n-1)k}$ (A.9) and the contribution of the cut to the partition function is thus given by $d^{-(n-1)k\ell_{\mathrm{DW}}}$, where ℓ_{DW} is the length of the minimal cut. There are $k+1$ cycles

in the DW; k cycles of the type $(1...n)$ and the last one being an identity on a single copy. Thus we can factorize $Z_A(\mathbf{m})$ as

$$\begin{aligned} Z_A(\mathbf{m}) &= d^{(1-Q)N_m-(n-1)k\ell_{\mathrm{DW}}} \\ &\quad\times \sum_{\{\alpha^i\}=0,1} \delta^{\mathbf{m}}_{\{\alpha\},\mathcal{M}(\mathbf{m})} \prod_{C_a} \delta^{\mathrm{DW}}_{\{\alpha^{C_a}\}} \prod_v V_v, \end{aligned} \tag{A.13}$$

the where $\delta^{\mathrm{DW}}_{\{\alpha^{C_a}\}}$ is non-zero (and equal to 1) if and only if the charges within the cycle C_a are the same on (unmeasured) links on the minimal cut. We can further factorize the above equation to get,

$$Z_A(\mathbf{m}) = d^{(1-Q)N_m-(n-1)k\ell_{\mathrm{DW}}} \left(Z_A^{(n)}(\mathbf{m})\right)^k Z_\emptyset^{(1)}(\mathbf{m}), \tag{A.14}$$

where

$$\begin{aligned} Z_A^{(n)}(\mathbf{m}) &= \sum_{\{\alpha\}} \delta^{\mathrm{DW}}_{\{\alpha\}} \prod_{i=1}^{n} \left(\delta^{\mathbf{m}}_{\{\alpha^i\},\mathcal{M}(\mathbf{m})} \prod_v V_v^i \right) \\ &= \sum_{\beta_1...\beta_{\ell_{\mathrm{DW}}}} \prod_{i=1}^{n} \left(\sum_{\{\alpha^i\}} \delta^{\mathrm{DW}}_{\{\alpha^i\},\{\beta\}} \delta^{\mathbf{m}}_{\{\alpha^i\},\mathcal{M}(\mathbf{m})} \prod_v V_v^i \right) \\ &\equiv \sum_{\{\beta\}} Z_A\left[\mathbf{m};\{\beta\}\right]^n \end{aligned} \tag{A.15}$$

with $\delta^{\mathrm{DW}}_{\{\alpha\},\{\beta\}}$ non-zero (and equal to 1) if and only if all copies of charges on the unbroken (not measured) links along the minimal cut are equal to $\{\beta\}$. The superscript (n) denotes the fact that we have n charge copies. Using the above results and (2.12), we find

$$S_n(\mathbf{m}) = \frac{-1}{n-1} \lim_{k\to 0} d^{(1-Q)N_m} Z_\emptyset^{(1)}(\mathbf{m}) \frac{d^{-(n-1)k\ell_{\mathrm{DW}}} \left(Z_A^{(n)}\right)^k - \left(Z_\emptyset^{(1)}\right)^{nk}}{k}. \tag{A.16}$$

Remarkably, this factorized form allows us to take the replica limit *exactly*:

$$S_n(\mathbf{m}) = \frac{-1}{n-1} Z_{\emptyset}^{(1)}(\mathbf{m}) \ln \frac{Z_A^{(n)}}{\left(Z_{\emptyset}^{(1)}\right)^n} + \ln d \; \ell_{\mathrm{DW}},$$
$$= \frac{-1}{n-1} Z_{\emptyset}^{(1)}(\mathbf{m}) \ln \left(\sum_{\{\beta\}} \frac{Z_A[\mathbf{m}; \{\beta\}]^n}{\left(Z_{\emptyset}^{(1)}\right)^n} \right) + \ln d \; \ell_{\mathrm{DW}}, \tag{A.17}$$

where $\{\beta\}$ represents all possible configuration of the charge on the unmeasured links along the minimal cut. We can further think of $\frac{Z_A[\mathbf{m};\{\beta\}]}{\left(Z_{\emptyset}^{(1)}\right)}$ as the probability for the charges along the unbroken links of the minimal cut to be equal to $\{\beta\}$ in the statistical model described by the partition function $Z_{\emptyset}^{(1)}$. Denoting this probability by $p_{\{\beta\}}$ we have our final result

$$S_n(\mathbf{m}) = \frac{-1}{n-1} Z_{\emptyset}^{(1)}(\mathbf{m}) \ln \left(\sum_{\{\beta\}} p_{\{\beta\}}^n \right) + \ln d \; \ell_{\mathrm{DW}}. \tag{A.18}$$

A.4 $p = 0$ limit

To illustrate the meaning of the statistical model (A.18), we compute S_n for $p = 0$. Let us start from the following product state,

$$|\psi_0\rangle = \left(a_0 |0\rangle + a_1 |1\rangle\right)^{\otimes L}. \tag{A.19}$$

In terms of the statistical model, this corresponds to the bottom links being in charge states 1 or 0 with probability a_1^2 and a_0^2 respectively. The minimal cut will be spatial in nature as we are considering late times and $\ell_{\mathrm{DW}} = L_A$ since the permutations are fully ordered. Since the vertex weights (A.10) are SU(2) symmetric, the link charge states are invariant under time evolution. This immediately gives $p_{\{\beta\}} = a_0^{2N_0} a_1^{2N_1}$,

where $N_{0,1}$ are the number of links with charge $0, 1$ in $\{\beta\}$. Using Eq. (A.18), we find the following expression for the Rényi entropies at late times:

$$S_n = \frac{-1}{n-1} \ln \left(|a_0|^{2n} + |a_1|^{2n} \right)^{L_A} + L_A \ln d. \tag{A.20}$$

This result is consistent with thermalization to a density matrix $\rho_A = e^{-\mu \mathcal{Q}}/\mathrm{Tr} e^{-\mu \mathcal{Q}}$, where the chemical potential μ is set by charge conservation

$$\langle \mathfrak{q} \rangle = a_1^2 = \mathrm{Tr}\left[\mathfrak{q} \rho_A\right] = \frac{e^{-\mu}}{1 + e^{-\mu}}. \tag{A.21}$$

We check that the Rényi entropies are indeed given by $S_n = \frac{-1}{n-1} \ln \mathrm{Tr} \rho_A^n$, since

$$S_n = L_A \left(\ln d + \frac{1}{n-1} \ln \left(\langle \mathfrak{q} \rangle^n + (1 - \langle \mathfrak{q} \rangle)^n \right) \right), \tag{A.22}$$

which coincides with (A.20).

A.5 Charge variance

In this section we briefly discuss evaluating the charge variance $[\delta \mathcal{Q}^2]$ in the language of the statistical model discussed above. The charge variance for fixed measurement locations and outcomes is given by $\delta \mathcal{Q}^2_{\mathbf{m}} = \langle \mathcal{Q}^2 \rangle_{\mathbf{m}} - \langle \mathcal{Q} \rangle^2_{\mathbf{m}}$. As the first term is linear in $\rho_{\mathbf{m}}$, the average over measurement outcomes will give a trivial answer at infinite temperature (see point 3 in Section **??**). We have

$$[\langle \mathcal{Q}^2 \rangle] = \mathrm{Tr} \mathcal{Q}^2 / \mathrm{Tr} \mathbb{I} = L(L+1)/4,$$

where charges take value 0 and 1. Any non-trivial physics is hidden in the second term. Nevertheless, the distribution of the variance over various trajectories is an

interesting quantity, and it will be useful to evaluate this quantity using the replica trick.

We first consider the second term which is given by,

$$[\langle \mathcal{Q} \rangle^2] = \sum_{\mathbf{m}} \mathbb{E}_U \left[p_{\mathbf{m}} \left(\frac{\mathrm{Tr}\left(\mathcal{Q}\rho_{\mathbf{m}}\right)}{\mathrm{Tr}\rho_{\mathbf{m}}} \right)^2 \right].$$

We can use the replica trick to re-write the above expression as

$$\begin{aligned} [\langle \mathcal{Q} \rangle^2] &= \lim_{k\to 0} \sum_{\mathbf{m}} \mathbb{E}_U \left[\left(\mathrm{Tr}\left(\mathcal{Q}\rho_{\mathbf{m}}\right)\right)^2 \left(\mathrm{Tr}\rho_{\mathbf{m}}\right)^{2k-1} \right], \\ &= \lim_{k\to 0} \sum_{\mathbf{m}} \mathbb{E}_U [\mathrm{Tr}\rho_{\mathbf{m}}^{\otimes(2k+1)} T], \end{aligned} \tag{A.23}$$

where T is an operator acting on the $2k+1$ copies at the top boundary and is given by $T = \mathcal{Q} \otimes \mathcal{Q} \otimes \mathbb{I} \cdots \otimes \mathbb{I}$. As discussed above, the above quantity maps to a classical statistical model on averaging over random unitary gates U. Since the action of T does not mix different copies, we can factorize the contribution of different copies as in Section A.3. The resulting expression, after taking the replica limit, is given by

$$[\langle \mathcal{Q} \rangle^2] = \sum_{\mathbf{m}} Z_{\emptyset}^{(1)}(\mathbf{m}) \langle \mathcal{Q}_{\mathrm{T}} \rangle^2_{\mathbf{m},\mathrm{stat}}, \tag{A.24}$$

where $\langle \cdot \rangle_{\mathrm{stat}}$ is the average in the statistical model described by the partition function $Z_{\emptyset}^{(1)}(\mathbf{m})$ (see eq A.12), and the subscript T in $\mathcal{Q}$ is to denote the fact that it is a quantity defined on the top boundary. As mentioned before, there is no simple expression for $[\langle \mathcal{Q} \rangle^2]$, but we can use the statistical mechanics model to evaluate it numerically. Similarly, for $\langle \mathcal{Q}^2 \rangle_{\mathbf{m}}$ the top operator T is given by $T = \mathcal{Q}^2 \otimes \mathbb{I} \cdots \otimes \mathbb{I}$ and we have

$$[\langle \mathcal{Q}^2 \rangle] = \sum_{\mathbf{m}} Z_{\emptyset}^{(1)}(\mathbf{m}) \langle \mathcal{Q}^2_{\mathrm{T}} \rangle_{\mathbf{m},\mathrm{stat}}. \tag{A.25}$$

APPENDIX B

STATISTICAL MECHANICS MODEL FOR GENERAL ABELIAN SYMMETRIES

In this section, we generalize the statistical mechanics models to general Abelian groups, and discuss consequences of charge-sharp phases under duality transformations. Notably, our results suggest the existence of volume-law entangled phases with symmetry protected and intrinsic topological order.

B.1 Haar average

Consider a general Abelian group G, with $\alpha \in \{1 \dots |R|\}$ labeling the different combinations of total charge for pairs of sites (e.g. for the U(1) model $\alpha \in \{-1, 0, +1\}$, for $\mathbb{Z}_N$ $\alpha \in \{0 \dots N-1\}$ etc...). We can decompose a symmetric two-site unitary into a direct sum of reps: $U = \sum_\alpha U_\alpha P_\alpha$, where P_α is a projector onto the α^{th}-charge-sector subspace. The main object in the statistical mechanics model is the unitary average of $\mathbb{E}_U \left[U^Q \otimes U^{*Q}\right]$ where Q is the number of replicas, which decomposes into a direct sum of all R^{2Q} charge-sector combinations. Since Haar-averaging requires that each U_α is "paired" with a complex-conjugated partner U_α^* of the same total charge, only terms in which the U^{*Q} charge-sectors form a permutation of the U^Q charge-sectors contribute. For each of these surviving combinations of charge-sectors, denote by n_α the number of times that charge-sector α appears in U^Q, and choose permutation elements $\sigma, \tau \in S_Q$ that sort the Q replicas into groups of the same charge. Then we can write:

$$\mathbb{E}_U\left[U^Q \otimes U^{*Q}\right] = \sum_{n_{1\ldots R}:\sum_\alpha n_\alpha = Q} \sum_{\sigma,\tau \in \frac{S_Q}{S_{n_1}\times\ldots S_{n_R}}} W_{\sigma,\tau} \bigotimes_\alpha \mathbb{E}_U\left(U_\alpha^{n_\alpha} P_\alpha^{n_\alpha} \otimes U_\alpha^{*n_\alpha} P_\alpha^{*n_\alpha}\right) W_{\sigma,\tau}^\dagger \tag{B.1}$$

where $W_{\sigma,\tau}$ is the unitary acting on $\mathcal{H}^q \otimes \mathcal{H}^{*q}$ that permutes the Q copies of U by σ and the Q copies of U^* by τ, and the permutation elements σ, τ range over the quotient group $\frac{S_Q}{S_{n_1}\times\ldots S_{n_R}}$ to avoid over counting equivalent permutations that cycle identical replicas with the same charge-sector. Here we have labeled projectors acting on $\mathcal{H}^*$ with a * simply for readability, and this mark carries no mathematical content.

The Haar average of each charge-sector-group is:

$$\mathbb{E}_U\left(U_\alpha^{n_\alpha} \otimes U_\alpha^{*n_\alpha}\right) = \sum_{\sigma_\alpha,\tau_\alpha \in S_{n_\alpha}} \mathrm{Wg}_{D_\alpha d^2}(\sigma_\alpha^{-1}\tau_\alpha; n_\alpha) |\sigma_\alpha\rangle\rangle\langle\langle\tau_\alpha|,$$

where Wg is the Weingarten function, D_α is the number of states in the charge-sector α, and $|\sigma\rangle\rangle$ denotes the operator which permutes the input legs of U by σ, and contracts them with the corresponding legs of U^* (and similarly for $\langle\langle\sigma|$ acting on the output legs). For our purposes, we will only need the large-d limit:

$$\lim_{d\to\infty} \mathrm{Wg}_d(\sigma^{-1}\tau; Q) \sim \frac{1}{d^Q}\delta_{\sigma,\tau}. \tag{B.2}$$

The sum over the total-charge sector permutations σ_α, can now be combined with the quotient-group permutations σ, τ to yield a simpler sum over S_Q permutations:

$$\begin{aligned}\mathbb{E}_U\left[U^Q \otimes U^{*Q}\right] =& \frac{1}{d^{2Q}} \sum_{\alpha_1\ldots\alpha_Q} \prod_i D_{\alpha_i}^{-1} \sum_{\sigma\in S_Q} \\ & P_{\alpha_1}\otimes\ldots P_{\alpha_Q} \otimes P^*_{\alpha_{\sigma(1)}} \otimes \ldots P^*_{\alpha_{\sigma(Q)}} |\sigma\rangle\rangle\langle\langle\sigma| P_{\alpha_1}\otimes\ldots P_{\alpha_Q} \otimes P^*_{\alpha_{\sigma(1)}} \otimes \ldots P^*_{\alpha_{\sigma(Q)}}.\end{aligned} \tag{B.3}$$

Note that, the two sets of projectors are partly redundant since $P_\alpha^2 = P_\alpha$, and since $P_\alpha \otimes \mathbb{1}|\sigma\rangle\rangle = \mathbb{1} \otimes P_{\alpha_{\sigma(i)}}|\sigma\rangle\rangle$, but are written in this way to emphasize that charge is

separately conserved in each replica, and also that the charge-sector labels on the $\mathcal{H}^*$ spaces are related to those in the $\mathcal{H}$ spaces by the permutation element σ.

Though complicated in appearance, Eq. B.3 has a simple interpretation: each gate becomes a vertex in the statistical mechanics model labeled by i) a permutation element $\sigma \in S_Q$, and ii) Q-different total charge-sector labels (those of the conjugate copies are related by permutation), which can be conveniently associated with the Q different individual link charges. After averaging, the indices of the gate input and output are unrelated, except by total charge conservation in each replica. Hence any input charge configuration can be transferred with equal weight $\sim 1/D_\alpha$ to any outgoing charge configuration with the same total charge α. The remaining rules for domain wall and measurement constraints closely parallel those of the U(1) model described above.

Example: $\mathbb{Z}_2$ Symmetric Monitored Circuits As an example, consider a random monitored circuit ensemble with symmetry group $G = \mathbb{Z}_2$, consisting of qubits with $\mathbb{Z}_2$ symmetry charge $\mathfrak{q}_i = \frac{1+\sigma_i^x}{2} \in \{0, 1\}$, and charge addition rule $\mathcal{Q} = \sum_i \mathfrak{q}_i \bmod 2$, (each accompanied by large dimension qudits that transform trivially under the symmetry). The effective statistical mechanics model in the $d \to \infty$ limit is an "8-vertex" model, which has an additional two vertices compared to the U(1)/6-vertex case that respectively correspond to pair creation and annihilation of charges, and differs also in that all 8 vertices come with weight $v = 1/2$.

Example: $\mathbb{Z}_N$ Symmetric Monitored Circuits As a second example, we can consider models with symmetry group $G = \mathbb{Z}_N$ for general N consisting of "quNits" with charge basis states $\{|0\rangle, \ldots |N-1\rangle\}$ having symmetry charge $\mathfrak{q} = 0 \ldots N-1$ (again, each accompanied by large-d qudits). The resulting statistical mechanics model would be an N^3-vertex model, with N different groups of vertices corresponding to the N-different total charges, and each group has N different ways to apportion

the incoming charge between the two input legs, and N different ways to apportion it between the output legs, each weighted by a factor of $v = 1/N$.

From these examples, one can readily generalize to arbitrary finite Abelian groups for which G can be written as a product of different $\mathbb{Z}_N$ factors.

APPENDIX C

ADDITIONAL NUMERICAL RESULTS

C.1 Entanglement dynamics in the statistical mechanics model

In this appendix, we present additional results on the entanglement dynamics obtained from the statistical mechanics model.

We start with the $p = 0$ case, and analyze how the argument for $\sqrt{t}$ growth translates to the statistical model language. We are working in the regime where $L \gg t$, so the minimal cut runs along the time direction. For simplicity of the argument, we assume that the cut does not fluctuate and is exactly vertical, that is, the cut passes through the same link at all times (we checked that our results are independent from averaging over fluctuations of the minimal cut). Using Eq. (2.18), the Rényi entanglement entropies are related to the classical Rényi entropies for charge configurations along the minimal cut. Let us denote this distribution by P_{DW}, with $S_\infty = \ln p_{\max}$, where $p_{\max}$ is the maximum of P_{DW}. We find that $p_{\max}$ is given by $P_{\mathrm{DW}}(0...0) \equiv P_0$. P_0 is the probability for all charges on the vertical cut to be equal to 0 (equivalently, we could have also considered $P_{\mathrm{DW}}(1...1) \equiv P_1$). P_0 describes the part of the dynamics where there are no exchange of charge across the cut and is therefore dominated by dead regions in the initial state, which we know to be the source of the dominant contribution in the Schmidt values. As we discussed in Sec. 2.1, if the initial state has a dead region of size $\sqrt{t}$ centered at the entanglement cut, charges cannot diffuse to the cut until times of order t, so the configurational entropy of charge along the vertical minimal cut will remain zero. It follows that $P_0 \geq \exp(-\sqrt{Dt})$ and therefore that $S_n \leq \sqrt{Dt}$ for $n > 1$. Meanwhile, typical components of the initial

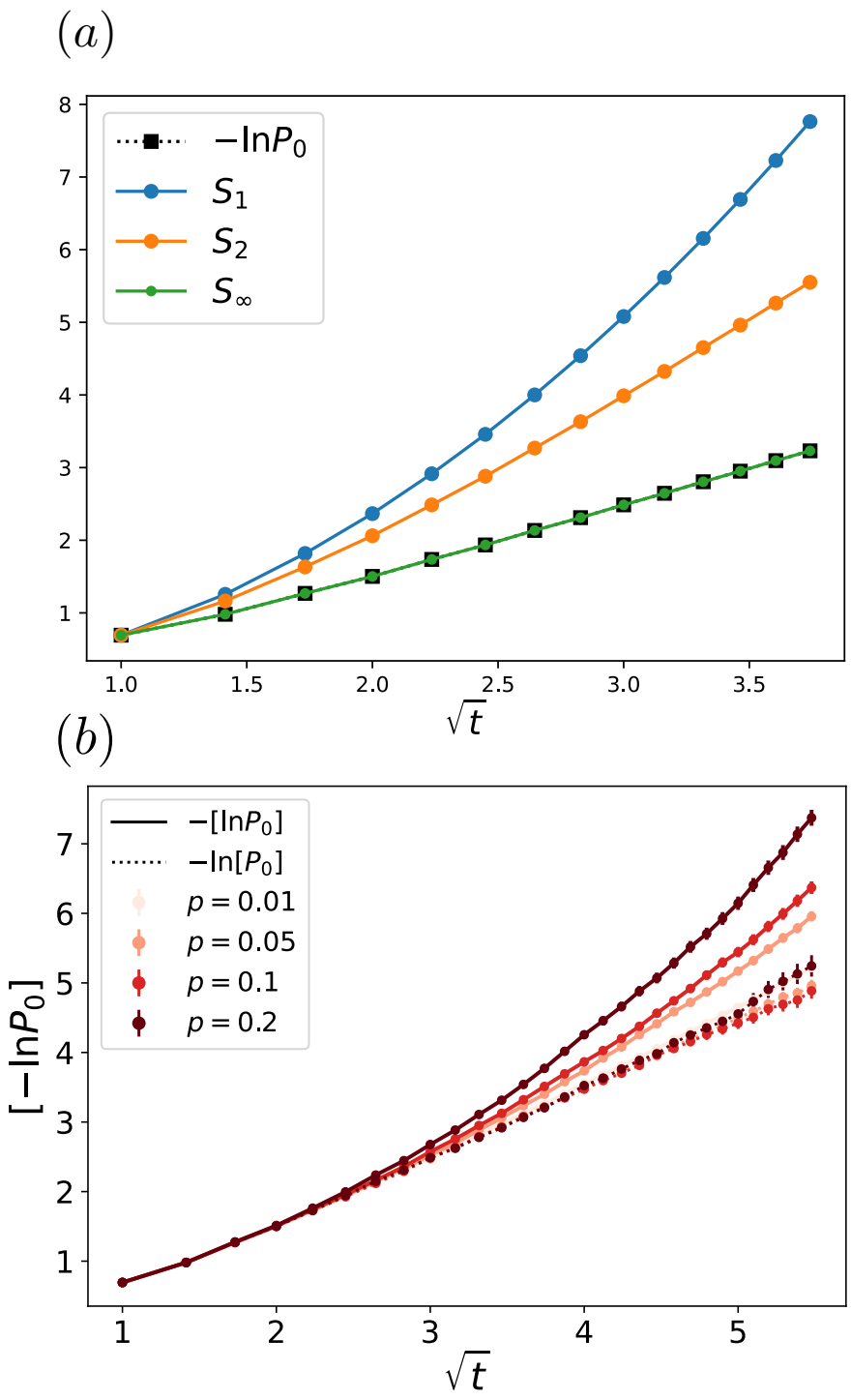

Figure C.1. Entanglement dynamics in the statistical mechanics model. (a) Plot of S_1, S_2, S_∞, and $-\ln P_0$ vs $\sqrt{t}$ for $p = 0$ obtained using the statistical model with a fixed vertical minimal cut. We clearly see different growth of S_1 and S_∞, S_2. The curve of $-\ln P_0$ exactly overlaps the S_∞ curve as argued in the main text. (b) Plot showing $[-\ln P_0]$ vs $\sqrt{t}$ for various p, and $L = 12$. We find that this quantity grows linearly with time for any non-zero p. We also plot the average $-\ln[P_0]$ for various p (dashed curves), which grows as $\sqrt{t}$ independently of p.

wavefunction give rise to essentially random charge configurations on the minimal cut. Owing to the greater multiplicity of typical configurations they dominate S_1, which grows linearly in t. These expectations are borne out in Fig. C.1(a).

We now turn to $p > 0$. For $p > 0$, the charge on measured sites in a given trajectory is constrained to match the measurement outcome. As we noted in Sec. 2.1, this suffices to eliminate dead regions in typical trajectories. To capture the effect of dead regions on the growth of S_∞ for $p > 0$, we calculate $-\ln P_0$ as a proxy for entanglement entropies. For numerical convenience, we make two simplifying assumptions: (1) we ignore fluctuations of the minimal cut, (2) we do not perform measurements on links adjacent to the cut (this avoids numerically expensive postselection procedures as the trajectories with non-zero P_0 quickly become rare as we increase p).

We plot $[-\ln P_0]$ and $-\ln[P_0]$ vs $\sqrt{t}$ in Fig. C.1(b). We find that the quantity $-\ln[P_0]$ grows as $\sqrt{t}$ for all p. This is expected because we are averaging over the trajectories before calculating the (pseudo)entropy; this is same as in the $p = 0$ case where the unitary evolution can be seen as equivalent to doing the sum over all trajectories. We find that at low p, $[-\ln P_0]$ stays closer to the $\sqrt{t}$ growth for longer times. At higher p it diverges significantly and crosses over to linear growth. Though $[-\ln P_0]$ is not exactly equal to the Rényi entropy, this transition from $\sqrt{t}$ to linear growth $\sim t$ is a generic phenomenon for all quantities where the survival of dead regions becomes a rare occurrence due to measurements, consistent with the general argument in Sec. 2.1, and the results of Sec. 2.4.

C.2 Charge sharpening dynamics in the fuzzy phase and near the charge-sharpening transition

In this appendix, we present numerical evidence that the charge sharpens on a time scale $t_\# \sim L$, in agreement with the general argument of Sec. 2.1. We plot the fraction N_0 of trajectories with $\delta\mathcal{Q}^2 < \epsilon$ versus $t \sim L$, both in the qubit chain

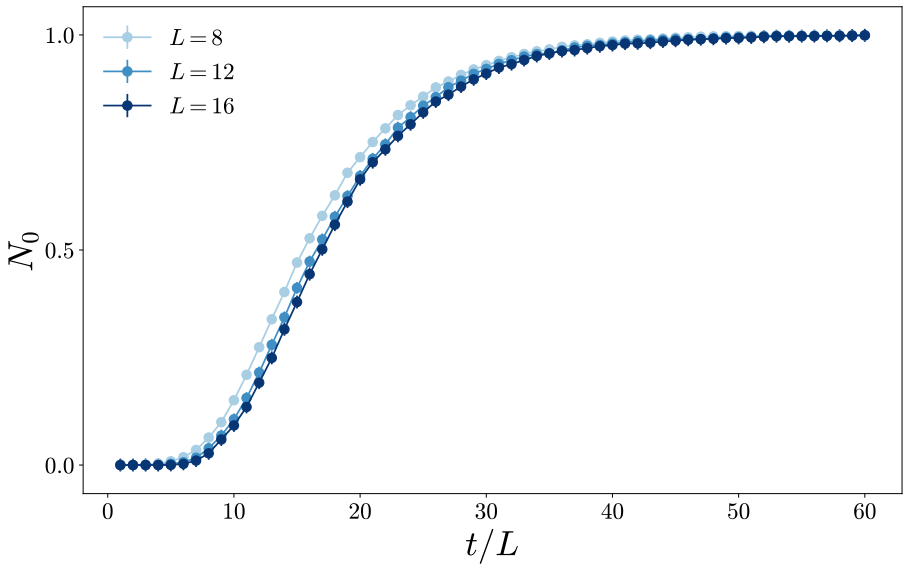

Figure C.2. Dynamics of charge sharpening in qubit chains. Fraction of trajectories with $\delta\mathcal{Q}^2 < \epsilon$ with $\epsilon = 10^{-3}$ at $p = 0.085$, inside the fuzzy phase.

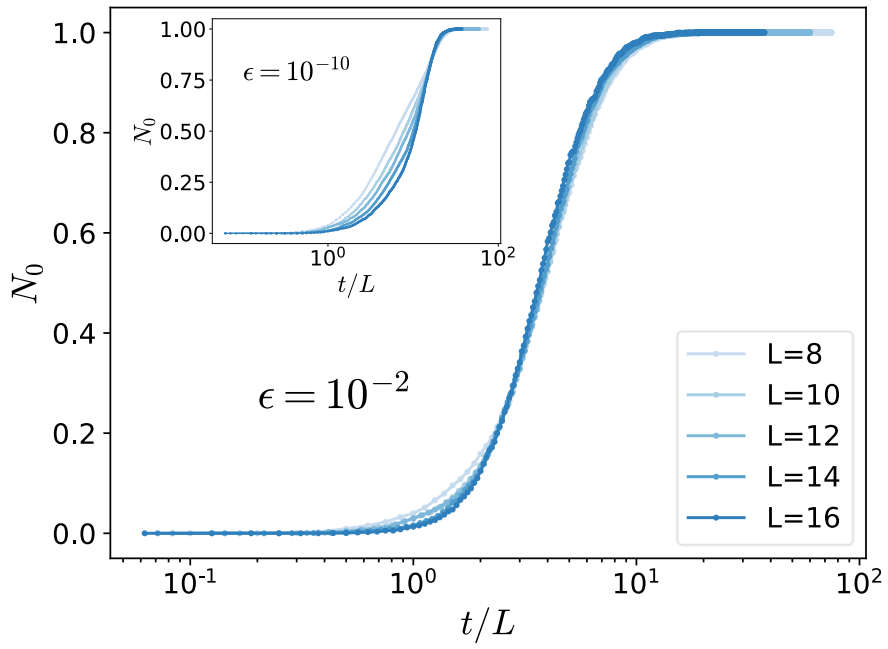

Figure C.3. Dynamics of charge sharpening in the statistical model. Fraction of trajectories with $\delta\mathcal{Q}^2 < \epsilon$ with $\epsilon = 10^{-2}$ at $p = 0.24$, inside the fuzzy phase. Inset: Different threshold $\epsilon = 10^{-10}$, showing a similar scaling of the charge sharpening over a timescale $t \sim L$.

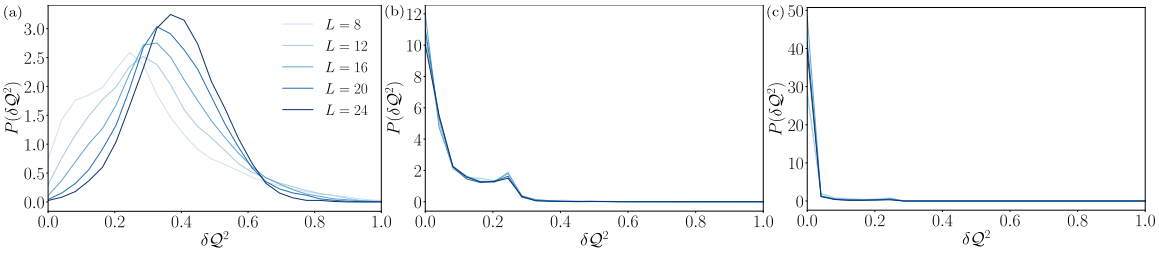

Figure C.4. Charge variance distribution in the qubit model. Distribution of the charge variance at $t/L = 4$ (a) in the charge fuzzy phase $p = 0.05$, (b) near the critical point $p = 0.10$, and (c) in the charge sharp phase $p = 0.14$.

numerics (Fig. C.2) and in the statistical mechanics model (Fig. C.3). We observe a clear crossover when N_0 lifts off from zero on a time scale scaling linearly with L, as expected. Note that this sharpening time scale $t_\# \sim L/p$ is much smaller than the purification time scale $t_\pi \sim \mathrm{e}^L$ [185].

We now turn to the critical dynamics near the charge sharpening phase transition in qubit chains. Before embarking into numerical details, we summarize the physics of the critical dynamics obtained from the simulations.

For generic initial states that mix multiple charge sectors, the charge sharpening happens in two stages: the measurement first sharpens the charge from multiple sectors to two consecutive sectors $(N, N+1)$ The measurement then further collapses the superposition of the two sectors $(N, N+1)$ to a unique charge (either N or $N+1$). The two stages are separated by the crossover time $t_\# \sim L/p$. At much later times $t \gg t_\#$ we find $N_0 \to 1$ in a critical manner that we now turn to.

The numerical simulations of qubit chains suggest that the second stage is governed by charge-sharpening criticality. In the long-time limit, $t \gg t_\#$, we find that the universal scaling law for the critical dynamics is an exponential function,

$$O(t,p) \sim A_O(x) e^{-t/\xi_t(x)}, \text{ where } x \equiv (p - p_\#) L^{1/\nu_\#}, \tag{C.1}$$

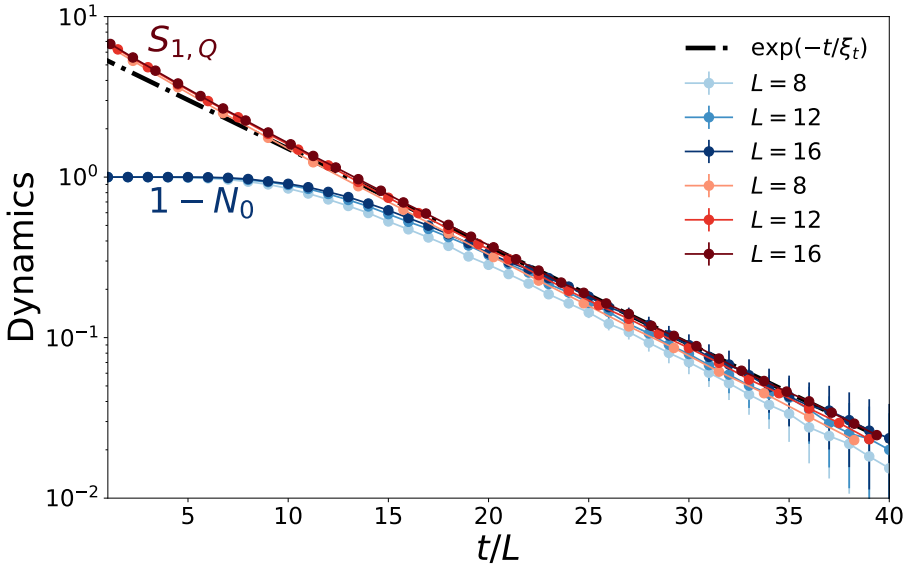

Figure C.5. Critical dynamics of charge-sharpening transition in qubit chains. Comparison of the dynamics of the ancilla entanglement entropy $S_{1,Q}$ and the quantity $1 - N_0$, where N_0 is the fraction of trajectories with $\delta\mathcal{Q}^2 < 0.01$ and the ancilla entanglement entropy $S_{1,Q}$. After rescaling the overall amplitude, both observables collapse to the same exponential function in the long-time limit.

L is the system size, and O is an observable sensitive to the criticality (e.g. N_0 and $S_{1,\mathcal{Q}}$). The universal decay rate ξ_t is a time scale that is different from the crossover time $t_\#$. Due to the space-time symmetry, the time scale ξ_t follows a scaling law,

$$\xi_t(x)/L = B(x). \tag{C.2}$$

Both universal scaling functions $A_O(x)$ and $B(x)$ are smooth in the critical regime. Right at the transition point, we obtain $\xi_t \approx 0.5L/p_\#$.

We now show our numerical evidence to support the above physical picture. We present the charge variance distribution $\delta\mathcal{Q}^2$ in each phase and the vicinity of the charge sharpening critical point in Fig. C.4 to provide additional clarity on the nature of the charge sharpening dynamics. More specifically, Fig. C.4(a) is deep in the charge fuzzy phase characteristic of the first stage of dynamics $t \ll t_\#$. It reveals a wide charge distribution, indicating that the quantum state at this stage is charge

fuzzy and spread across multiple sectors. The middle panel depicts the second stage $t > t_\#$ with $p \approx p_\#$. The charge variance at this stage is peaked at zero and 0.25, indicating the quantum state is either projected to a unique state or a superposition of two consecutive charge sectors $(N, N+1)$, respectively. The third panel is for late time dynamics $t \gg t_\#$ deep in the charge sharp phase. In this regime, only the peak near zero remains, indicating the long-time evolved quantum state has a unique sharp charge as expected.

We now focus on the critical dynamics of the charge-sharpening phase transition. We first present a strong evidence to show that the critical dynamics is only about two consecutive sectors $(N, N+1)$. In Fig C.5, we compare the dynamics of $1 - N_0$ to that of the ancilla-system entanglement entropy $S_{1,\mathcal{Q}}$ (see Sec. 2.2.2 for the definition) in the vicinity of the transition point. The former involves multiple charge sectors, while the latter only involves two consecutive sectors $(N, N+1)$ (with $N = L/2$). After rescaling the overall amplitude, the long-time dynamics of $S_{1,\mathcal{Q}}$ almost perfectly matches with the second stage dynamics of $1 - N_0$, both going like $\sim e^{-t/\xi_t}$. Furthermore, due to the absence of other sectors, the ancilla probe saturates to the critical behavior much earlier than $1-N_0$. We thus conclude that the long-time critical dynamics only involves two consecutive sectors. In the long-time limit $t > t_\#$, both observables decay with the same exponential function, suggesting that the critical dynamics is exponential as in Eq.(C.1) and Eq.(C.2).

We use the ancilla dynamics to establish the universal scaling functions $A_O(x)$ and $B(x)$ in Eq.(C.1) and Eq.(C.2). The scaling function for the amplitude $A_O(x)$ depends on the choice of observable. It has been extracted for N_0 in Fig. 2.4(a) and for the ancilla probe $E_{1,Q}$ in Fig. 2.4(b). In this section, we extract the scaling of $B(x)$ for the universal decay rate. In Fig.C.6, we calculate the long-time dynamics of $S_{1,\mathcal{Q}}$ for various p and system sizes L, then fit the tail to extract the decay rate ξ_t. We find $\xi_t(p, L)$ cross at the transition point $p = p_\#$, indicating the existence of a

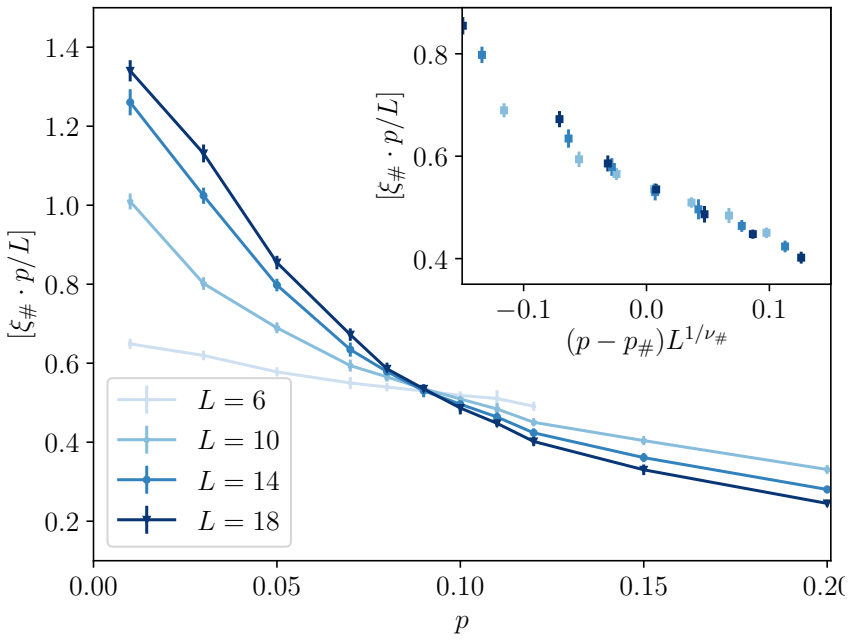

Figure C.6. Universal decay rate of charge-sharpening transition in qubit chains. Data and collapse of the decay rate in the vicinity of the charge-sharpening phase transition. The transition point $p = 0.088$ and the critical exponent $\nu = 2.15$ established in the main text is used to collapse the curves.

scaling function $\xi_t(x)/L = B(x)$. To extract this function, we collapse the curves for different L using the transition point $p_\# = 0.088$ and the critical exponent $\nu_\# = 2.15$ established in Fig.2.4(b).

C.3 Finite size scaling

In the case of qubit chains ($d = 1$), the numerical simulations are performed for system sizes $L \leq 24$. We rely on finite-size scaling protocols to extract the critical properties in the thermodynamic limit. We briefly explain the protocols in this section.

The quantities we studied in the main text, including the tripartite mutual information, the probability of a trajectory with certain charge variance and the ancilla probes shown in Figs. 2.2 and 2.4, all have zero scaling dimension. In the vicinity of the transition point, they share the same finite size scaling ansatz,

$$R(p, L) = f\left((p - p_0)L^{1/\nu}, vL^{-\omega}\right) + ... \tag{C.3}$$

where L is the system size, the measurement probability p is the relevant scaling field with a critical exponent $\nu > 0$. The transition point p_0 is either the entanglement phase transition p_c or the charge-sharpening phase transition $p_\#$.

To make the analysis systematic, we keep the leading irrelevant scaling variable v in the above scaling ansatz. In thermodynamic limit $L \to \infty$, it is suppressed by a non-negative exponent ω. In finite size scaling, however, this field may play an important role. Numerically, we find that the variable v is significant for the ancilla probes while negligible for other quantities. We therefore have to use a more involved finite size scaling protocol as explained below to analyze the ancilla probes [182].

Since our numerics indicates that the scaling function $f(x, y)$ in Eq.(C.3) is analytic for both $x = (p - p_0)L^{1/\nu}$ and $y = vL^{-\omega}$, one can approximate f with its Taylor

expansion near the critical point,

$$R(p, L) = a_R + b_R(p - p_0)L^{1/\nu} + c_R(p - p_0)^2 L^{2/\nu} + d_R/L^{\omega} + ... \tag{C.4}$$

where we assume p is close to the critical point p_0 and the system size is sufficiently large so that both $x = (p - p_0)L^{1/\nu}$ and $y = vL^{-\omega}$ are small. We also redefine the Taylor coefficient d_R to absorb the unknown amplitude v of the irrelevant variable. In the ideal case $d_R = 0$, $R(p_0, L)$ collapses to the universal constant a_R at the critical point. It indicates that the curves $R(p, L)$ for different system sizes perfectly cross at $p = p_0$. However, in realistic models, d_R is non-zero. The irrelevant field then shifts the crossing points as the system size increases.

The ansatz Eq.(C.4) allows us to extract the phase transition point p_0 and the critical exponent ν with the presence of a non-negligible irrelevant scaling variable. In practice, we collect dozens of data points for different p and system size L in the vicinity of the critical points. We then perform a non-linear fitting with the ansatz Eq. (C.4) by taking the coefficients a, b, c, d and critical properties p_0 and ν as the fitting parameters. We then try to drop some of the parameters to make sure the fitting is robust and the error bars are reliable.

BIBLIOGRAPHY

[1] Bistritzer, Rafi, and MacDonald, Allan H. Moiré bands in twisted double-layer graphene. *Proceedings of the National Academy of Sciences of the United States of America 108*, 30 (jul 2011), 12233–12237.

[2] Cao, Yuan, Fatemi, Valla, Fang, Shiang, Watanabe, Kenji, Taniguchi, Takashi, Kaxiras, Efthimios, and Jarillo-Herrero, Pablo. Unconventional superconductivity in magic-angle graphene superlattices. *Nature 556*, 7699 (apr 2018), 43–50.

[3] Cao, Yuan, Fatemi, Valla, Demir, Ahmet, Fang, Shiang, Tomarken, Spencer L., Luo, Jason Y., Sanchez-Yamagishi, Javier D., Watanabe, Kenji, Taniguchi, Takashi, Kaxiras, Efthimios, Ashoori, Ray C., and Jarillo-Herrero, Pablo. Correlated insulator behaviour at half-filling in magic-angle graphene superlattices. *Nature 556*, 7699 (apr 2018), 80–84.

[4] Sbroscia, Matteo, Viebahn, Konrad, Carter, Edward, Yu, Jr-Chiun, Gaunt, Alexander, and Schneider, Ulrich. Observing localisation in a 2D quasicrystalline optical lattice.

[5] Roati, Giacomo, D'Errico, Chiara, Fallani, Leonardo, Fattori, Marco, Fort, Chiara, Zaccanti, Matteo, Modugno, Giovanni, Modugno, Michele, and Inguscio, Massimo. Anderson localization of a non-interacting Bose-Einstein condensate. *Nature 453*, 7197 (jun 2008), 895–898.

[6] Schreiber, Michael, Hodgman, Sean S., Bordia, Pranjal, Lüschen, Henrik P., Fischer, Mark H., Vosk, Ronen, Altman, Ehud, Schneider, Ulrich, and Bloch, Immanuel. Observation of many-body localization of interacting fermions in a quasirandom optical lattice. *Science 349*, 6250 (aug 2015), 842–845.

[7] Bordia, Pranjal, Lüschen, Henrik P., Hodgman, Sean S., Schreiber, Michael, Bloch, Immanuel, and Schneider, Ulrich. Coupling Identical one-dimensional Many-Body Localized Systems. *Physical Review Letters 116*, 14 (2016).

[8] Lüschen, Henrik P., Scherg, Sebastian, Kohlert, Thomas, Schreiber, Michael, Bordia, Pranjal, Li, Xiao, Das Sarma, S., and Bloch, Immanuel. Single-Particle Mobility Edge in a One-Dimensional Quasiperiodic Optical Lattice. *Physical Review Letters 120*, 16 (2018).

[9] Lüschen, Henrik P., Bordia, Pranjal, Scherg, Sebastian, Alet, Fabien, Altman, Ehud, Schneider, Ulrich, and Bloch, Immanuel. Observation of Slow Dynamics near the Many-Body Localization Transition in One-Dimensional Quasiperiodic Systems. *Physical Review Letters 119*, 26 (dec 2017), 260401.

[10] Viebahn, Konrad, Sbroscia, Matteo, Carter, Edward, Yu, Jr Chiun, and Schneider, Ulrich. Matter-Wave Diffraction from a Quasicrystalline Optical Lattice. *Physical Review Letters 122*, 11 (2019).

[11] Deissler, B., Zaccanti, M., Roati, G., D'Errico, C., Fattori, M., Modugno, M., Modugno, G., and Inguscio, M. Delocalization of a disordered bosonic system by repulsive interactions. *Nature Physics 6*, 5 (apr 2010), 354–358.

[12] Sanchez-Palencia, Laurent, and Lewenstein, MacIej. Disordered quantum gases under control. *Nature Physics 6*, 2 (feb 2010), 87–95.

[13] Bordia, Pranjal, Lüschen, Henrik, Scherg, Sebastian, Gopalakrishnan, Sarang, Knap, Michael, Schneider, Ulrich, and Bloch, Immanuel. Probing slow relaxation and many-body localization in two-dimensional quasiperiodic systems. *Physical Review X 7*, 4 (nov 2017), 041047.

[14] Viebahn, Konrad, Sbroscia, Matteo, Carter, Edward, Yu, Jr Chiun, and Schneider, Ulrich. Matter-Wave Diffraction from a Quasicrystalline Optical Lattice. *Physical Review Letters 122*, 11 (mar 2019), 110404.

[15] Corcovilos, Theodore A., and Mittal, Jahnavee. Two-dimensional optical quasicrystal potentials for ultracold atom experiments. *Applied Optics 58*, 9 (mar 2019), 2256.

[16] Kohlert, Thomas, Scherg, Sebastian, Li, Xiao, Lüschen, Henrik P., Das Sarma, Sankar, Bloch, Immanuel, and Aidelsburger, Monika. Observation of Many-Body Localization in a One-Dimensional System with a Single-Particle Mobility Edge. *Physical Review Letters 122*, 17 (may 2019), 170403.

[17] Kraus, Yaacov E., Lahini, Yoav, Ringel, Zohar, Verbin, Mor, and Zilberberg, Oded. Topological states and adiabatic pumping in quasicrystals. *Physical Review Letters 109*, 10 (2012), 106402.

[18] Christodoulides, Demetrios N., Lederer, Falk, and Silberberg, Yaron. Discretizing light behaviour in linear and nonlinear waveguide lattices, 2003.

[19] Szameit, Alexander, Blömer, Dominik, Burghoff, Jonas, Schreiber, Thomas, Pertsch, Thomas, Nolte, Stefan, Tünnermann, Andreas, and Lederer, Falk. Discrete nonlinear localization in femtosecond laser written waveguides in fused silica. *Optics Express 13*, 26 (dec 2005), 10552.

[20] Lahini, Y., Pugatch, R., Pozzi, F., Sorel, M., Morandotti, R., Davidson, N., and Silberberg, Y. Observation of a localization transition in quasiperiodic photonic lattices. *Physical Review Letters 103*, 1 (jun 2009), 013901.

[21] Else, Dominic V, Ho, Wen Wei, and Dumitrescu, Philipp T. Long-Lived Interacting Phases of Matter Protected by Multiple Time-Translation Symmetries in Quasiperiodically Driven Systems. *Physical Review X 10*, 2 (2020).

[22] Dumitrescu, Philipp T., Vasseur, Romain, and Potter, Andrew C. Logarithmically Slow Relaxation in Quasiperiodically Driven Random Spin Chains. *Physical Review Letters 120*, 7 (feb 2018), 070602.

[23] Giergiel, Krzysztof, Kuroś, Arkadiusz, and Sacha, Krzysztof. Discrete time quasicrystals. *Physical Review B 99*, 22 (2019).

[24] Zhao, Hongzheng, Mintert, Florian, and Knolle, Johannes. Floquet time spirals and stable discrete-time quasicrystals in quasiperiodically driven quantum many-body systems. *Physical Review B 100*, 13 (oct 2019), 134302.

[25] Verdeny, Albert, Puig, Joaquim, and Mintert, Florian. Quasi-periodically driven quantum systems. *Zeitschrift fur Naturforschung - Section A Journal of Physical Sciences 71*, 10 (oct 2016), 897–907.

[26] Nandy, Sourav, Sen, Arnab, and Sen, Diptiman. Aperiodically driven integrable systems and their emergent steady states. *Physical Review X 7*, 3 (2017).

[27] Cubero, David, and Renzoni, Ferruccio. Asymptotic theory of quasiperiodically driven quantum systems. *Physical Review E 97*, 6 (jun 2018), 062139.

[28] Nandy, Sourav, Sen, Arnab, and Sen, Diptiman. Steady states of a quasiperiodically driven integrable system. *Physical Review B 98*, 24 (dec 2018), 245144.

[29] Ray, Sayak, Sinha, Subhasis, and Sen, Diptiman. Dynamics of quasiperiodically driven spin systems. *Physical Review E 100*, 5 (nov 2019), 052129.

[30] Crowley, P. J.D., Martin, I., and Chandran, A. Topological classification of quasiperiodically driven quantum systems. *Physical Review B 99*, 6 (feb 2019), 064306.

[31] Martin, Ivar, Refael, Gil, and Halperin, Bertrand. Topological frequency conversion in strongly driven quantum systems. *Physical Review X 7*, 4 (oct 2017), 041008.

[32] Wilkinson, M. Critical properties of electron eigenstates in incommensurate systems. *Proceedings of the Royal Society of London. A. Mathematical and Physical Sciences 391*, 1801 (1984), 305–350.

[33] Kohmoto, Mahito, Kadanoff, Leo P., and Tang, Chao. Localization problem in one dimension: Mapping and escape. Tech. Rep. 23, 1983.

[34] Kohmoto, Mahito, and Banavar, Jayanth R. Quasiperiodic lattice: Electronic properties, phonon properties, and diffusion. Tech. Rep. 2, 1986.

[35] You, J. Q., Yan, J. R., Xie, Tiansheng, Zeng, Xiaobiao, and Zhong, J. X. Generalized Fibonacci lattices: Dynamical maps, energy spectra and wavefunctions. Tech. Rep. 38, 1991.

[36] Suslov, IM. Localization in one-dimensional incommensurate systems. Tech. rep., 1982.

[37] Niu, Qian, and Nori, Franco. Renormalization-Group Study of One-Dimensional Quasiperiodic Systems. *Physical Review Letters 57*, 16 (oct 1986), 2057–2060.

[38] Niu, Qian, and Nori, Franco. Spectral splitting and wave-function scaling in quasicrystalline and hierarchical structures. *Physical Review B 42*, 16 (dec 1990), 10329–10341.

[39] Hatsugai, Y., and Kohmoto, M. Energy spectrum and the quantum Hall effect on the square lattice with next-nearest-neighbor hopping. *Physical Review B 42*, 13 (nov 1990), 8282–8294.

[40] Azbel, M. Ya. Quantum particle in one-dimensional potentials with incommensurate periods. *Physical Review Letters 43*, 26 (dec 1979), 1954–1957.

[41] Avila, Artur, and Jitomirskaya, Svetlana. The ten Martini problem. *Annals of Mathematics 170*, 1 (2009), 303–342.

[42] Kraus, Yaacov E., Ringel, Zohar, and Zilberberg, Oded. Four-dimensional quantum hall effect in a two-dimensional quasicrystal. *Physical Review Letters 111*, 22 (2013).

[43] Senechal, Marjorie. *Quasicrystals and Geometry*. Cambridge University Press, Cambridge, 1995.

[44] Rodriguez, Alejandro W, McCauley, Alexander P., Avniel, Yehuda, and Johnson, Steven G. Computation and visualization of photonic quasicrystal spectra via Bloch's theorem. *Physical Review B - Condensed Matter and Materials Physics 77*, 10 (2008).

[45] Hofstadter, Douglas R. Energy levels and wave functions of Bloch electrons in rational and irrational magnetic fields. *Physical Review B 14*, 6 (sep 1976), 2239–2249.

[46] Azbel, M Ya. Energy spectrum of a conduction electron in a magnetic field. *Soviet Physics JETP 19*, 3 (1964), 634–645.

[47] Takahashi, Minoru. *Thermodynamics of One-Dimensional Solvable Models*. 1999.

[48] Zotos, X. Finite Temperature Drude Weight of the One-Dimensional Spin-\$1/2\$ Heisenberg Model. *Phys. Rev. Lett. 82*, 8 (feb 1999), 1764–1767.

[49] Karrasch, C, Bardarson, J H, and Moore, J E. Finite-Temperature Dynamical Density Matrix Renormalization Group and the Drude Weight of Spin-\$1/2\$ Chains. *Phys. Rev. Lett. 108*, 22 (may 2012), 227206.

[50] Prosen, Tomaž. Quasilocal conservation laws in XXZ spin-1/2 chains: Open, periodic and twisted boundary conditions. *Nuclear Physics B 886* (2014), 1177–1198.

[51] Ilievski, Enej, and De Nardis, Jacopo. Ballistic transport in the one-dimensional Hubbard model: The hydrodynamic approach. *Physical Review B 96*, 8 (aug 2017), 81118.

[52] Prosen, Tomaž, and Ilievski, Enej. Families of quasilocal conservation laws and quantum spin transport. *Physical Review Letters 111*, 5 (aug 2013), 57203.

[53] Ilievski, Enej, and De Nardis, Jacopo. Microscopic Origin of Ideal Conductivity in Integrable Quantum Models. *Physical Review Letters 119*, 2 (jul 2017), 20602.

[54] Urichuk, Andrew, Oez, Yahya, Klümper, Andreas, and Sirker, Jesko. The spin Drude weight of the XXZ chain and generalized hydrodynamics. *SciPost Physics 6*, 1 (2019), 5.

[55] Harris, A. B. Effect of random defects on the critical behaviour of ising models. *Journal of Physics C: Solid State Physics 7*, 9 (1974), 1671–1692.

[56] Chayes, J. T., Chayes, L., Fisher, Daniel S., and Spencer, T. Finite-size scaling and correlation lengths for disordered systems. *Physical Review Letters 57*, 24 (dec 1986), 2999–3002.

[57] Dasgupta, Chandan, and Ma, Shang Keng. Low-temperature properties of the random Heisenberg antiferromagnetic chain. *Physical Review B 22*, 3 (aug 1980), 1305–1319.

[58] Fisher, Daniel S. Random transverse field Ising spin chains. *Physical Review Letters 69*, 3 (1992), 534–537.

[59] Fisher, Daniel S. Critical behavior of random transverse-field Ising spin chains. *Physical Review B 51*, 10 (1995), 6411–6461.

[60] Fisher, Daniel S. Random antiferromagnetic quantum spin chains. *Physical Review B 50*, 6 (1994), 3799–3821.

[61] Luck, J. M. Critical behavior of the aperiodic quantum Ising chain in a transverse magnetic field. *Journal of Statistical Physics 72*, 3-4 (1993), 417–458.

[62] Hermisson, Joachim. Aperiodic and correlated disorder in XY chains: Exact results. *Journal of Physics A: Mathematical and General 33*, 1 (dec 2000), 57–79.

[63] Hermisson, Joachim, Grimm, Uwe, and Baake, Michael. Aperiodic Ising quantum chains. Tech. Rep. 21, 1997.

[64] Hida, Kazuo. New universality class in spin-one-half Fibonacci Heisenberg chains. *Physical Review Letters 93*, 3 (jul 2004), 037205–1.

[65] Hida, Kazuo. Density Matrix Renormalization Group Study of the S = 1/2 Antiferromagnetic Heisenberg Chains with Quasiperiodic Exchange Modulation. *Journal of the Physical Society of Japan 68*, 10 (oct 1999), 3177–3180.

[66] Hida, Kazuo. Renormalization group studies of the Fibonacci quantum spin chains. *Journal of the Physical Society of Japan 74*, SUPPL. (2005), 57–62.

[67] Hida, Kazuo. Quasiperiodic Hubbard chains. *Physical Review Letters 86*, 7 (2001), 1331–1334.

[68] Igloi, F. Quantum Ising model on a quasiperiodic lattice. *Journal of Physics A: Mathematical and General 21*, 18 (1988), L911.

[69] Iglói, F, Karevski, D, and Rieger, H. Random and aperiodic quantum spin chains: A comparative study. Tech. rep., 1998.

[70] Iglói, Ferenc, and Turban, Loïc. Exact renormalization-group study of aperiodic Ising quantum chains and directed walks. *Physical Review B - Condensed Matter and Materials Physics 56*, 17 (1997), 11031–11050.

[71] Juhász, Róbert, and Zimborás, Zoltán. Entanglement entropy in aperiodic singlet phases. *Journal of Statistical Mechanics: Theory and Experiment 2007*, 4 (apr 2007), P04004.

[72] Vieira, André P. Aperiodic quantum XXZ chains: Renormalization-group results. *Physical Review B - Condensed Matter and Materials Physics 71*, 13 (2005).

[73] Vieira, André P. Low-energy properties of aperiodic quantum spin chains. *Physical Review Letters 94*, 7 (2005), 77201.

[74] Chandran, A, and Laumann, C R. Localization and symmetry breaking in the quantum quasiperiodic ising glass. *Physical Review X 7*, 3 (2017).

[75] Crowley, P. J. D., Chandran, A., and Laumann, C. R. Critical behavior of the quasi-periodic quantum Ising chain. *arXiv:1812.01660 [cond-mat]* (dec 2018).

[76] Crowley, P. J.D., Chandran, A., and Laumann, C. R. Quasiperiodic Quantum Ising Transitions in 1D. *Physical Review Letters 120*, 17 (2018).

[77] Andre, Serge, and Aubry, Gilles. Analyticity Breaking and Ander- son Localization in Incommensurate Lattices. *Ann. Isr. Phys. Soc. 3, 133* (1980).

[78] Goremykina, Anna, Vasseur, Romain, and Serbyn, Maksym. Analytically Solvable Renormalization Group for the Many-Body Localization Transition. *Physical Review Letters 122*, 4 (jan 2019), 040601.

[79] Dumitrescu, Philipp T., Goremykina, Anna, Parameswaran, Siddharth A., Serbyn, Maksym, and Vasseur, Romain. Kosterlitz-Thouless scaling at many-body localization phase transitions. Tech. Rep. 9, 2019.

[80] Morningstar, Alan, Huse, David A., and Imbrie, John Z. Many-body localization near the critical point. *arXiv preprint arXiv:2006.04825* (2020).

[81] Morningstar, Alan, and Huse, David A. Renormalization-group study of the many-body localization transition in one dimension. *Physical Review B 99*, 22 (jun 2019), 224205.

[82] Lee, Mac, Look, Thomas R., Lim, S. P., and Sheng, D. N. Many-body localization in spin chain systems with quasiperiodic fields. *Physical Review B 96*, 7 (aug 2017), 075146.

[83] Khemani, Vedika, Sheng, D N, and Huse, David A. Two Universality Classes for the Many-Body Localization Transition. *Physical Review Letters 119*, 7 (2017).

[84] Agrawal, Utkarsh, Gopalakrishnan, Sarang, and Vasseur, Romain. Universality and quantum criticality in quasiperiodic spin chains. *Nature Communications 11*, 1 (2020), 1–7.

[85] De Roeck, Wojciech, and Huveneers, François. Stability and instability towards delocalization in many-body localization systems. *Physical Review B 95*, 15 (2017), 155129.

[86] Luitz, David J, Huveneers, François, and De Roeck, Wojciech. How a Small Quantum Bath Can Thermalize Long Localized Chains. *Physical Review Letters 119*, 15 (2017).

[87] Potirniche, Ionut Dragos, Banerjee, Sumilan, and Altman, Ehud. Exploration of the stability of many-body localization in d>1. *Physical Review B 99*, 20 (2019), 205149.

[88] Bordia, Pranjal, Lüschen, Henrik, Schneider, Ulrich, Knap, Michael, and Bloch, Immanuel. Periodically driving a many-body localized quantum system. *Nature Physics 13*, 5 (may 2017), 460–464.

[89] Choi, Jae Yoon, Hild, Sebastian, Zeiher, Johannes, Schauß, Peter, Rubio-Abadal, Antonio, Yefsah, Tarik, Khemani, Vedika, Huse, David A., Bloch, Immanuel, and Gross, Christian. Exploring the many-body localization transition in two dimensions. *Science 352*, 6293 (jun 2016), 1547–1552.

[90] Kondov, S. S., McGehee, W. R., Xu, W., and Demarco, B. Disorder-induced localization in a strongly correlated atomic Hubbard gas. *Physical Review Letters 114*, 8 (2015).

[91] Lukin, Alexander, Rispoli, Matthew, Schittko, Robert, Tai, M. Eric, Kaufman, Adam M., Choi, Soonwon, Khemani, Vedika, Léonard, Julian, and Greiner, Markus. Probing entanglement in a many-body-localized system. *Science 364*, 6437 (apr 2019), 256–260.

[92] Lüschen, Henrik P., Bordia, Pranjal, Hodgman, Sean S., Schreiber, Michael, Sarkar, Saubhik, Daley, Andrew J., Fischer, Mark H., Altman, Ehud, Bloch, Immanuel, and Schneider, Ulrich. Signatures of many-body localization in a controlled open quantum system. *Physical Review X 7*, 1 (mar 2017), 11034.

[93] Rispoli, Matthew, Lukin, Alexander, Schittko, Robert, Kim, Sooshin, Tai, M. Eric, Léonard, Julian, and Greiner, Markus. Quantum critical behaviour at the many-body localization transition. *Nature 573*, 7774 (sep 2019), 385–389.

[94] Rubio-Abadal, Antonio, Choi, Jae Yoon, Zeiher, Johannes, Hollerith, Simon, Rui, Jun, Bloch, Immanuel, and Gross, Christian. Many-Body Delocalization in the Presence of a Quantum Bath. *Physical Review X 9*, 4 (2019).

[95] Wei, Ken Xuan, Ramanathan, Chandrasekhar, and Cappellaro, Paola. Exploring Localization in Nuclear Spin Chains. *Physical Review Letters 120*, 7 (feb 2018), 070501.

[96] Griffiths, Robert B. Nonanalytic Behavior above the Critical Point in a Random Ising Ferromagnet. *Physical Review Letters 23*, 1 (1969), 17–19.

[97] Vojta, Thomas. Quantum griffiths effects and smeared phase transitions in metals: Theory and experiment. *Journal of Low Temperature Physics 161*, 1-2 (oct 2010), 299–323.

[98] Bertini, Bruno, Collura, Mario, De Nardis, Jacopo, and Fagotti, Maurizio. Transport in out-of-equilibrium XXZ chains: Exact profiles of charges and currents. *Physical Review Letters 117*, 20 (nov 2016).

[99] Castro-Alvaredo, Olalla A., Doyon, Benjamin, and Yoshimura, Takato. Emergent hydrodynamics in integrable quantum systems out of equilibrium. *Physical Review X 6*, 4 (may 2016).

[100] Nandkishore, Rahul, and Huse, David A. Many-body localization and thermalization in quantum statistical mechanics. *Annual Review of Condensed Matter Physics 6*, 1 (2015), 15–38.

[101] Vasseur, Romain, and Moore, Joel E. Nonequilibrium quantum dynamics and transport: From integrability to many-body localization. *Journal of Statistical Mechanics: Theory and Experiment 2016*, 6 (2016), 64010.

[102] Abanin, D.˜A., Altman, E, Bloch, I, and Serbyn, M. Ergodicity, Entanglement and Many-Body Localization. *ArXiv e-prints* (apr 2018).

[103] D'Alessio, Luca, Kafri, Yariv, Polkovnikov, Anatoli, and Rigol, Marcos. From quantum chaos and eigenstate thermalization to statistical mechanics and thermodynamics. *Advances in Physics 65*, 3 (2016), 239–362.

[104] Kinoshita, Toshiya, Wenger, Trevor, and Weiss, David S. A quantum Newton's cradle. *Nature 440*, 7086 (apr 2006), 900–903.

[105] Langen, Tim, Erne, Sebastian, Geiger, Remi, Rauer, Bernhard, Schweigler, Thomas, Kuhnert, Maximilian, Rohringer, Wolfgang, Mazets, Igor E., Gasenzer, Thomas, and Schmiedmayer, Jörg. Experimental observation of a generalized Gibbs ensemble. *Science 348*, 6231 (apr 2015), 207–211.

[106] Tang, Yijun, Kao, Wil, Li, Kuan Yu, Seo, Sangwon, Mallayya, Krishnanand, Rigol, Marcos, Gopalakrishnan, Sarang, and Lev, Benjamin L. Thermalization near Integrability in a Dipolar Quantum Newton's Cradle. *Physical Review X 8*, 2 (may 2018), 21030.

[107] Calabrese, Pasquale, and Cardy, John. Time dependence of correlation functions following a quantum quench. *Physical Review Letters 96*, 13 (2006), 136801.

[108] Prosen, Tomaz. Open XXZ spin chain: Nonequilibrium steady state and a strict bound on ballistic transport. *Physical Review Letters 106*, 21 (may 2011), 217206.

[109] Caux, Jean Sébastien, and Essler, Fabian H.L. Time evolution of local observables after quenching to an integrable model. *Physical Review Letters 110*, 25 (jun 2013), 257203.

[110] Fagotti, Maurizio, and Essler, Fabian H.L. Stationary behaviour of observables after a quantum quench in the spin-1/2 Heisenberg XXZ chain. *Journal of Statistical Mechanics: Theory and Experiment 2013*, 7 (2013), P07012.

[111] Essler, Fabian H.L., and Fagotti, Maurizio. Quench dynamics and relaxation in isolated integrable quantum spin chains. *Journal of Statistical Mechanics: Theory and Experiment 2016*, 6 (jun 2016), 64002.

[112] Wouters, B., De Nardis, J., Brockmann, M., Fioretto, D., Rigol, M., and Caux, J. S. Quenching the anisotropic Heisenberg chain: Exact solution and generalized gibbs ensemble predictions. *Physical Review Letters 113*, 11 (sep 2014), 117202.

[113] Ilievski, Enej, Medenjak, Marko, and Prosen, Tomaž. Quasilocal Conserved Operators in the Isotropic Heisenberg Spin- 1/2 Chain. *Physical Review Letters 115*, 12 (sep 2015), 120601.

[114] Ilievski, E., De Nardis, J., Wouters, B., Caux, J. S., Essler, F. H.L., and Prosen, T. Complete Generalized Gibbs Ensembles in an Interacting Theory. *Physical Review Letters 115*, 15 (oct 2015), 157201.

[115] Ilievski, Enej, Medenjak, Marko, Prosen, Tomaž, and Zadnik, Lenart. Quasilocal charges in integrable lattice systems. *Journal of Statistical Mechanics: Theory and Experiment 6*, 6 (2016), 1–51.

[116] Fagotti, Maurizio, Collura, Mario, Essler, Fabian H.L., and Calabrese, Pasquale. Relaxation after quantum quenches in the spin- 1 2 Heisenberg XXZ chain. *Physical Review B - Condensed Matter and Materials Physics 89*, 12 (mar 2014), 125101.

[117] Rigol, Marcos, Dunjko, Vanja, Yurovsky, Vladimir, and Olshanii, Maxim. Relaxation in a completely integrable many-body Quantum system: An Ab initio study of the dynamics of the highly excited states of 1D lattice hard-core bosons. *Physical Review Letters 98*, 5 (feb 2007), 050405.

[118] Caux, Jean Sébastien, and Konik, Robert M. Constructing the generalized Gibbs ensemble after a quantum quench. *Physical Review Letters 109*, 17 (oct 2012), 175301.

[119] Rigol, Marcos. Breakdown of Thermalization in Finite One-Dimensional Systems. *Physical Review Letters 103*, 10 (sep 2009), 100403.

[120] Bernard, Denis, and Doyon, Benjamin. Conformal field theory out of equilibrium: A review. *Journal of Statistical Mechanics: Theory and Experiment 2016*, 6 (jun 2016), 64005.

[121] Spohn, Herbert. Interacting and noninteracting integrable systems. *Journal of Mathematical Physics 59*, 9 (jun 2018), 091402.

[122] Han, J. H., Thouless, D. J., Hiramoto, H., and Kohmoto, M. Critical and bicritical properties of Harper's equation with next-nearest-neighbor coupling. Tech. Rep. 16, 1994.

[123] Thouless, D. J. Bandwidths for a quasiperiodic tight-binding model. Tech. Rep. 8, 1983.

[124] El, G. A. The thermodynamic limit of the Whitham equations. *Physics Letters, Section A: General, Atomic and Solid State Physics 311*, 4-5 (2003), 374–383.

[125] El, G. A., and Kamchatnov, A. M. Kinetic equation for a dense soliton gas. *Physical Review Letters 95*, 20 (nov 2005), 204101.

[126] Bulchandani, Vir B., Vasseur, Romain, Karrasch, Christoph, and Moore, Joel E. Bethe-Boltzmann hydrodynamics and spin transport in the XXZ chain. *Physical Review B 97*, 4 (jan 2018), 45407.

[127] Doyon, Benjamin, Yoshimura, Takato, and Caux, Jean Sébastien. Soliton Gases and Generalized Hydrodynamics. *Physical Review Letters 120*, 4 (jan 2018), 45301.

[128] Spohn, Herbert. *Large Scale Dynamics of Interacting Particles*. Theoretical and Mathematical Physics. Springer Berlin Heidelberg, 1991.

[129] De Nardis, Jacopo, Bernard, Denis, and Doyon, Benjamin. Hydrodynamic Diffusion in Integrable Systems. *Physical Review Letters 121*, 16 (oct 2018).

[130] Gopalakrishnan, Sarang, Huse, David A., Khemani, Vedika, and Vasseur, Romain. Hydrodynamics of operator spreading and quasiparticle diffusion in interacting integrable systems. *Physical Review B 98*, 22 (dec 2018).

[131] De Nardis, Jacopo, Bernard, Denis, and Doyon, Benjamin. Diffusion in generalized hydrodynamics and quasiparticle scattering. *SciPost Physics 6*, 4 (dec 2019).

[132] Gopalakrishnan, Sarang, and Vasseur, Romain. Kinetic Theory of Spin Diffusion and Superdiffusion in XXZ Spin Chains. *Physical Review Letters 122*, 12 (mar 2019), 127202.

[133] Fagotti, Maurizio. Higher-order generalized hydrodynamics in one dimension: The noninteracting test. *Physical Review B 96*, 22 (dec 2017), 220302.

[134] Essler, Fabian H.L., Van Den Berg, Rianne, and Gritsev, Vladimir. Integrable spin chains with random interactions. *Physical Review B 98*, 2 (jul 2018).

[135] Vosk, Ronen, and Altman, Ehud. Many-body localization in one dimension as a dynamical renormalization group fixed point. *Physical Review Letters 110*, 6 (feb 2013), 067204.

[136] Vasseur, Romain, Friedman, Aaron J., Parameswaran, S. A., and Potter, Andrew C. Particle-hole symmetry, many-body localization, and topological edge modes. *Physical Review B 93*, 13 (apr 2016), 134207.

[137] De Vega, H. J., and Woynarovich, F. New integrable quantum chains combining different kinds of spins. *Journal of Physics A: Mathematical and General 25*, 17 (1992), 4499–4516.

[138] De Vega, H. J., Mezincescu, Luca, and Nepomechie, Rafael I. Thermodynamics of integrable chains with alternating spins. *Physical Review B 49*, 18 (may 1994), 13223–13226.

[139] Takahashi, Minoru. *Thermodynamics of One-Dimensional Solvable Models*. Cambridge, UK: Cambridge University Press, 1999.

[140] Boon, J. P., Grosfils, P., and Lutsko, J. F. Temporal diffusion. *Europhysics Letters 63*, 2 (jul 2003), 186–192.

[141] Langmann, Edwin, and Moosavi, Per. Diffusive Heat Waves in Random Conformal Field Theory. *Physical Review Letters 122*, 2 (jul 2019).

[142] Naef, F, and Zotos, X. Spin and energy correlations in the one dimensional spin-Heisenberg model. *Journal of Physics: Condensed Matter 10*, 12 (1998), L183.

[143] Rigol, Marcos, and Shastry, B Sriram. Drude weight in systems with open boundary conditions. *Phys. Rev. B 77*, 16 (apr 2008), 161101.

[144] Karrasch, C, Kennes, D M, and Heidrich-Meisner, F. Spin and thermal conductivity of quantum spin chains and ladders. *Phys. Rev. B 91*, 11 (mar 2015), 115130.

[145] Herbrych, J, Steinigeweg, R, and Prelov\ifmmode \checks\else š\fiek, P. Spin hydrodynamics in the $ S=1/2 anisotropic Heisenberg chain. *Phys. Rev. B 86*, 11 (sep 2012), 115106.

[146] Sánchez, Ramsés J, Varma, Vipin Kerala, and Oganesyan, Vadim. Anomalous and regular transport in spin-1 2 chains: ac conductivity. *Physical Review B 98*, 5 (2018), 54415.

[147] Collura, Mario, De Luca, Andrea, and Viti, Jacopo. Analytic solution of the domain-wall nonequilibrium stationary state. *Physical Review B 97*, 8 (feb 2018), 81111.

[148] Lieb, Elliott H, and Robinson, Derek W. *The Finite Group Velocity of Quantum Spin Systems*. Springer Berlin Heidelberg, Berlin, Heidelberg, 2004, pp. 425–431.

[149] Ilievski, Enej, De Nardis, Jacopo, Medenjak, Marko, and Prosen, Tomaz. Superdiffusion in One-Dimensional Quantum Lattice Models. *Phys. Rev. Lett. 121*, 23 (dec 2018), 230602.

[150] De Nardis, Jacopo, Bernard, Denis, and Doyon, Benjamin. Hydrodynamic Diffusion in Integrable Systems. *Phys. Rev. Lett. 121*, 16 (oct 2018), 160603.

[151] Nardis, Jacopo De, Bernard, Denis, and Doyon, Benjamin. Diffusion in generalized hydrodynamics and quasiparticle scattering. *SciPost Phys. 6*, 4 (2019), 49.

[152] Gopalakrishnan, Sarang, Huse, David A, Khemani, Vedika, and Vasseur, Romain. Hydrodynamics of operator spreading and quasiparticle diffusion in interacting integrable systems. *Phys. Rev. B 98*, 22 (dec 2018), 220303.

[153] Agrawal, Utkarsh, Gopalakrishnan, Sarang, Vasseur, Romain, and Ware, Brayden. Anomalous low-frequency conductivity in easy-plane XXZ spin chains. *Physical Review B 101*, 22 (2020), 224415.

[154] Van Damme, Maarten, Vanderstraeten, Laurens, De Nardis, Jacopo, Haegeman, Jutho, and Verstraete, Frank. Real-time scattering of interacting quasiparticles in quantum spin chains. *arXiv:1907.02474 [cond-mat]* (jul 2019).

[155] Bouchaud, Jean Philippe, and Georges, Antoine. Anomalous diffusion in disordered media: Statistical mechanisms, models and physical applications. *Physics Reports 195*, 4-5 (1990), 127–293.

[156] Agrawal, Utkarsh, Gopalakrishnan, Sarang, and Vasseur, Romain. Quantum criticality in the 2d quasiperiodic Potts model.

[157] Motrunich, Olexei, Mau, Siun-Chuon Chuon, Huse, David A., and Fisher, Daniel S. Infinite-randomness quantum Ising critical fixed points. *Physical Review B - Condensed Matter and Materials Physics 61*, 2 (jan 2000), 1160–1172.

[158] Vojta, Thomas. Disorder in quantum many-body systems, jun 2019.

[159] Jagannathan, A. Quantum Spins and Quasiperiodicity: A Real Space Renormalization Group Approach. *Physical Review Letters 92*, 4 (jan 2004), 4.

[160] Giamarchi, T., and Schulz, H. J. Anderson localization and interactions in one-dimensional metals. *Physical Review B 37*, 1 (jan 1988), 325–340.

[161] Vidal, Julien, Mouhanna, Dominique, and Giamarchi, Thierry. Interacting fermions in self-similar potentials. *Physical Review B - Condensed Matter and Materials Physics 65*, 1 (nov 2002), 142011–1420115.

[162] Vidal, Julien, Mouhanna, Dominique, and Giamarchi, Thierry. Correlated fermions in a one-dimensional quasiperiodic potential. *Physical Review Letters 83*, 19 (1999), 3908–3911.

[163] Luck, J. M. A classification of critical phenomena on quasi-crystals and other aperiodic structures. *Epl 24*, 5 (1993), 359–364.

[164] Szabó, Attila, and Schneider, Ulrich. Non-power-law universality in one-dimensional quasicrystals. *Physical Review B 98*, 13 (2018), 134201.

[165] Senthil, T., and Majumdar, Satya N. Critical properties of random quantum potts and clock models. *Physical Review Letters 76*, 16 (apr 1996), 3001–3004.

[166] Fendley, Paul. Parafermionic edge zero modes in Zn-invariant spin chains. *Journal of Statistical Mechanics: Theory and Experiment 2012*, 11 (2012).

[167] Inoue, Takashi, and Yamamoto, Shoji. Optical Observation of Quasiperiodic Heisenberg Antiferromagnets in Two Dimensions. *Physica Status Solidi (B) Basic Research* (apr 2020).

[168] Szabó, Attila, and Schneider, Ulrich. Mixed spectra and partially extended states in a two-dimensional quasiperiodic model. *Physical Review B 101*, 1 (jan 2020), 014205.

[169] Pich, C., Young, A. P., Rieger, H., and Kawashima, N. Critical behavior and griffiths-mccoy singularities in the two-dimensional random quantum ising ferromagnet. *Physical Review Letters 81*, 26 (dec 1998), 5916–5919.

[170] Guo, Muyu, Bhatt, R. N., and Huse, David A. Quantum critical behavior of a three-dimensional Ising spin glass in a transverse magnetic field. *Physical Review Letters 72*, 26 (jun 1994), 4137–4140.

[171] Rieger, H., and Young, A. P. Zero-temperature quantum phase transition of a two-dimensional Ising spin glass. *Physical Review Letters 72*, 26 (jun 1994), 4141–4144.

[172] Kang, Byungmin, Parameswaran, S. A., Potter, Andrew C., Vasseur, Romain, and Gazit, Snir. Superuniversality from disorder at two-dimensional topological phase transitions. *arXiv e-prints* (aug 2020), arXiv:2008.09617.

[173] Orús, Román. A practical introduction to tensor networks: Matrix product states and projected entangled pair states. *Annals of Physics 349* (oct 2014), 117–158.

[174] Kovács, István A., and Iglói, Ferenc. Renormalization group study of the two-dimensional random transverse-field Ising model. *Physical Review B - Condensed Matter and Materials Physics 82*, 5 (may 2010).

[175] Lin, Yu-Cheng, Iglói, Ferenc, and Rieger, Heiko. Entanglement {Entropy} at {Infinite}-{Randomness} {Fixed} {Points} in {Higher} {Dimensions}. *Physical Review Letters 99*, 14 (oct 2007), 147202.

[176] Bazavov, Alexei, Berg, Bernd A., and Dubey, Santosh. Phase transition properties of 3D Potts models. Tech. Rep. 3, 2008.

[177] Hellmund, Meik, and Janke, Wolfhard. High-temperature series expansions for the q-state Potts model on a hypercubic lattice and critical properties of percolation. *Physical Review E - Statistical, Nonlinear, and Soft Matter Physics 74*, 5 (2006).

[178] Wu, F. Y. The Potts model. *Reviews of Modern Physics 54*, 1 (jan 1982), 235–268.

[179] Hui, Kenneth, and Berker, A. Nihat. Random-field mechanism in random-bond multicritical systems. *Physical Review Letters 62*, 21 (may 1989), 2507–2510.

[180] Kovács, István A., and Iglói, Ferenc. Critical behavior and entanglement of the random transverse-field Ising model between one and two dimensions. *Physical Review B - Condensed Matter and Materials Physics 80*, 21 (dec 2009), 214416.

[181] Yu, Rong, Saleur, Hubert, and Haas, Stephan. Entanglement entropy in the two-dimensional random transverse field Ising model. *Physical Review B - Condensed Matter and Materials Physics 77*, 14 (apr 2008), 140402.

[182] Deng, Youjin, and Blöte, Henk W J. Simultaneous analysis of several models in the three-dimensional Ising universality class. *Phys. Rev. E 68*, 3 (sep 2003), 36125.

[183] Skinner, Brian, Ruhman, Jonathan, and Nahum, Adam. Measurement-Induced Phase Transitions in the Dynamics of Entanglement. *Physical Review X 9*, 3 (2019).

[184] Chan, Amos, Nandkishore, Rahul M., Pretko, Michael, and Smith, Graeme. Unitary-projective entanglement dynamics. *Physical Review B 99*, 22 (jun 2019), 224307.

[185] Gullans, Michael J., and Huse, David A. Dynamical Purification Phase Transition Induced by Quantum Measurements. *Physical Review X 10*, 4 (oct 2020), 41020.

[186] Choi, Soonwon, Bao, Yimu, Qi, Xiao Liang, and Altman, Ehud. Quantum Error Correction in Scrambling Dynamics and Measurement-Induced Phase Transition. *Physical Review Letters 125*, 3 (mar 2020).

[187] Fan, Ruihua, Vijay, Sagar, Vishwanath, Ashvin, and You, Yi Zhuang. Self-organized error correction in random unitary circuits with measurement. *Physical Review B 103*, 17 (feb 2021).

[188] Rakovszky, Tibor, Pollmann, Frank, and Von Keyserlingk, C. W. Diffusive Hydrodynamics of Out-of-Time-Ordered Correlators with Charge Conservation. *Physical Review X 8*, 3 (oct 2018).

[189] Khemani, Vedika, Huse, David A., and Nahum, Adam. Velocity-dependent Lyapunov exponents in many-body quantum, semiclassical, and classical chaos. *Physical Review B 98*, 14 (oct 2018), 144304.

[190] Huang, Yichen. Dynamics of Renyi entanglement entropy in local quantum circuits with charge conservation. *arXiv:1902.00977 [cond-mat, physics:hep-th, physics:quant-ph]* (feb 2019).

[191] Rakovszky, Tibor, Pollmann, Frank, and Von Keyserlingk, C. W. Sub-ballistic Growth of Rényi Entropies due to Diffusion. *Physical Review Letters 122*, 25 (jun 2019), 250602.

[192] Zhou, Tianci, and Ludwig, Andreas W.W. Diffusive scaling of Rényi entanglement entropy. *Physical Review Research 2*, 3 (jul 2020), 33020.

[193] Žnidarič, Marko. Entanglement growth in diffusive systems. *Communications Physics 3*, 1 (jan 2020), 1–9.

[194] Bao, Yimu, Choi, Soonwon, and Altman, Ehud. Symmetry enriched phases of quantum circuits. *Annals of Physics 435* (feb 2021), arXiv:2102.09164.

[195] Aaronson, Scott, and Gottesman, Daniel. Improved simulation of stabilizer circuits. *Physical Review A - Atomic, Molecular, and Optical Physics 70*, 5 A (nov 2004), 052328.

[196] Gottesman, Daniel. The Heisenberg Representation of Quantum Computers.

[197] Ippoliti, Matteo, and Khemani, Vedika. Postselection-Free Entanglement Dynamics via Spacetime Duality. *Physical Review Letters 126*, 6 (feb 2021), 060501.

[198] Piroli, Lorenzo, Bertini, Bruno, Cirac, J. Ignacio, and Prosen, TomaŽ. Exact dynamics in dual-unitary quantum circuits. *Physical Review B 101*, 9 (2020).

[199] Bertini, Bruno, Kos, Pavel, and Prosen, TomaŽ. Exact Correlation Functions for Dual-Unitary Lattice Models in <math xmlns. *Physical Review Letters 123*, 21 (nov 2019), 210601.

[200] Bertini, Bruno, Kos, Pavel, and Prosen, Tomaž. Entanglement Spreading in a Minimal Model of Maximal Many-Body Quantum Chaos. *Physical Review X 9*, 2 (2019).

[201] Bertini, Bruno, Kos, Pavel, and Prosen, Tomaž. Exact Spectral Form Factor in a Minimal Model of Many-Body Quantum Chaos. *Physical Review Letters 121*, 26 (dec 2018), 264101.

[202] Bremner, Michael J., Jozsa, Richard, and Shepherd, Dan J. Classical simulation of commuting quantum computations implies collapse of the polynomial hierarchy. *Proceedings of the Royal Society A: Mathematical, Physical and Engineering Sciences 467*, 2126 (feb 2011), 459–472.

[203] Shepherd, Dan, and Bremner, Michael J. Temporally unstructured quantum computation. *Proceedings of the Royal Society A: Mathematical, Physical and Engineering Sciences 465*, 2105 (may 2009), 1413–1439.

[204] Collins, Benoît. Moments and cumulants of polynomial random variables on unitary groups, the itzykson-zuber integral, and free probability. *International Mathematics Research Notices 2003*, 17 (jan 2003), 953–982.

[205] Zhou, Tianci, and Nahum, Adam. Emergent statistical mechanics of entanglement in random unitary circuits. *Physical Review B 99*, 17 (apr 2019).

[206] Bao, Yimu, Choi, Soonwon, and Altman, Ehud. Theory of the phase transition in random unitary circuits with measurements. *Physical Review B 101*, 10 (aug 2020).

[207] Vasseur, Romain, Potter, Andrew C, You, Yi-Zhuang, and Ludwig, Andreas W W. Entanglement transitions from holographic random tensor networks. *Phys. Rev. B 100*, 13 (oct 2019), 134203.

[208] Li, Yaodong, Chen, Xiao, and Fisher, Matthew P.A. Quantum Zeno effect and the many-body entanglement transition. *Physical Review B 98*, 20 (nov 2018), 205136.

[209] Page, Don N. Average entropy of a subsystem. *Physical Review Letters 71*, 9 (1993), 1291–1294.

[210] Agrawal, Utkarsh, Zabalo, Aidan, Chen, Kun, Wilson, Justin H, Potter, Andrew C, Pixley, J.˜H., Gopalakrishnan, Sarang, and Vasseur, Romain. Entanglement and charge-sharpening transitions in U(1) symmetric monitored quantum circuits. *arXiv e-prints* (jul 2021), arXiv:2107.10279.

[211] Blais, Alexandre, Grimsmo, Arne L, Girvin, S M, and Wallraff, Andreas. Circuit quantum electrodynamics. *Rev. Mod. Phys. 93*, 2 (may 2021), 25005.

[212] Zabalo, Aidan, Gullans, Michael J, Wilson, Justin H, Gopalakrishnan, Sarang, Huse, David A, and Pixley, J H. Critical properties of the measurement-induced transition in random quantum circuits. *Physical Review B 101*, 6 (oct 2020).

[213] Gullans, Michael J, and Huse, David A. Scalable Probes of Measurement-Induced Criticality. *Physical Review Letters 125*, 7 (sep 2020).

[214] Huang, Yichen. Dynamics of Rényi entanglement entropy in diffusive qudit systems. *IOP SciNotes 1*, 3 (feb 2020), 035205.

[215] Calabrese, Pasquale, and Cardy, John. Entanglement entropy and conformal field theory. *Journal of Physics A: Mathematical and Theoretical 42*, 50 (dec 2009), 504005.

[216] Jian, Chao Ming, You, Yi Zhuang, Vasseur, Romain, and Ludwig, Andreas W W. Measurement-induced criticality in random quantum circuits. *Physical Review B 101*, 10 (aug 2020).

[217] Hayden, Patrick, Nezami, Sepehr, Qi, Xiao-Liang, Thomas, Nathaniel, Walter, Michael, and Yang, Zhao. Holographic duality from random tensor networks. *Journal of High Energy Physics 2016*, 11 (2016), 9.

[218] Zabalo, Aidan, Gullans, Michael J, Wilson, Justin H, Vasseur, Romain, Ludwig, Andreas W.˜W., Gopalakrishnan, Sarang, Huse, David A, and Pixley, J.˜H. Operator scaling dimensions and multifractality at measurement-induced transitions. *arXiv e-prints* (jul 2021), arXiv:2107.03393.

[219] Li, Yaodong, and Fisher, Matthew P A. Statistical Mechanics of Quantum Error-Correcting Codes.

[220] Schollwöck, Ulrich. The density-matrix renormalization group in the age of matrix product states. *Annals of Physics 326*, 1 (jan 2011), 96–192.

[221] Li, Yaodong, Chen, Xiao, and Fisher, Matthew P.A. Measurement-driven entanglement transition in hybrid quantum circuits. *Physical Review B 100*, 13 (2019), 134306.

[222] Barratt, Fergus, Agrawal, Utkarsh, Gopalakrishnan, Sarang, Huse, David A, Vasseur, Romain, and Potter, Andrew C. Field theory of charge sharpening in symmetric monitored quantum circuits. *arXiv e-prints* (nov 2021), arXiv:2111.09336.

[223] Vidal, Guifré. Efficient Classical Simulation of Slightly Entangled Quantum Computations. *Phys. Rev. Lett. 91*, 14 (oct 2003), 147902.

[224] Vidal, Guifré. Efficient Simulation of One-Dimensional Quantum Many-Body Systems. *Phys. Rev. Lett. 93*, 4 (jul 2004), 40502.

[225] Fisher, Matthew P A. Duality in low dimensional quantum field theories. In *Strong interactions in low dimensions*. 2007, pp. 419–438.

[226] Nahum, Adam, and Skinner, Brian. Entanglement and dynamics of diffusion-annihilation processes with Majorana defects. *Phys. Rev. Research 2*, 2 (jun 2020), 23288.

[227] Lavasani, Ali, Alavirad, Yahya, and Barkeshli, Maissam. Measurement-induced topological entanglement transitions in symmetric random quantum circuits.

[228] Ippoliti, Matteo, Gullans, Michael J., Gopalakrishnan, Sarang, Huse, David A., and Khemani, Vedika. Entanglement phase transitions in measurement-only dynamics.

[229] Sang, Shengqi, and Hsieh, Timothy H. Measurement Protected Quantum Phases. *arXiv:2004.09509 [cond-mat, physics:quant-ph]* (apr 2020).

[230] Potter, Andrew C, and Vasseur, Romain. Symmetry constraints on many-body localization. *Phys. Rev. B 94*, 22 (dec 2016), 224206.